# EXPERIMENTAL INVESTIGATION OF CORROSION AND WEAR BEHAVIORS OF SHAPE MEMORY MATERIALS

**2024**
**PhD THESIS**
**MECHANICAL ENGINEERING**

**Abuojaila Abdallah Mouammer SOLTAN**

**Thesis Advisor**
**Prof. Dr. İsmail ESEN**

# EXPERIMENTAL INVESTIGATION OF CORROSION AND WEAR BEHAVIORS OF SHAPE MEMORY MATERIALS

**Abuojaila Abdallah Mouammer SOLTAN**

**Thesis Advisor**
**Prof. Dr. İsmail ESEN**

**T.C.**
**Karabuk University**
**Institute of Graduate Programs**
**Department of Mechanical Engineering**
**Prepared as**
**PhD Thesis**

**KARABUK**
**May 2024**

I certify that in my opinion the thesis submitted by Abuojaila Abdallah Mouammer SOLTAN titled “EXPERIMENTAL INVESTIGATION OF CORROSION AND WEAR BEHAVIORS OF SHAPE MEMORY MATERIALS” is fully adequate in scope and in quality as a thesis for the degree of PhD.

Prof. Dr. İsmail ESEN .....

Thesis Advisor, Department of Mechanical Engineering

This thesis is accepted by the examining committee with a unanimous vote in the Department of Mechanical Engineering as a PhD thesis. 05.01.2024

| Examining Committee Members (Institutions) | | Signature |
|---|---|---|
| Chairman | : Prof. Dr. İsmail ESEN (KBU) | ..... |
| Member | : Prof. Dr. Selami SAĞIROĞLU (KBU) | ..... |
| Member | : Assoc. Prof. Dr. İbrahim ÇAYIROĞLU (KBU) | ..... |
| Member | : Assoc. Prof. Dr. Mehmet Akif KOÇ (SUBU) | ..... |
| Member | : Assoc. Prof. Dr. Recep KILIÇ (SUBU) | ..... |

The degree of PhD by the thesis submitted is approved by the Administrative Board of the Institute of Graduate Programs, Karabuk University.

Assoc. Prof. Dr. Zeynep ÖZCAN .....

Director of the Institute of Graduate Programs

*"Bu tezdeki tüm bilgilerin akademik kurallara ve etik ilkelere uygun olarak elde edildiğini ve sunulduğunu; ayrıca bu kuralların ve ilkelerin gerektirdiği şekilde, bu çalışmadan kaynaklanmayan bütün atıfları yaptığımı beyan ederim."*

Abuojaila Abdallah Mouammer SOLTAN

# ÖZET

**Doktora Tezi**

## ŞEKİL HAFIZALI MALZEMELERİN KOROZYON VE AŞINMA DAVRANIŞLARININ DENEYSEL İNCELENMESİ

**Abuojaila Abdallah Mouammer SOLTAN**

**Karabük Üniversitesi**
**Lisansüstü Eğitim Enstitüsü**
**Makine Mühendisliği Anabilim Dalı**

**Tez Danışmanı:**
**Prof. Dr. İsmail ESEN**
**Mayıs 2024, 72 sayfa**

Bu çalışmada, "SMA" alaşımı (Shape Memory-Alloy) olarak adlandırılan ve 25 ile 35°C arasında değişen hafıza sıcaklıkları arasında şekil geri kazanım hafıza etkisi sunan Ni-Ti alaşımı (Ni 55% – Ti 45%) numunelerinin korozyon testleri gerçekleştirildi. Korozyon testleri için 0,3 mm kalınlığında NiTi sac numuneler hazırlanarak potansiyodinamik ve daldırma korozyon testleri yapıldı. NiTi alaşım levha numunelerine standart metalografik prosedürler uygulandı. Ardından metalografik olarak hazırlanan numunelerin Mikroyapı görüntüleri Nikon marka optik mikroskop cihazı kullanılarak görüntüleri elde edilmiştir. Korozyon testi için standart hava ile teması kesilen behere file ile daldırılır. Takiben 0.00001g hassasiyette terazide düzenli aralıklarla ağırlık kaybı ölçülmüştür. İncelenen NiTi süper alaşımın aşınma testleri, kuru ortamda ve vücut sıvısında 20N ve 40N yükler altında karşılıklı aşınma testleri yapılarak gerçekleştirilmiştir.

Aşınma esnasında 100CR6 kalite çelik bilye karşı malzeme ile 13mm uzunluğunda ve 0.04m/s kayma hızında toplam 300 metre numune yüzeyine alınmıştır. Aşınma sonuçları ağırlık kaybı ölçümü ile değerlendirilmiş ve ağırlık kaybı deney öncesi ve sonrasında 0,1 MG hassasiyetli elektronik hassas terazide ölçülmüştür. Yapay vücut sıvısı (SBF) içinde ve oda sıcaklığında potansiyodinamik test yapıldıktan sonra elektrokimyasal analizlerin sonucunda elde edilen Tafel eğrileri kullanılarak numunelerin korozyon direnci hesaplanmıştır. 23 günlük potansiyodinamik test sonuçlarına göre vücut sıvısındaki madde kaybının 0.0046 mm/Yıl olduğu belirlendi ve 10 gün süreyle Havadan izole edilmiş vücut sıvısında yapılan daldırma testinde ağırlık kaybı 0.028 mm/Yıl olarak ölçülmüştür. Ayrıca yüksek korozyon direnci sunan şekil hafızalı malzeme korozif ortamda daha az ağırlık kaybı sergilemiştir.

**Anahtar Sözcükler :** Şekil Hafızalı Alaşım, Nitinol, Korozyon, Aşınma, Mikroyapı.
**Bilim Kodu** **:** 91407, 91501

## ABSTRACT

**Ph. D. Thesis**

**EXPERIMENTAL INVESTIGATION OF CORROSION AND ABRASION BEHAVIOR OF SHAPE MEMORY MATERIALS**

**Abuojaila Abdallah Mouammer SOLTAN**

**Karabuk University**
**Institute of Graduate Programs**
**Department of Mechanical Engineering**

**Thesis Advisor:**
**Prof. Dr. İsmail ESEN**
**June 2024, 72 pages**

In this study, corrosion tests of samples of Ni-Ti alloy (Ni 55% – Ti 45%) called "SMA" alloy (Shape Memory-Alloy) and offering shape recovery memory effect between memory temperatures varying between 25 and 35°C are performed. For corrosion tests, 0.3 mm thick NiTi sheet samples are prepared and potentiodynamic and immersion corrosion tests are performed. Standard metallographic procedures were applied to the NiTi alloy sheet samples.

Then, the microstructure images of the metallographically prepared samples are obtained using Nikon brand optical microscope device. For the corrosion test, the standard net is immersed in the beaker whose contact with air is cut off, and then weight loss is measured at regular intervals on a balance with 0.00001 precision. The wear tests of the examined NiTi super alloy have been carried out by reciprocating wear tests under 20N and 40N loads in a dry environment and in body fluid.

During wear, 100CR6 quality steel ball has been taken with counter material on the sample surface of a 13mm in length and 0.04m/s in the sliding speed, in total 300 meters. The wear results have been evaluated by weight loss measurement, and the weight loss has been measured on an electronic precision balance with 0.1 MG sensitivity before and after the experiment. Corrosion resistance of the samples was calculated by using Tafel curves obtained as a result of electrochemical analysis after potentiodynamic testing in artificial body fluid (SBF) and at room temperature. According to the 23-day potentiodynamic test results, the loss of substance in the body fluid was determined as 0.0046 mm/Year and the weight loss was measured as 0.028 mm/Year in the immersion test performed in the body fluid isolated from the air for 10 days. In addition, the shape memory material, which offers high corrosion resistance, exhibited less weight loss in the corrosive environment.

**Key Word** **:** SMA, Nitinol, Corrosion, Wear, Microstructure.
**Science Code** **:** 91407, 91501

## ACKNOWLEDGEMENT

I would like to express my endless thanks to my advisor "Prof. Dr. İsmail ESEN" for both his unwavering interest and support in the planning, research, execution, and formation of this thesis.

I would like to express my endless thanks to my advisor, whose vast knowledge and experience I have benefited from and who has shaped my work in the light of scientific foundations with his guidance and information.

I would like to thank my family and friends, who have brought me to this day, who have given me strength and believed in me at every stage of my life, and who have supported me throughout the whole process.

**CONTENTS**

**Sayfa**

**Sayfa**

## LIST OF FIGURES

**Page**

**Page**

## LIST OF TABLES

**Page**

## SYMBOLS AND ABBREVITIONS INDEX

### SYMBOLS

$Cr_{eş}$ : Chromium equivalence

$Ni_{eş}$ : Nickel equivalence

Ag : silver

Al : Aluminium

Ar : Argon

Au : Gold

Cu : Cupper

$H_2$ : Hydrogen

He : Helium

Mo : Molybdenum

Ni : Nickel

Ti : Titanium

$\gamma$ : Unit mass

$\sigma$ : Normal stress

### ABBREVIATIONS

AISI : American Iron and Steel Institute (Amerika Demir ve Çelik Enstitüsü)

ASTM : American Society for Testing and Materials (Amerika Deneme ve Malzeme Topluluğu)

AWS : American Welding Society (Amerika Kaynak Topluluğu)

DIN : Deutch Industrie Normen (Alman Endüstri Normları)

EN : European Norm (Avrupa Normu)

IIW : International Institute of Welding (Uluslararası Kaynak Enstitüsü)

SMA : SMA

# PART 1

## INTRODUCTION

Nitinol, also known as nickel-titanium (NiTi) alloy, is a shape-memory alloy (SMA) that has gained significant attention in various fields due to its unique properties and potential applications [1], [2], [11], [12], [3]–[10]. The term "nitinol" was coined in the 1960s to denote the composition (nickel-titanium) and place of discovery (Naval Ordnance Laboratory) of this alloy [1]. NiTi alloy is commercially available and is one of the most popular and well-studied SMAs [1]. It outperforms other SMA metals, such as iron or copper-based alloys, in terms of mechanical and thermomechanical properties [1].

The shape-memory effect in NiTi alloy was first discovered in the 1960s [1]. This effect allows the alloy to "remember" its original shape and recover it upon heating after substantial mechanical deformation [13]. NiTi alloy exhibits an austenite phase, which is the high-temperature stable phase, and a martensite phase, which is the low-temperature stable phase [14]. The usually assumed austenitic structure is cubic B2, but the exact atomic structure of the austenite phase in NiTi alloy is still a subject of research [13], [15]. The alloy undergoes a reversible martensitic phase transformation between these two phases, which is responsible for its shape-memory effect and superelasticity [14] [15].

NiTi alloy has excellent mechanical properties, including superelasticity and high damping capacity [11] [7]. Superelasticity refers to the ability of the alloy to undergo large elastic deformations and recover its original shape upon unloading, even after being deformed beyond its elastic limit [7]. This property makes NiTi alloy suitable for applications where high flexibility and resistance to deformation are required, such as orthodontic wires, braces, and stents [2], [16]. The high damping capacity of NiTi alloy allows it to absorb and dissipate mechanical energy, making it useful in

applications that require vibration damping, such as in aerospace and automotive industries [7].

In addition to its mechanical properties, NiTi alloy exhibits excellent biocompatibility, corrosion resistance, and wear resistance [3], [5] [6], [7], [10], [12]. It has been extensively used in biomedical applications, including orthopedics, dental implants, cardiovascular stents, and orthodontics [3], [5], [7], [11], [16]. NiTi alloy's biocompatibility has been demonstrated through in vivo testing and preclinical experience [3]. It is considered highly biocompatible and has been reported to have good biocompatibility even after surface modifications [3], [5]. However, there have been some concerns regarding the biocompatibility of NiTi alloys, and certain studies have reported cytotoxicity for NiTi alloys[4], [7]. Further research is needed to fully understand and address these concerns. The corrosion resistance of NiTi alloy is an important factor in its biomedical applications [10], [17]–[20]. The alloy forms a protective oxide layer on its surface, which improves its corrosion resistance [21]. However, the corrosion resistance of NiTi alloy can be influenced by factors such as surface treatments, surface conditions, and the presence of impurities [10], [17], [18], [20], [22], [23]. Surface treatments, such as chemical etching and mechanical polishing, can affect the corrosion resistance of NiTi alloy [18], [22]. The alloy's corrosion resistance can also be influenced by its microstructure and composition [23], [24]. Therefore, careful consideration should be given to the surface conditions and treatments of NiTi alloy in biomedical applications to ensure its long-term performance and biocompatibility.

### 1.1. FABRICATION OF NITI ALLOY

The fabrication of NiTi alloy has been explored using various techniques, including plasma arc melting (PAM), additive manufacturing (3D printing), and selective laser melting (SLM) [17], [25]–[28]. PAM has been shown to be a suitable noncontaminating melting route for manufacturing high-quality NiTi alloy [17]. Additive manufacturing techniques, such as SLM, have been used to fabricate near-net-shape NiTi implants with improved properties [25], [27]. These techniques offer the potential for precise control over the microstructure and properties of NiTi alloy,

allowing for the customization of implants for specific applications. In conclusion, NiTi alloy, also known as nitinol, is a commercially available shape-memory alloy that exhibits unique properties, including shape memory effect, superelasticity, and high damping capacity. It outperforms other SMA metals in terms of mechanical and thermomechanical properties. NiTi alloy has been extensively used in various fields, including orthopedics, dentistry, cardiovascular interventions, and aerospace. It exhibits excellent biocompatibility, corrosion resistance, and wear resistance, making it suitable for biomedical applications. However, there are ongoing research efforts to address concerns regarding its biocompatibility and to further improve its properties for specific applications. The fabrication of NiTi alloy has been explored using various techniques, including PAM and additive manufacturing, offering the potential for customized and high-quality implants. Reference [29] provides a comprehensive overview of the engineering aspects of SMAs, including NiTi nitinol. It covers topics such as alloy design, processing techniques, and shape memory behavior.

## 1.2. CORROSION BEHAVIOR OF NITI NITINOL ALLOYS

The corrosion behavior of NiTi nitinol alloys has been extensively studied due to its importance in various applications, particularly in the biomedical field. Nitinol alloys are known for their shape memory effect, superelasticity, and biocompatibility [7], [25]. However, the corrosion resistance of nitinol is a critical factor to ensure its long-term performance and biocompatibility in physiological environments [30].

The corrosion resistance of nitinol is primarily attributed to the presence of a protective oxide layer, mainly titanium dioxide (TiO2), on its surface [30]. The stability and properties of this oxide layer play a crucial role in determining the corrosion behavior of nitinol[30]. The oxide layer acts as a barrier, preventing further corrosion and reducing the release of potentially toxic nickel ions [30], [31]. The stability and thickness of the oxide layer can be influenced by various factors, including surface treatments, heat treatments, and alloy composition [22], [24], [30], [32].

Surface treatments have been explored to improve the corrosion resistance of nitinol alloys. For example, electropolishing has been shown to enhance the corrosion

resistance of nitinol by promoting the formation of a dense and protective oxide layer [33]. Chemical etching and heat treatments have also been investigated to modify the surface conditions of nitinol and improve its corrosion resistance [22], [32]. Plasma arc melting (PAM) has been identified as a suitable noncontaminating melting route for manufacturing high-quality nitinol with improved corrosion resistance [17].

In addition to surface treatments, alloy composition can significantly affect the corrosion behavior of nitinol. The presence of nickel in nitinol alloys can lead to concerns regarding the release of nickel ions, which can have toxic effects [30], [34]. Therefore, efforts have been made to develop nitinol alloys with reduced nickel content or alternative alloy compositions to improve biocompatibility and corrosion resistance [35], [36]. For example, the addition of other elements, such as zirconium (Zr) or molybdenum (Mo), has been investigated to enhance the corrosion resistance of nitinol alloys [24], [35].

Furthermore, the corrosion behavior of nitinol can be influenced by factors such as mechanical deformation, heat treatments, and exposure to physiological environments [32], [37]. Studies have shown that mechanical deformation, such as tensile or compressive loading, can affect the corrosion resistance of nitinol [38]. Heat treatments can also alter the microstructure and properties of nitinol, which can subsequently impact its corrosion behavior [24], [32]. Exposure to physiological environments, such as simulated body fluids, can provide insights into the long-term corrosion behavior of nitinol in biomedical applications [37], [39].

Overall, the corrosion behavior of NiTi nitinol alloys is a complex phenomenon that is influenced by a range of factors, including surface treatments, alloy composition, mechanical deformation, heat treatments, and exposure to physiological environments. Understanding and optimizing the corrosion resistance of nitinol alloys is crucial for their successful application in biomedical devices and other fields. Further research is needed to explore advanced surface modification techniques, alloy design strategies, and long-term corrosion performance evaluation to enhance the corrosion resistance and biocompatibility of nitinol alloys.

## 1.3. MICROSTRUCTURE OF NITI NITINOL ALLOYS

Nitinol is a SMA (SMA) composed of nickel and titanium. It is known for its unique properties, including superelasticity and shape memory effect [40]. The microstructure of Nitinol plays a crucial role in determining its mechanical behavior and functional properties [41]. The alloy undergoes a phase transformation from martensite to austenite, which is responsible for its shape memory effect and superelastic behavior [41]. The transformation temperatures (TTs) and critical properties of Nitinol can be tailored by adjusting the microstructure through processing parameters [40].

The microstructure of Nitinol can be influenced by various factors, including heat treatment, thermomechanical treatment, and additive manufacturing processes [14], [42], [43]. Heat treatment is commonly used to adjust the transition temperatures and control the microstructure of Nitinol alloys [42]. Thermomechanical treatment can also be employed to improve the properties of Nitinol, such as superelasticity, while maintaining the desired microstructure [42]. Additive manufacturing processes, such as laser powder bed fusion (L-PBF), have been used to produce complex Nitinol components with tailored microstructures [40].

The corrosion resistance of Nitinol is another important aspect related to its microstructure. The surface characteristics, including surface finish quality, homogeneity of microstructures, and presence of defects, can affect the corrosion resistance of Nitinol alloys (Yan & Boland, 2006). Nanostructured Nitinol has shown potential for improved corrosion resistance compared to microstructured Nitinol [18]. The mechanical behavior of Nitinol is strongly influenced by its microstructure. The solid-state diffusionless phase transformations and the presence of different phases in Nitinol can result in complex mechanical responses, making it challenging to model and predict the behavior of the alloy [44], [45]. The microstructure, including the presence of equiaxed grains and dendrites, can also affect the fatigue and fracture properties of Nitinol [46], [47].

Various techniques, such as differential scanning calorimetry (DSC), electron backscatter diffraction (EBSD), and X-ray phase analysis, have been used to analyze

the microstructure of Nitinol and understand its properties [41], [43], [48]–[50]. These techniques provide valuable insights into the composition, grain structure, phase distribution, and mechanical behavior of Nitinol alloys. In conclusion, the microstructure of Nitinol alloys is a critical factor that influences their mechanical behavior, functional properties, and corrosion resistance. Heat treatment, thermomechanical treatment, and additive manufacturing processes can be used to tailor the microstructure and control the properties of Nitinol. Understanding the microstructure of Nitinol is essential for optimizing its performance in various applications, including biomedical implants, orthodontic devices, and cardiovascular devices. Further research is needed to explore the relationship between microstructure and properties of Nitinol and develop advanced processing techniques to enhance its performance.

## 1.4. SUPERELASTIC BEHAVIOR OF NITI NITINOL ALLOYS

Nitinol, also known as near-equiatomic nickel-titanium alloy (NiTi), is a unique material that exhibits superelastic behavior and shape memory effects [19], [51]–[54]. These properties are a result of a thermoelastic phase transformation near ambient temperature, martensite twinning, and the inhibition of slip by fine Ni4Ti3 precipitates [51]. The superelastic behavior of Nitinol allows it to recover from large strains and exhibit bone-like behavior, making it suitable for biomedical applications such as bone implants, stents, orthodontic wires, and dental instruments[55], [56].

The mechanical properties of Nitinol, including its superelasticity and shape memory effects, make it a versatile material for various applications. It has high recovery strain, high strength, and a relatively low Young's modulus [51]. The superelastic behavior of Nitinol allows it to undergo large deformations and recover its original shape when the external load is removed [57]. This property is particularly beneficial in applications where continuous force is applied, such as orthodontic treatment and bone fixation [58].

The shape memory effect of Nitinol allows it to "remember" its original shape and return to it when heated above a certain temperature [59]. This property is utilized in

various applications, including biomedical devices and actuators [60]. The shape memory effect is a result of the reversible martensitic phase transformation in Nitinol [5].

The unique properties of Nitinol are attributed to its microstructure and composition. The presence of fine Ni4Ti3 precipitates inhibits slip and enhances the superelastic behavior [51]. The stability and behavior of Nitinol in the physiological environment are primarily dependent on the properties of the TiO2 oxide layer that forms on its surface [30]. The microstructure of Nitinol can be tailored through processing parameters, such as additive manufacturing, to achieve desired properties [44].

However, there are some concerns regarding the biocompatibility and corrosion resistance of Nitinol, particularly due to the release of nickel ions [61]. Nickel is known to have toxicological effects, and its presence in Nitinol raises concerns for certain individuals who are hypersensitive to nickel [57]. Research is ongoing to improve the biocompatibility and corrosion resistance of Nitinol through surface treatments and alloy modifications [62].

In conclusion, Nitinol alloys, with their superelastic behavior and shape memory effects, have found extensive applications in various fields, including biomedical devices, orthodontics, bone implants, and stents. The unique properties of Nitinol are a result of its microstructure, composition, and thermoelastic phase transformation. Ongoing research aims to further enhance the biocompatibility and corrosion resistance of Nitinol for its continued use in biomedical applications.

SMAs, such as Nitinol, exhibit unique properties, including shape memory effect and superelasticity, which make them suitable for cardiovascular implants. These alloys can undergo large deformations and recover their original shape upon heating. Shape memory polymers, on the other hand, can be programmed to change their shape in response to external stimuli, such as temperature or pH. Both types of smart materials have shown promise in various cardiovascular implant applications, including stents, occludes, and heart valves. However, there are challenges that need to be addressed, such as biocompatibility, fatigue resistance, and long-term stability, to ensure the

successful implementation of these materials in cardiovascular implants. Further research and development are needed to optimize the properties and performance of SMAsand shape memory polymers for cardiovascular applications.

In this study, the microstructure of the sheet metals with a wall thickness of 0.3 mm of the SMA was examined by optical microscope, SEM, and the strength of the macrotexture was measured using XRD. In addition to this, potentiodynamic and immersion corrosion tests of sheet materials were carried out in a 3.5% NaCl environment. Also, at room temperature, back-and-forth direction dry environment and corrosive wear tests were carried out. In addition, DSC test, SEM, and XRD examinations were performed.

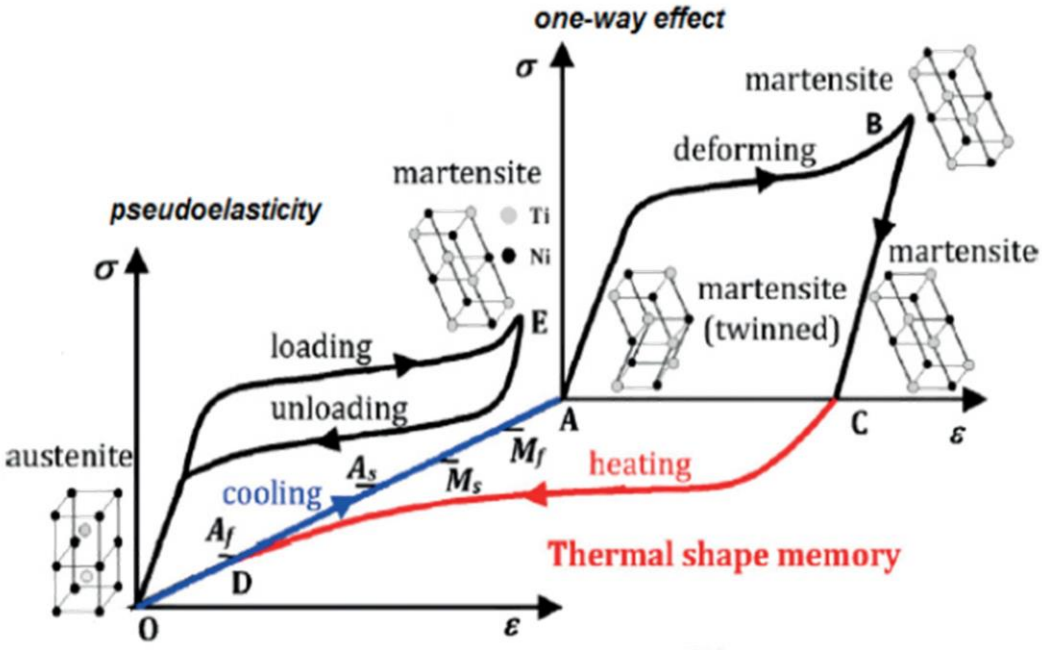


Figure 1.1. The stress-strain curve characterizing the shape memory and superelastic behavior of NiTi [44].

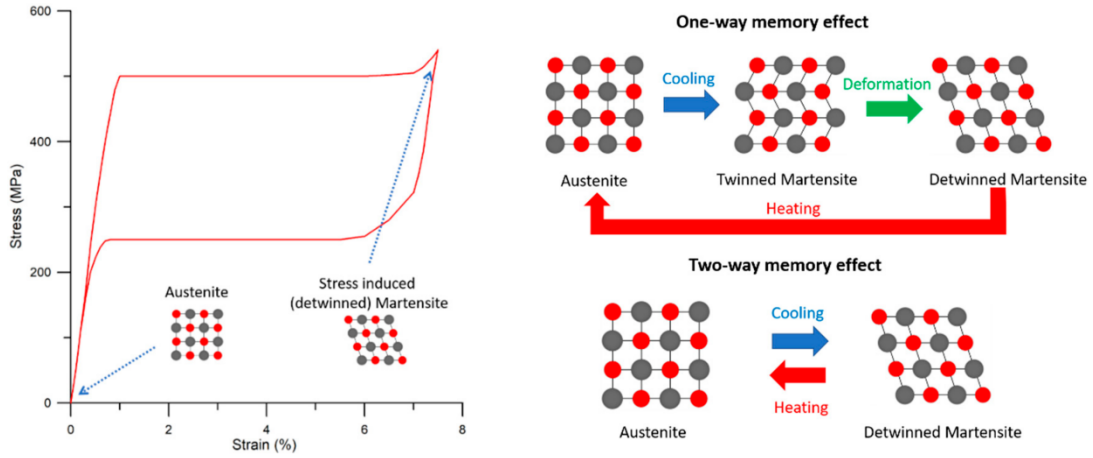


(a) (b)

Figure 1.2. Phase change of the nitinol [63].

Table 1.1. Chemical constituents of SMA [64].

| **Ni** | **Ti** | **C** | **O** | **Si, Co, Mn, Cr, W, V Mo,** | **Al, Ta, Hf Cu, Nb, Zr,** | **Bi, Mg, Pb, Sn, Cd Ag, Ca,** | **Zn, Be, Sr, As, Ba Na, Sb,** | **B** | **Fe** |
|---|---|---|---|---|---|---|---|---|---|
| **55** | 44 | 0.05 | 0.05 | 0.01 | 0.01 | 0.01 | 0.01 | 0.001 | 0.5 |

Table 1.2. Mechanical characteristics of NiTi alloys at (*Ms*−15 °C) [65].

| **Alloy** | **Ductility/ %** | **Ult. Strength (Mpa)** | **Yl. Strength (Mpa)** |
|---|---|---|---|
| **Ni42.5Ti42.5Nb15** | 21.6 | 801 | 289 |
| **Ni45Ti45Nb10** | 26.6 | 836 | 231 |
| **Ni47.5Ti47.5Nb5** | 24.7 | 805 | 182 |
| **Ni50Ti50** | 32.4 | 801 | 192 |

Rolling changes some properties of Nitinol as seen Table 1.3

Table 1.3. Mechanical features and As and Ms temperatures of some nitinol alloys [65].

| Type | *As* °C | *Ms* °C |
|---|---|---|
| **Ni50Ti50** | 88 | 58 |
| **Ni41Ti44Nb15** | 56 | 23 |
| **Ni42.5Ti42.5Nb15** | 40 | 4 |

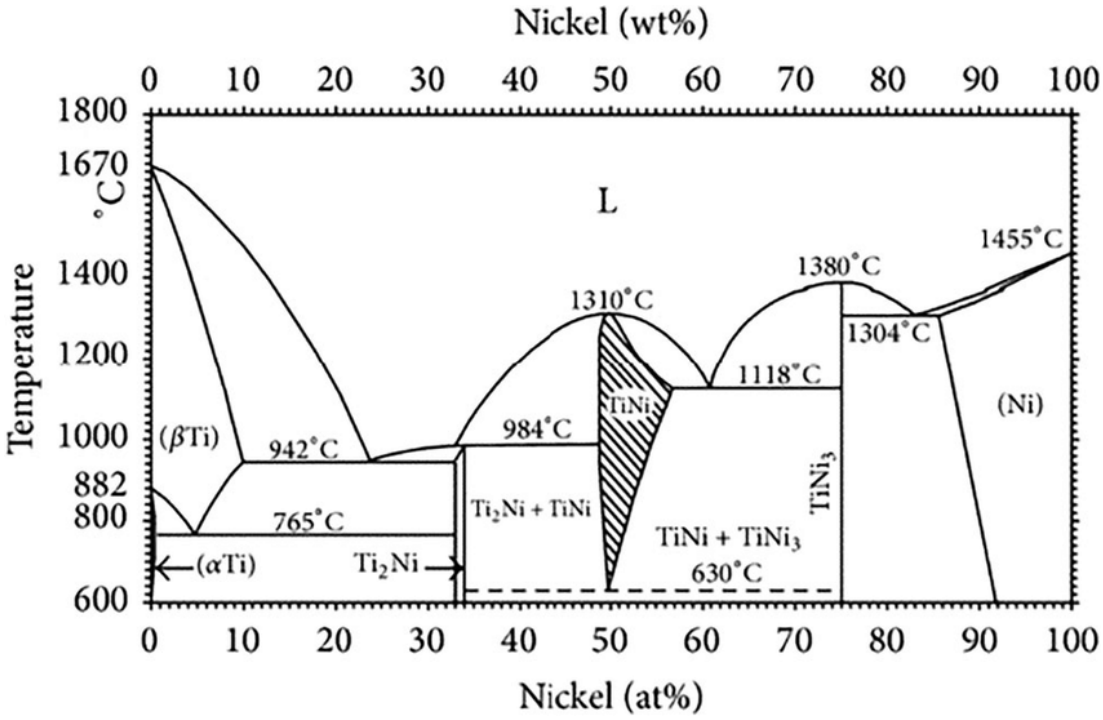


Figure 1.3. Ni-Ti alloy's phase equilibrium diagram [66].

In order to give the desired memory shape by heat treatment, temperatures between 500ºC-800ºC are often preferred, and this temperature value should be at least 300ºC-350ºC with the setting of sufficient time. During the heat treatment of the SMA, it is required to act in a controlled manner to give the requested memory shape. Otherwise, the memory effect cannot be gained. The maximum memory effect gained is limited by strain and/or strain and the amount of cycling required.

## 1.5. TREATMENT OF NITI SMA ALLOYS

They are alloys that can return to their original state with the appropriate temperature after undergoing a change in shape depending on the temperature and are sensitive to

thermal change [63]. The temperature limit causing the change depends on the properties of each alloy. However, commercially available products generally respond to temperatures between 35°C and 90°C [69].

SMAsare available in two different types: unidirectional memory and bidirectional memory. Unidirectional memory means that alloys can return to their original shape after being heated and retain their shape when cooled again, while in bidirectional memory, alloys can change shape alternately by memorizing both high and low-temperature shapes at the same time [67]. Figure 1.3 shows the one-way shape memory event.

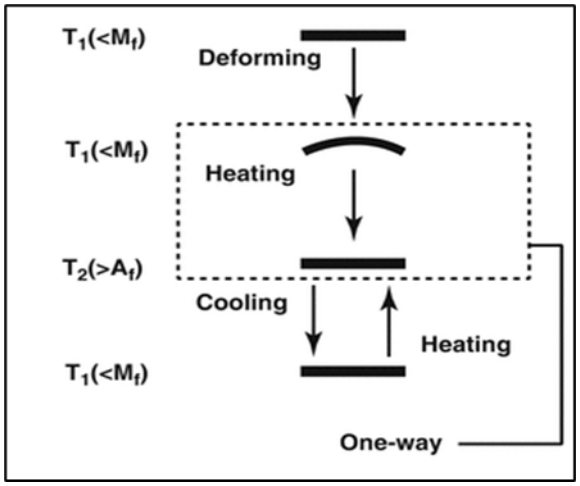


Figure 1.4. Shape memory event: One-way.

When the alloy is deformed at a temperature below the martensite finish temperature (T < Mf), the sample cannot return to its original state if the externally applied stress is removed. Even if the temperature starts to decrease again, the sample cannot regain its deformed shape. In other words, in cooling below the martensite's initial temperature, the structure turns into the martensite phase but does not undergo any deformation. This type of shape memory mechanism is called a one-way strain event [33].

As seen in Figure 2.4, shape change is observed in SMAsthat are deformed in the sample martensite phase (at T<Mf temperature). As a result of the removal of the applied force, the sample cannot return to its original shape, but when the temperature

is above the austenite finish temperature (T >Af), the alloy returns to its original shape. If the sample cannot regain its deformed shape when the temperature is lowered back below the martensite's initial temperature, this type of shape recall feature is called a one-way shape memory event [73]. One-way shape memory is also called irreversible shape memory event. The unidirectional shape memory phenomenon occurs in many alloys. Examples of these alloy systems are NiAl, NiTi, CuZn, TiNb, CuZnSn, CuZnSi, and FeMnC, FePt [74].

Some of the SMAs can show a two-way recall effect. The martensite transformations observed in such alloys show bidirectionality depending on the effect of applied pressure and temperature. Because of their reversibility, these alloys exhibit mechanical behavior, unlike other alloy systems. These alloys can remember their shape at a temperature above the austenite transformation end temperature and at a low temperature below the martensite transformation temperature. For this reason, bidirectional SMAs are materials that can remember their geometric shapes without the need for any external stress during repetitive heating and cooling processes [75-76].

A sample that is completely in the martensite phase below the Mf temperature can be given the desired shape with force applied from the outside. Despite the removal of the applied force, the specimen continues to maintain its deformed shape. When the temperature of the deformed sample is increased above the austenite finish temperature, the plastic deformation disappears, and the sample returns to its pre-deformation shape. If the temperature of the sample is lowered to the martensite finish temperature, it regains its deformed shape. This event is called a bidirectional shape-memory event. Figure 1.5 shows the schematic representation of the bidirectional shape memory event. In short, the material takes the shape of the phase formed as a result of repeating each heating and cooling process [77].

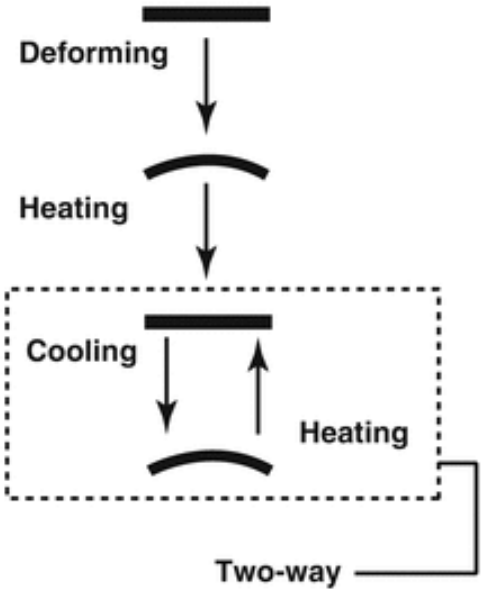


Figure 1.5. Bidirectional shape memory event.

## 1.6. SHAPE MEMORY TRAINING

Some SMAs inherently exhibit two-way shape memory. A complex shape memory training called "Training", which consists of the following process steps, is performed in order for some alloys with two-way shape memory to show a two-way shape recall effect (Figures 1.6 and 1.7).

- Extreme deformation in the martensitic state
- Shape recall cycle (Cooling>Deformation>Heating>Repetition)
- Pseudo-elastic cycle (Load>Unload>Repeat)
- Unified shape memory and pseudo-elastic cycling
- Rotation insertion of deformed martensite under the influence of stress and temperature
- Constrained and constrained aging over long periods of time (causes purely shape recall effect, little different from bidirectional shape recall effect).

There are some limitations to be considered in obtaining two-way shape memory.

These are;

- Reversible deformation usually remains around 2%. This rate is less than what is seen around 6% in unidirectional shape memory.
- Transformation forces during cooling are quite small.
- Shape memory can be lost with very little overheating (less than 250°C).
- The long-term fracture and stability properties are not well known.

There is a permanent temperature hysteresis during the heating and cooling cycles.

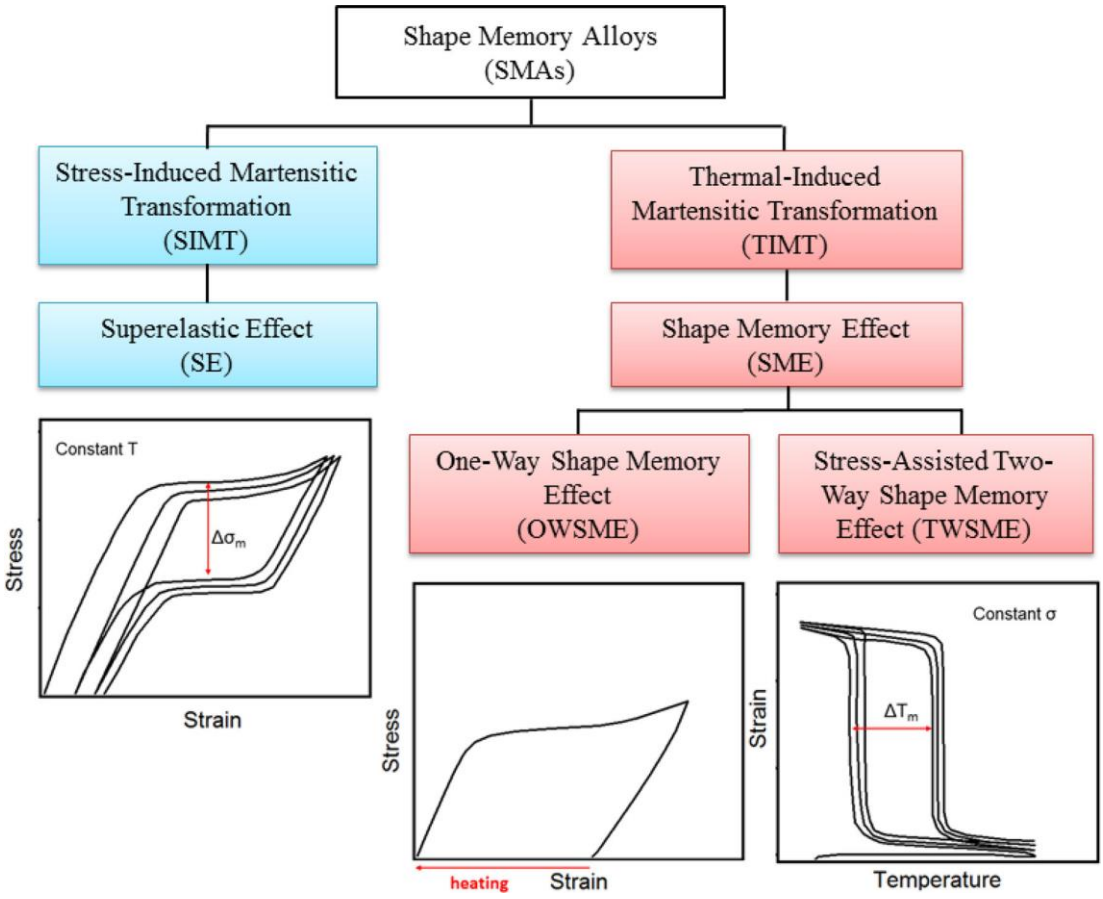


Figure 1.6. Heat treatment to achieve bidirectional shape memory effect [68].

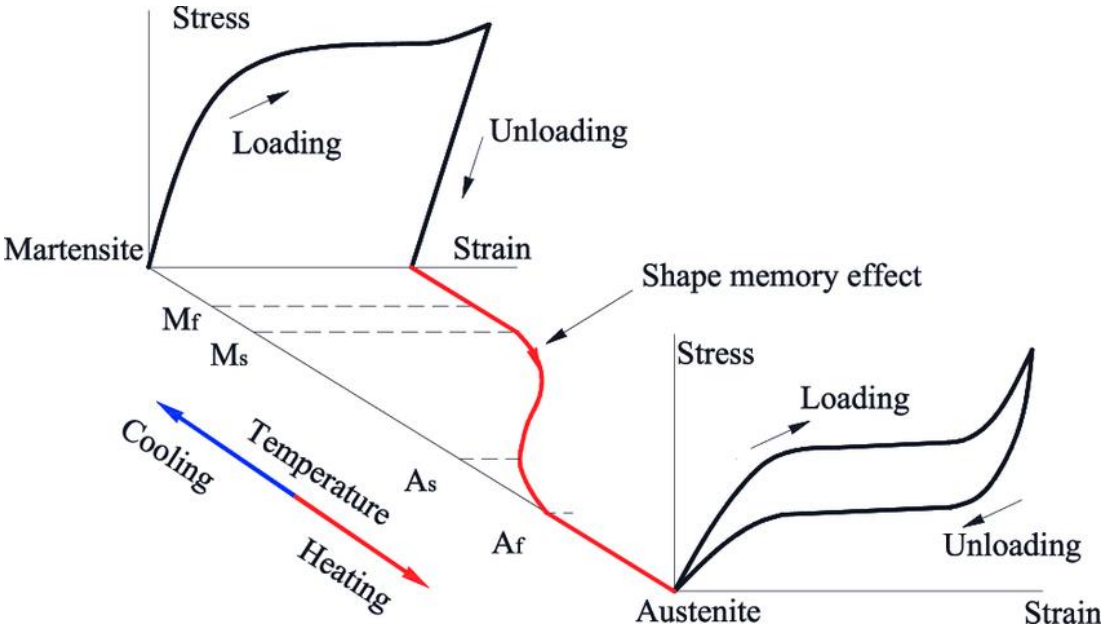


Figure 1.7. Typical thermomechanical behavior of SMA [69].

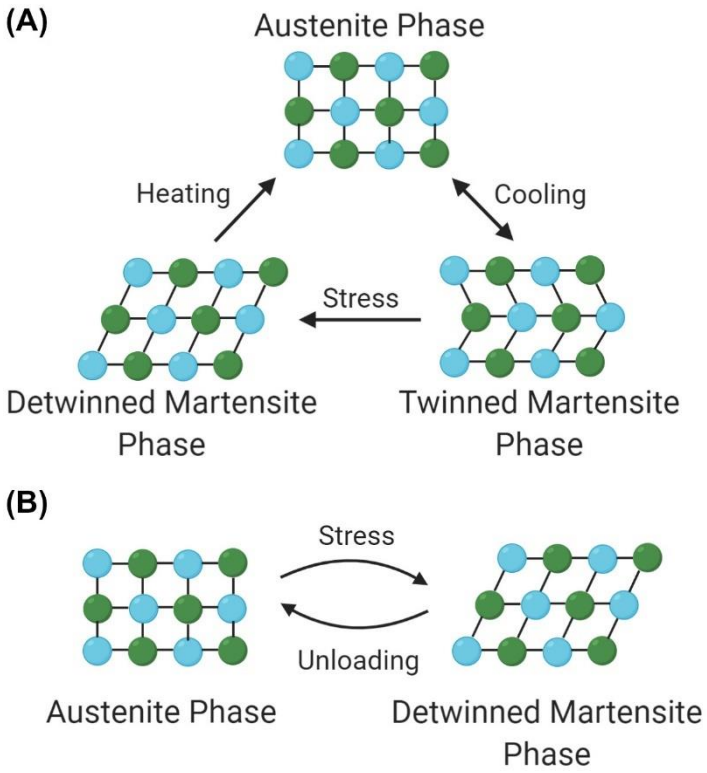


Figure 1.8. Views of the two phases of the SMA [70].

# PART 2

# ANA BAŞLIK

## 2.1. PRODUCTION METHODS OF NICKEL-TITANIUM SMA

Titanium, one of the constituents of the nickel-titanium SMA, is a metal that has managed to become one of the most used materials in the world. Titanium melts at 1670°C, has a specific gravity of 4.5 g/cm³, and has high corrosion resistance even at temperatures reaching up to 400°C. Pure titanium is mostly used for corrosion resistance. Due to using area, it can show low tensile strength and high forming ability. With alloying elements added to pure titanium, the tensile strength increases up to 700 MPa, and the ductility of titanium decreases to 20%. Pure titanium, with a purity of 99.5%, passes into the alpha phase at room temperature in a tightly ordered hexagonal structure and transforms into a volume-centered cubic β phase at 885°C. The melting temperature of pure nickel is 1455°C, and the most important technical feature of pure nickel is its corrosion resistance. The recovery of pure nickel is by roasting and reduction processes from large amounts of sulfide ores. Plastic shaping of nickel is generally similar to shaping austenite steel, but in the pure state, it can make some differences due to its high chemical affinity, for example, to Sulfur. For example, during heat treatment, sulfur from combustion gases or excess cutting fluids on the surface of the part diffuses along the grain boundaries of the nickel and precipitates as Sulphide. Depending on the environment, corrosion damage may begin, and the damage is concentrated at the grain boundaries where the precipitates are located. The mechanical strength of titanium alloys is approximately 2.5 times that of aluminum alloys and is equivalent to some alloy steels. Its modulus of elasticity is 110 GPa, with higher ductility and toughness than aluminum alloys. In the production of nickel-titanium SMAs, two different methods are used: the casting method and the sintering method. Production by casting method; vacuum induction method, vacuum arc method, electron beam arc method, and plasma arc method. In the production of the

alloy, first and foremost, nickel and titanium metals with commercial purity higher than 99.5% must and must be used.

Titanium reacts easily with oxygen from 900°C. For this reason, nickel-titanium alloys must be cast in a vacuum or a protective gas atmosphere. Electric furnaces from foundry furnaces; Arc furnaces are divided into three groups induction furnaces and resistance furnaces. Arc and induction furnaces can reach higher temperatures than resistance furnaces.

## 2.2. PRODUCTION WITH VACUUM ARC METHOD

The heat released from an electric arc created in the furnace is utilized in the use and melting of metal in arc furnaces. If the electric arc is formed between two electrodes, it is referred to as an indirect arc, and if it is formed between electrons and molten metal, it is referred to as a direct arc furnace.

Figure 2.1. Arc Furnace.

In the direct arc furnace, the voltage applied to the electrodes is low, and the current is quite high. Although direct arc furnaces are generally preferred for melting steels and alloyed cast irons, indirect arc furnaces are generally used for melting non-ferrous metals. Andreasen and Fahl applied and used vacuum induction and vacuum arc techniques in 1987 to ensure the quality and purity of the sample piece. The metals to be cast were first melted in a vacuum induction furnace at 1400°C. If it is then melted and solidified again in the vacuum arc furnace, homogeneity is achieved.

## 2.3. PRODUCTION WITH VACUUM INDUCTION METHOD

Induction furnaces are divided into two groups, core and coreless, and in the coreless induction furnace, the crucible is surrounded by a coil made of water-cooled copper pipe. In the channel type, i.e., the coreless type, the liquid metal forms a channel around the core of the primary winding. The electrical efficiency of these furnaces is much higher. This type of furnace is generally preferred not for melting, unlike others, but for holding and overheating.

Figure 2.2. Vacuum Induction Furnace

In both mentioned induction furnaces, the molten metal is surrounded by an electric coil, which can be thought of as the primary winding of a normal transformer. The alternating current flowing through this coil generates heat by stimulating or inducing eddy currents in the conductive liquid metal, which can be thought of as secondary winding. Graphite has high thermal conductivity and is, therefore a more preferred crucible material compared to other Mold materials. Alumina or magnesium oxide (MgO) are not suitable crucible materials since they will give oxygen to the metal that becomes liquid with the effect of heat. In the case of using graphite, the casting temperature must not exceed 1450°C in any way so that no carbon is dispersed into this alloy. In this case, since the Ni-Ti melting temperature is 1310°C, in other words,

it does not exceed 1450°C, the casting will be made using a graphite crucible. In casting at this temperature, approximately 200-500 ppm will be mixed into the material. Carbon will not affect the physical properties of the material [68].

During the production made by [71], 99.7% purity Ti and 99.98% purity Ni were cast in a graphite crucible in a high-frequency induction furnace. The composition of the nickel-titanium alloy obtained during this casting was 50.7% of nickel and 49.3% of titanium by atom. The composition of the alloy produced in the vacuum induction furnace by [71] using 99.7% pure titanium metal and 99.97% pure nickel metal was found to be 49.4% titanium and 50.6% nickel atomically.

## 2.4. PRODUCTION BY ELECTRON BEAM ARC METHOD

The electron beam arc method, which is applied as an alternative method to the other methods described, is a type of method used in the melting of high-temperature-resistant materials since the 1950s. These materials are Ta, Nb, W, Ti, Zr, and Hf. In the melting technique with this method, the electrons of the focused beam collide with the metal surface consisting of pure nickel and titanium metals at extremely high speed. As a result of the heating of the solid metal, a large increase in the kinetic energies of the atoms in the crystal lattice occurs. Since electrons are such small masses, they actually transfer their energy to the rather heavy nuclei of the crystal atoms in the process of impact. After this first step in energy transfer, the conduction electrons gain collision energy and initiate the melting event. A cylindrical nickel-titanium alloy with a diameter of 40 mm and a length of 270 mm was obtained at the end of two repeated castings with 54.7% nickel by weight using the electron beam arc method made by [72].

## 2.5. PRODUCTION WITH PLASMA ARC METHOD

With the arc formed between the tungsten cathode and the nickel-titanium feed metal in an inert gas atmosphere, the gas flowing from around the cathode to the center of the anode is ionized and forms the gas plasma. In order to keep oxidation at minimum levels, the process is carried out in an inert gas atmosphere.

## 2.6. PRODUCTION BY SINTERING METHOD

Powder metallurgy in Ni-Ti production; is applied in two different ways as pure metal sintering and alloy sintering. In the pure metal sintering application, pure powders of the two metals are mixed and pressed, and sintered. And the homogeneity of the composition, in this case, becomes low. In alloy sintering, pre-prepared alloy powder is used. In this case, the homogeneity to be achieved is much higher than necessary. The plasma-rotary electrode method is a suitable method for producing high-quality powders. This method ensures that the alloy, which starts to melt, is scattered in droplets and atomized by rotating the electrode from the alloy heated by plasma arc welding at high speed. This solidified powder is sintered by the hot isostatic press method at approximately 840°C. The alloy obtained by this method is exactly in the quality of alloys produced in a vacuum. For the production of Ni-Ti SMA, there are three stages that should be considered as a priority. These are, respectively, the composition ratio of the alloy, hot-cold forming processes, and shape memory-giving processes to the alloy. Hot forming of the alloy is carried out at approximately 700°C to 900°C. This process is generally hot formed as wire, sheet, and bar. There is no need for a vacuum environment for hot forming processes. By means of heat treatments applied to the alloy, it is ensured that the alloy takes the desired shape memory. As a result of these processes, known as shape memory acquisition processes, the Ni-Ti alloy is made ready for use in the desired area by taking the shapes gained with temperature changes. In the production of Ni-Ti made by Bram et al in 2002 using the sintering method, Ni-Ti powders smaller than 45μm are kept at 1050°C for 5 hours under 195 MPa pressure. Afterward, it was kept at 850°C for about 1 hour, and after it was subjected to solution heat treatment, it was kept at 500°C for 1 more hour, and water-cooled heat treatment was passed.

# PART 3

# EXPERIMENTAL STUDY

## 3.1. MATERIAL

Nitinol sheet material of 3 mm thickness and 30 cm length with 25ºC and 35ºC conversion temperatures used in the study was obtained from "Kellogg's Research Labs". NiTi alloy, composition as ingredients ASTM F 2063-12. The main material used within the scope of the doctoral thesis is nitinol, whose chemical composition is given in Table 3.1 and contains 55.6% nickel atomically.

## 3.2. MICROSTRUCTURE TEST

The microstructure test of the NiTi superalloy involved cutting a sample measuring 13 × 10 × 0.3 mm from a larger NiTi SMA sample measuring 25.6 × 100 × 0.3 mm. The cut sample was then placed in a silicon mold and treated with bakelite resin and stiffening liquid. The Bakelite sample surfaces were sequentially sanded using sandpaper with grit sizes of 600, 800, 1200, 2000, and 2500. This was performed using a metallography machine, followed by polishing with diamond water. The polished samples was immersed in a solution containing 1 ml of HF, 4 ml of Nitric acid, and 5 ml of ethanol. It was etched for a duration of 90 seconds. The acidified sample was extracted from the solution and subsequently cleaned with alcohol. Its microstructure was then observed and documented using a microscope, capturing photographs at magnifications of 20x and 50x. The Nikon Eclipse MA200 optical microscope was utilized for this study.

Table 3.1. Standard High purity ASTM F 2063-12 requirement wt. %.

| Alloy | Ti | Ni | C max | Co, Fe max | Nb max | Si max | Cu, Cr max | Sn max | O + N max | Al. max | H max | Mn, Mo, W max | S max |
|---|---|---|---|---|---|---|---|---|---|---|---|---|---|
| | bal. | 55.6, | 0.0020 | 0.0050 | 0.005 | 0.0025 | 0.0050 | 0.0100 | 0.0252 | 0.0057 | 0.0015 | 0.0050 | 0.0010 |
| | bal. | 56.0, | 0.050 | 0.050 | 0 | | 0.010 | | 0.0060 | 0.0050 | 0.0012 | 0.0050 | |
| | bal. | 54.5 | | | 0.025 | | | | 0.050 | | | 0.0050 | |
| | bal. | 57.0 | | | | | | | 0.050 | | | 0.0050 | |

Figure 3.1. Nikon Eclipse MA200.

### 3.3. X-RAY DIFFRACTION (XRD) TEST

To analyze the chemical spectrum and texture of the SMA phases, appropriately sized samples were cut and their surfaces cleaned using standard metallographic procedures. The KBU Iron and Steel Institute utilized the Ultima IV model X-ray diffraction (XRD) device. X-ray diffraction (XRD) analysis was conducted using an XRD device within the angular range of 15-90°, and the obtained results were subsequently analyzed. The Rigaku Ultima IV -X-Ray Diffraction Spectrometer measuring instrument used in this study (Figure 3.2).


Figure 3.2. X-Ray Diffraction Spectrometer measuring instrument: Rigaku Ultima IV.

### 3.4. SEM-EDX TEST

Along with the tests carried out after the preparation of the specimen, SEM-EDX tests of the specimen were performed and information about the contents of the materials was obtained. Test results are given in the following sections.

### 3.5. CORROSION TEST

#### 3.5.1. Immersion Test

A 13×10×0.3mm sample has been obtained by cutting a NiTi SMA sample measuring 25.6×100×0.3mm. The sample's surface was polished using 2500-grit sandpaper and subsequently cleaned with alcohol using ultrasonic technology. The initial weight was measured using a precise electronic balance with an accuracy of 0.1 mg and placed in a body fluid environment. The sample was removed from the solution every 24 hours and cleaned by immersing it in a mixture of 50% H2SO4 and 50% HCl acid in an ultrasonic device for approximately 8 minutes. It was then gently brushed in distilled water and alcohol, and finally dried. The immersion corrosion examinations are

assessed by quantifying the weight loss and determining the change in sample thickness. The duration of the test time frame is 10 days.

### 3.5.2. Potentiodynamic Polarization Test

In the potentiodynamic polarization examinations conducted on the NiTi super material, one side of the sample surface measuring 8×8 mm2 was exposed to the atmosphere, while the other surface was shaped together with copper wire. In the experimental setup, the test cell (Isotherm 3.3) consists of a 250ml beaker. The test sample is used as the working electrode, while a graphite rod serves as the counter electrode. Additionally, a saturated calomel electrode (SCE) is employed as the reference electrode. In all experimental studies, particularly those without current flowing through the system, both reference and working electrodes were submerged in a 3.5% simulated body fluid (SBF) solution at room temperature. The change in corrosion potentials, measured in millivolts (mV), between the two electrodes was recorded during current flow. Potentiodynamic polarization curves were generated within the voltage range of -0.25V to +0.25V, using a scanning speed of 1mV/s. The curves were recorded starting from the cathodic direction and progressing towards the Ecorr direction, after achieving the equilibrium potential. The potential for corrosion (Ecorr) and the density of corrosion currents (Icorr) were determined through the analysis of Tafel curves. Three tests were conducted on the Gamry Equipment potential dynamic polarization examination device for all parameters, and the arithmetic mean of the obtained results was calculated. The duration of the experiment spanned 23 days. The study utilized a Gamry system PC4/300 mA potentiostat/galvanostat examiner with controlled by a computer DC105 corrosion analysis (Figures 3.3 and 3.4).

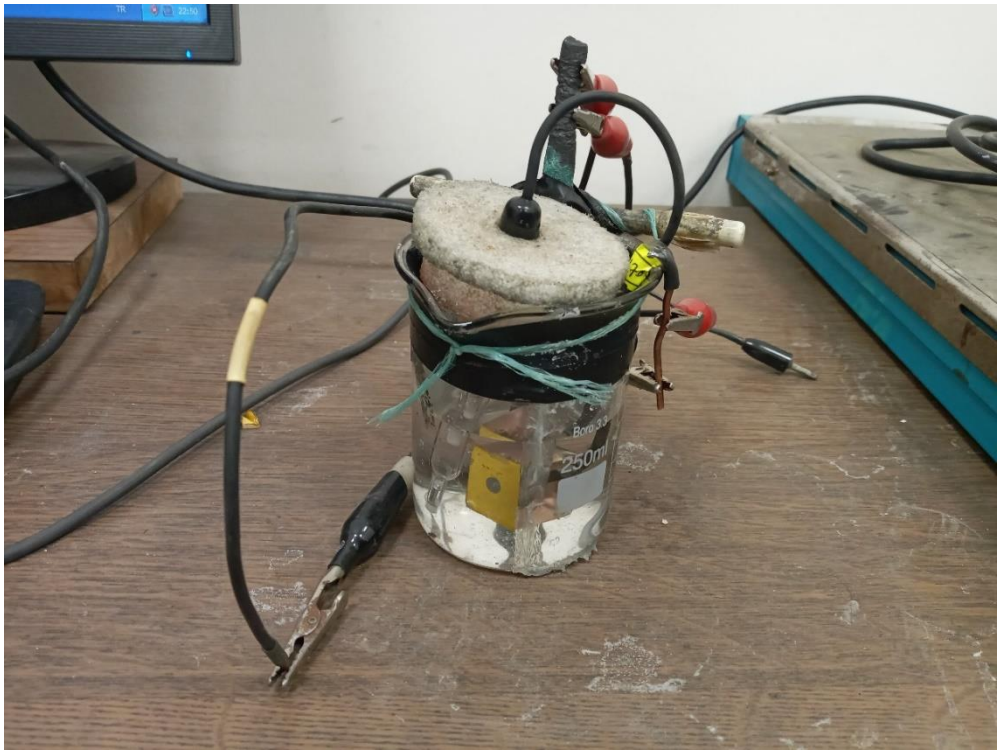


Figure 3.3. Gamry system PC4/300 mA potentiostat/galvanostat test rig.

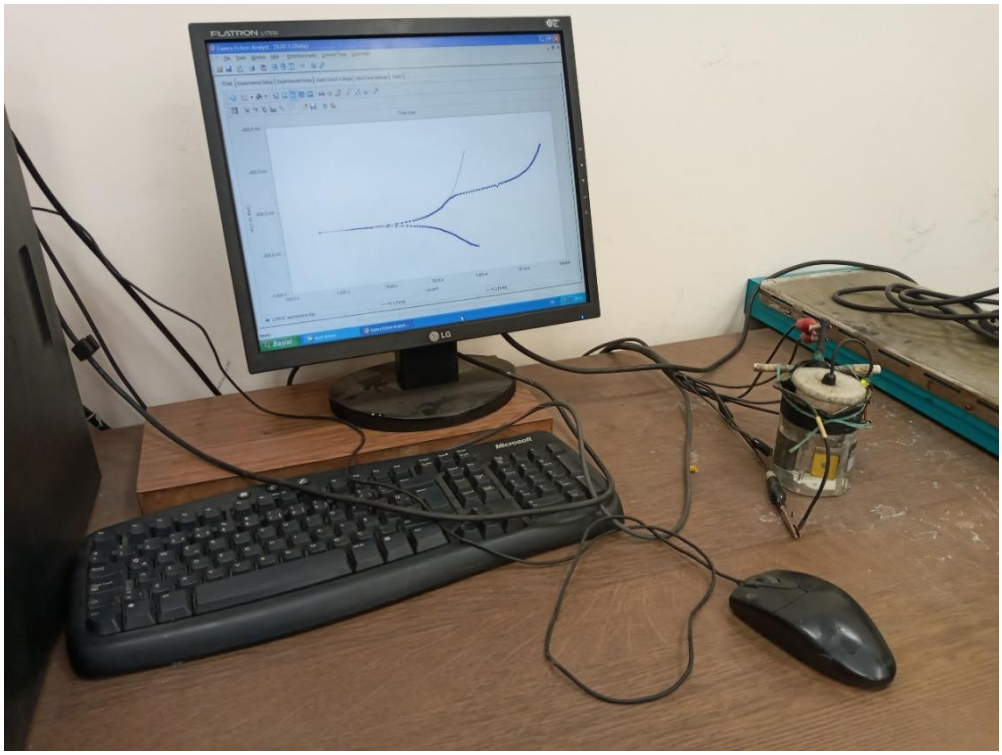


Figure 3.4. Tester with computer-controlled setup.

### 3.6. WEAR TEST

Reciprocating wear tests were conducted on the investigated NiTi super alloy for 20N and 40N loads in both dry and body fluid environments. A 13mm sample surface was subjected to wear testing using a 100CR6 high-quality steel ball as the counter material. The sliding speed was set at 0.04m/s, and the total distance traveled during the test was 300 meters. The wear results were assessed using weight loss measurements. The weight loss was measured prior to and following the experiment using an electronic accurate balance with a sensitivity of 0.1 MG. Furthermore, the width of the track and durability were assessed using a wear family profilometer instrument to quantify the wear losses, specifically the reduction in the area of the wear track. The wear mechanism was evaluated using a scanning electron microscope. The study utilized a device (Figure 3.5) that employed forward-backward motion to conduct a wear test on AISI 52100 steel balls.


Figure 3.5. AISI 52100 steel ball abrasion tester.

### 3.7. DSC (DIFFERENTIAL SCANNING CALORIMETRY)

The DSC method was employed at KBU Iron and Steel Institute to analyze the shape memory effect in an alloy. This involved determining change temperatures, transition from phase to phase temperatures, kinetic parameters, such as enthalpy and entropy values, and investigating the impact of the process of aging on these parameters. Measurements were conducted using the Hitachi Differential Scanning Calorimeter DSC7000 SERIES device. The energy changes occurring in the sample in DSC measurements are endothermic and exothermic. The Hitachi Differential Scanning Calorimeter (DSC) measuring device used in this study (Figure 3.6).


Figure 3.6. Hitachi Differential Scanning Calorimeter.

# PART 4

# RESULTS AND DISCUSSION

In this section, microstructure results, SEM, EDS, XRD, potentiodynamic polarization corrosion test results, Abrasion test results and DSC test results are shared.

## 4.1. MICROSTRUCTURAL RESULTS

Figure 4.1a and 4.1b present the optical microstructures of the examined alloy at minimal magnification (10x) and elevated magnification (50x), respectively. The direction twinned martensite (detwinning martensite) was noticed during the transition from the austenite phase to the martensite phase in the material structure.

Figure 4.1b illustrates the detwinning martensite form within the specified rectangular area. The oriented twin martensite, which is the primary deformation mechanism for superelastic deformation and is consistent with the findings of [72]. The microstructure analysis reveals multiple phases, which are attributed to the localized condensation of titanium and nickel. Kaya et al. [73] identified the presence of NI4Ti3 and austenite as phases. The study found that the dark regions exhibited the Ni4Ti3 phase at lower temperatures, whereas the light regions displayed the austenite phase. This study demonstrates the presence of distinct grain boundaries and the formation of precipitates. The XRD analysis reveals the presence of Ni4Ti3, Ni3Ti, and NiTi2 as precipitates.

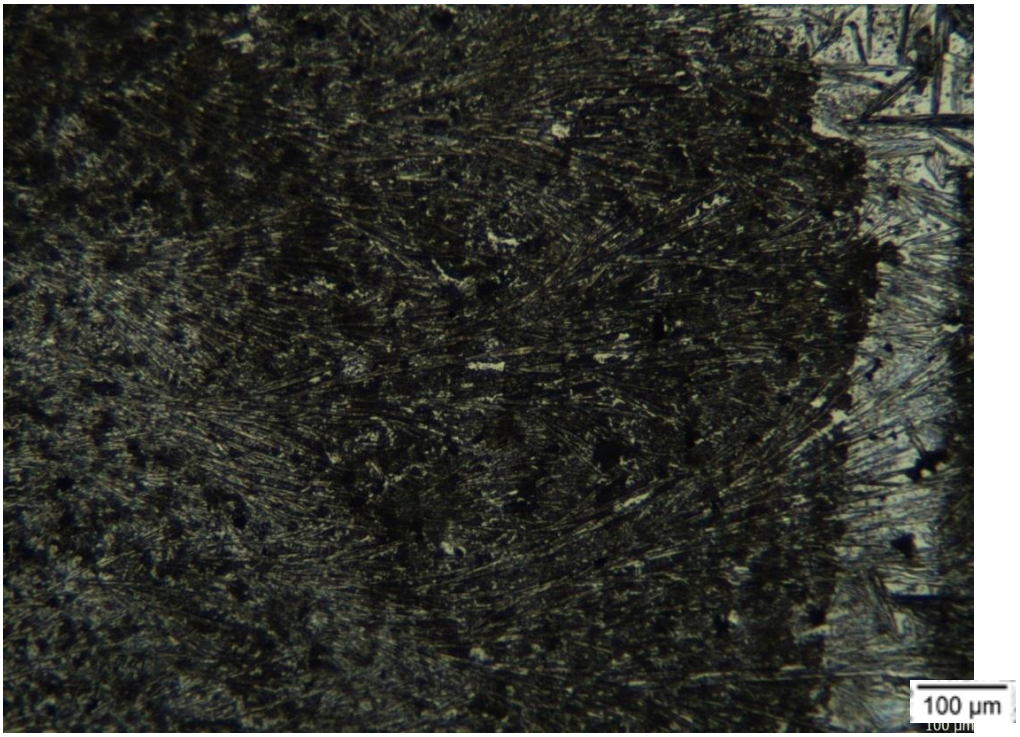


(a)

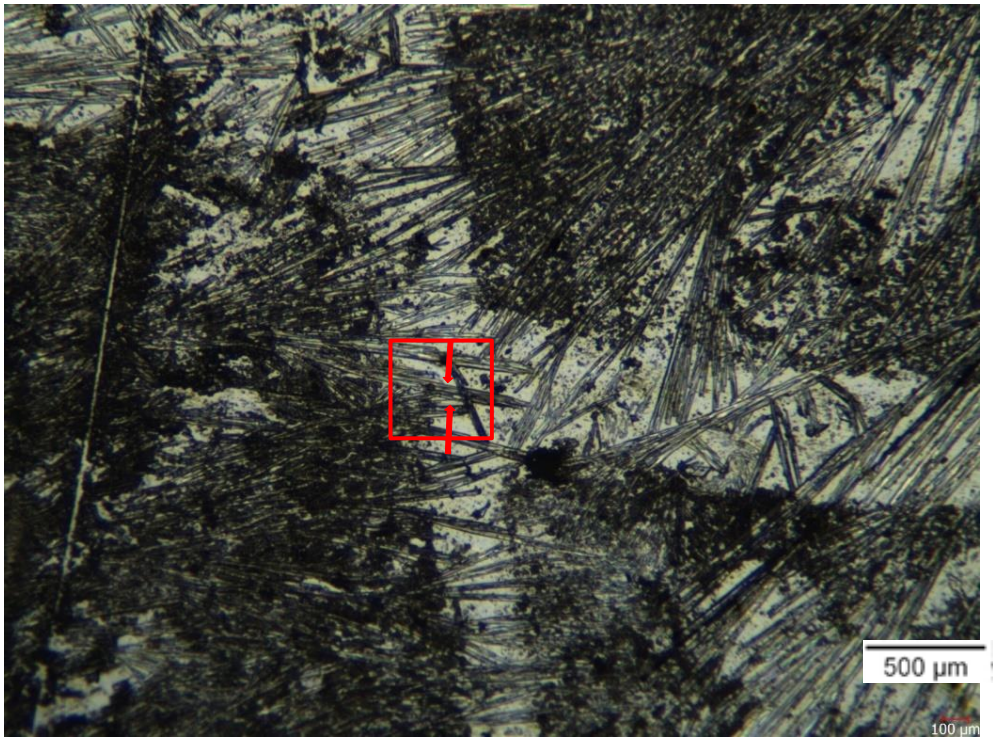


(b)

Figure 4.1. (a): Low-magnification (10X) optical microstructure image of the alloy under investigation. (b): High-magnification (50X) optical equipment micro structure image of the alloy under investigation. The arrow and geometric drawing depict detwinning martensite zones.

The scanning electron microscopy (SEM) images and energy-dispersive X-ray spectroscopy (EDS) analysis outcomes of the shape memory alloy (SMA) are provided in section 4.2. The surface resulting from the intersection of individual traces is both smooth and impermeable. Furthermore, the observed samples displayed a white-gray surface.

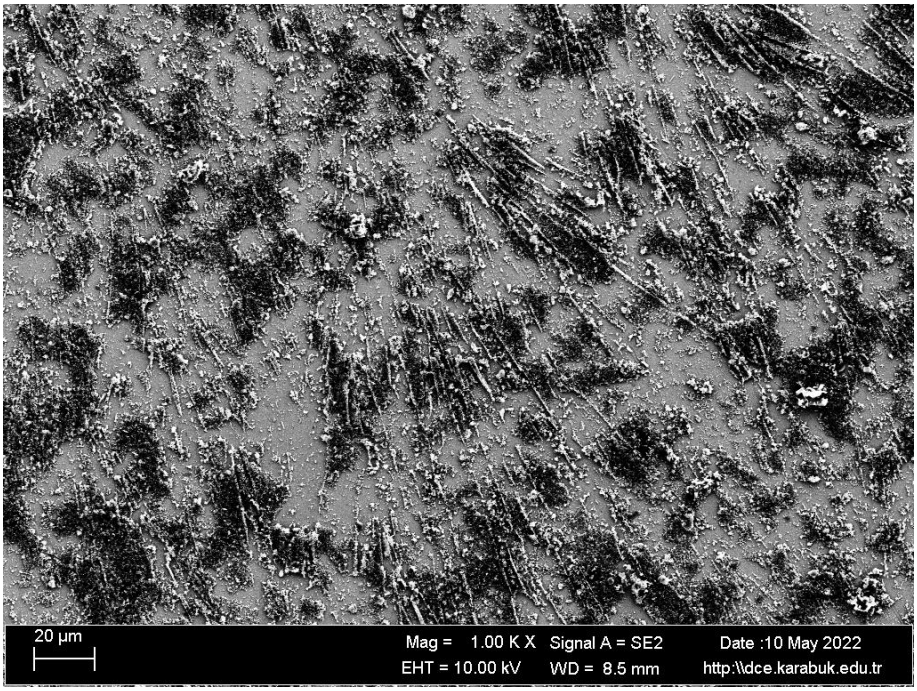


(a)

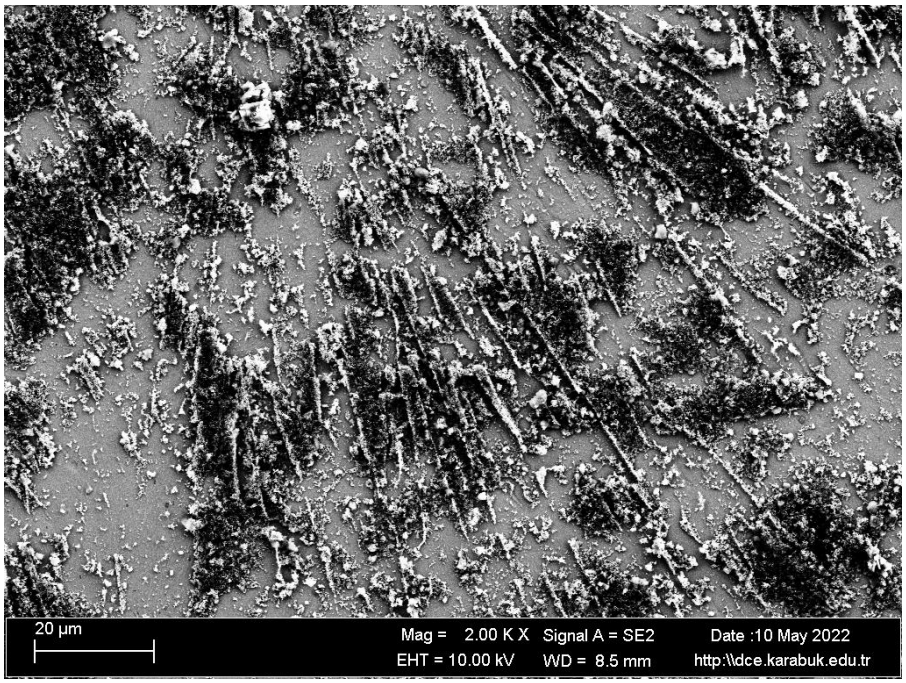


(b)

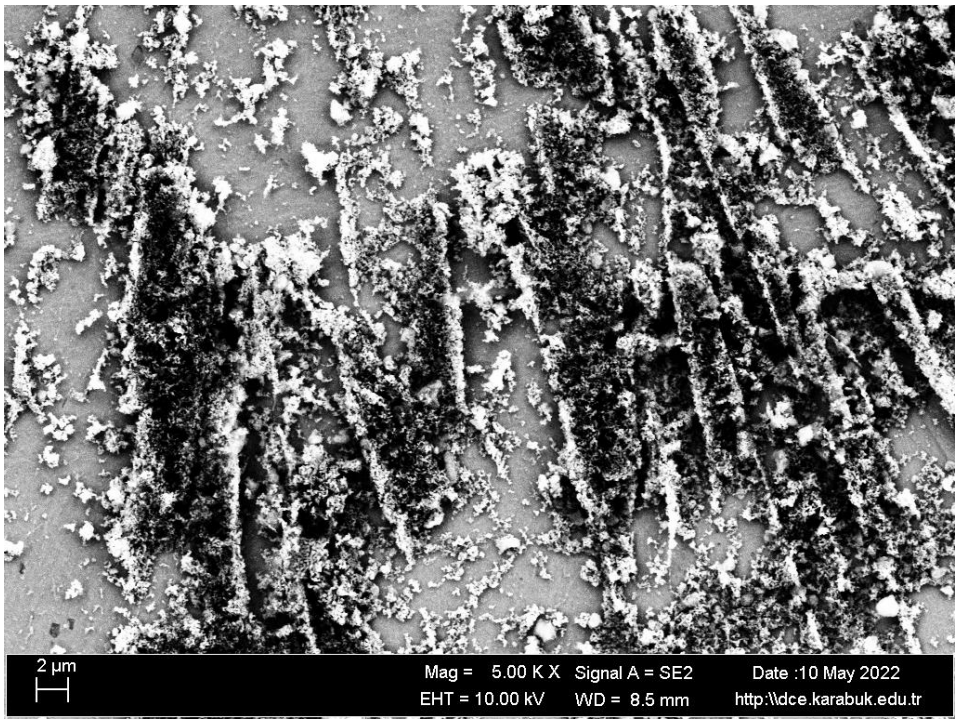
2 µm
Mag = 5.00 K X Signal A = SE2
Date :10 May 2022
EHT = 10.00 kV WD = 8.5 mm
http:\\dce.karabuk.edu.tr

(c)

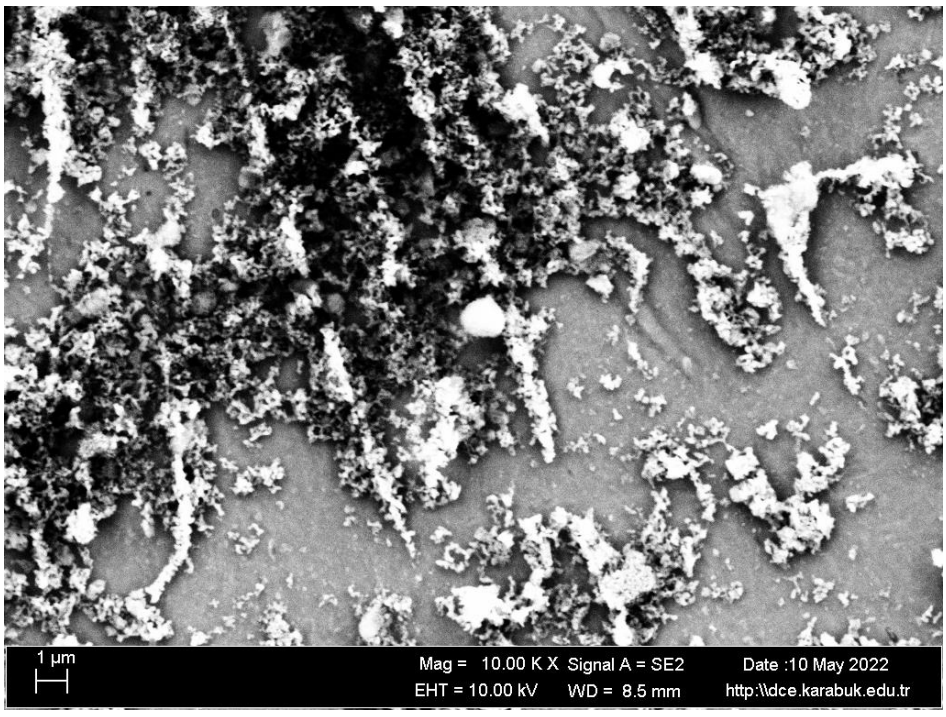
1 µm
Mag = 10.00 K X Signal A = SE2
Date :10 May 2022
EHT = 10.00 kV WD = 8.5 mm
http:\\dce.karabuk.edu.tr

(d)

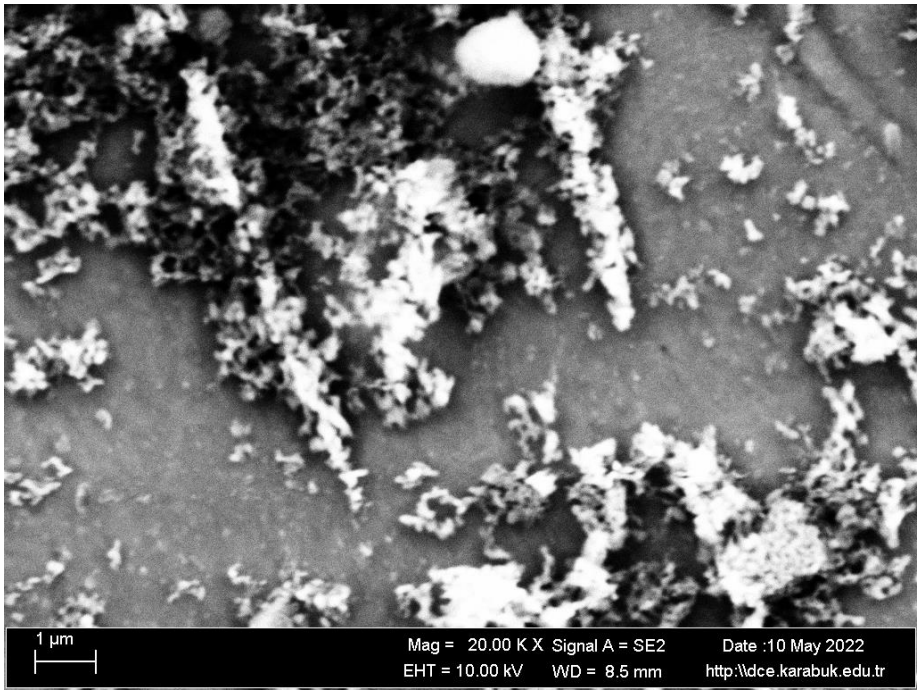


(e)

Figure 4.2. Images analysis results of the EDS Microstructure SEM of the SMA.

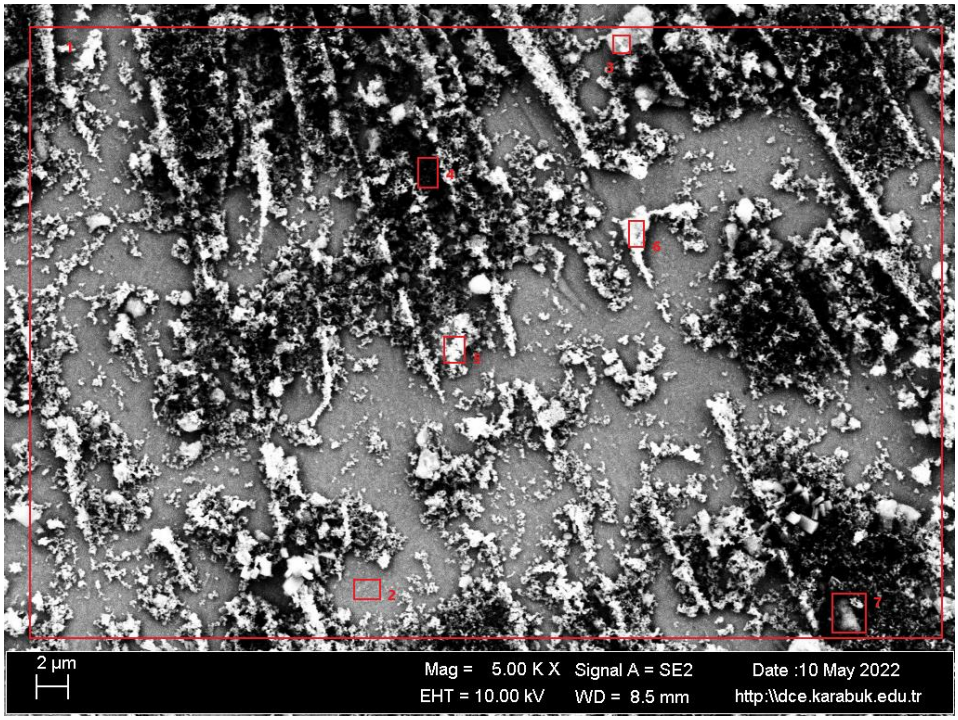


Figure 4.3. EDS analysis for the SMA.

Table 4.1. Response spectrum of the regions in Fig.4.3.

| **Wt.(%)** | | | | | | | | | | | |
|---|---|---|---|---|---|---|---|---|---|---|---|
| **Spectra** | H | O | Mg | Cl | C | Na | Ti | K | Ca | Cu | Ni |
| **1** | 0.03 | 48.57 | 0.39 | 0 | 2.15 | 0.33 | 20.92 | 0.13 | 0.04 | 0.09 | 27.35 |
| **2** | 0 | 3.83 | 0.08 | 0.07 | 0.02 | 0.28 | 39.38 | 0.16 | 0 | 0 | 56.17 |
| **3** | 0.09 | 48.99 | 0.69 | 0.09 | 9.3 | 0.7 | 11.27 | 0 | 0.07 | 0.87 | 27.94 |
| **4** | 0.12 | 61.92 | 0.35 | 0 | 1.69 | 0.31 | 17.37 | 0 | 0 | 0 | 18.24 |
| **5** | 0.01 | 44.5 | 0.12 | 0.19 | 3.03 | 0.25 | 20.45 | 0.01 | 0 | 0 | 31.44 |
| **6** | 0.02 | 41.71 | 0.32 | 0.04 | 3 | 0.49 | 22 | 0 | 0 | 0.28 | 32.14 |
| **7** | 0.05 | 59.33 | 0.39 | 0 | 5.49 | 0.36 | 15.24 | 0.01 | 0.08 | 0.24 | 18.81 |
| **Mean value:** | 0.04 | 44.12 | 0.33 | 0.06 | 3.53 | 0.39 | 20.95 | 0.05 | 0.03 | 0.21 | 30.3 |
| **Sigma:** | 0.04 | 19.24 | 0.2 | 0.07 | 3.03 | 0.16 | 8.95 | 0.07 | 0.04 | 0.32 | 12.69 |
| **Sigma means:** | 0.02 | 7.27 | 0.08 | 0.03 | 1.15 | 0.06 | 3.38 | 0.03 | 0.01 | 0.12 | 4.79 |

## 4.2. XRD ANALYSIS

X-ray diffraction (XRD) analysis is employed for phase identification in shape memory alloys (SMA). Figure 4.4 illustrates the presence of the NiTi austenite phase. The shape memory state in shape memory materials is determined by the occurrence of the martensitic transformation. Nitinol B2 maintains a stable austenite phase structure at room temperature. Morawiec et al. observed a minimal level of martensitic transformation in NiTi SHA following deformation caused by cold rolling. The presence of numerous dislocations and gaping defects in the atomic structure of this substance is responsible for this phenomenon. Furthermore, the microstructure results provided [72]demonstrated the presence of a twinned martensitic structure. This study observed the formation of austenite, martensite, and various phases including Ni4Ti3, Ni3Ti, NiTi, NiTi2, and Ti2Ni. Kuang et al. [74] detected similar phases in his study and this supports optical images.

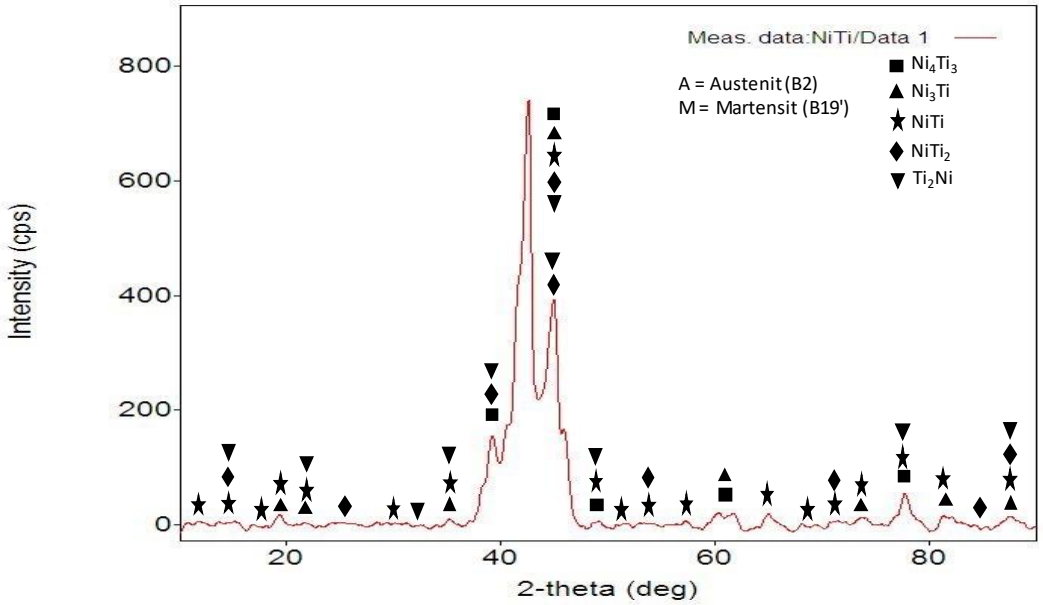


Figure 4.4. XRD analysis for SMA.

## 4.2. SEM-EDX TEST RESULTS

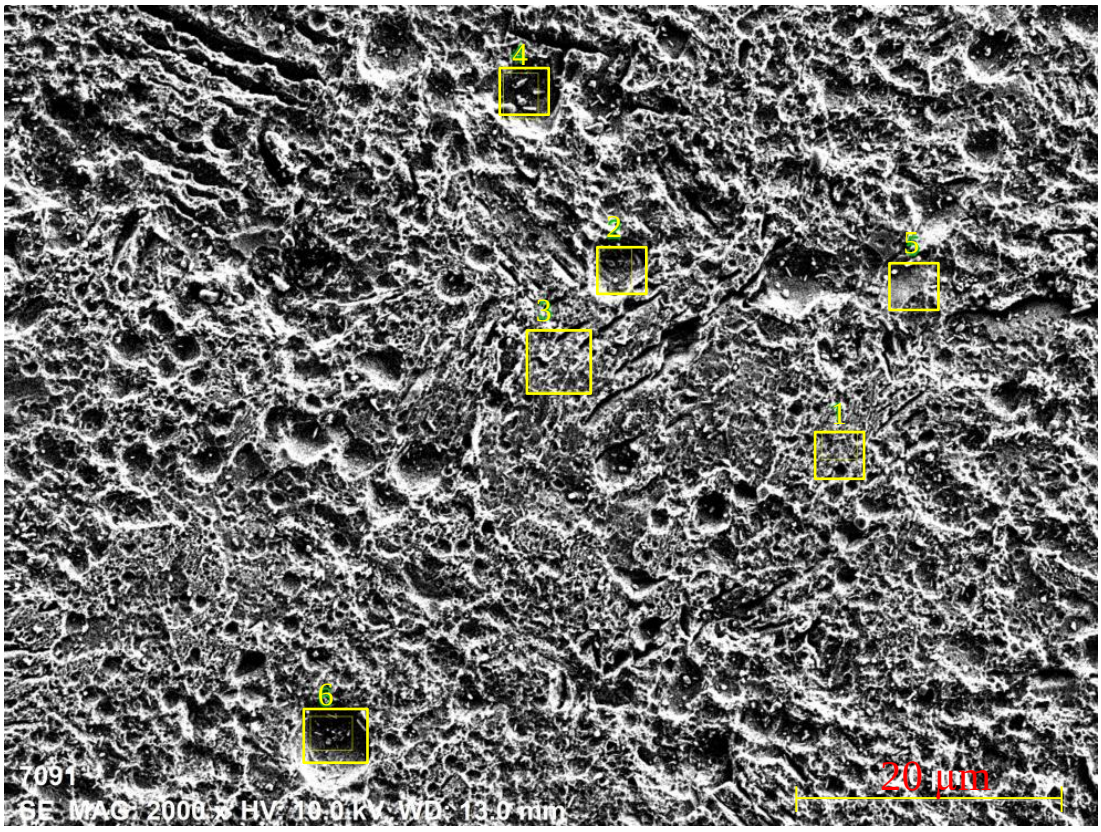


Figure 4.5. Ni-Ti SEM image with 2kx magnification.

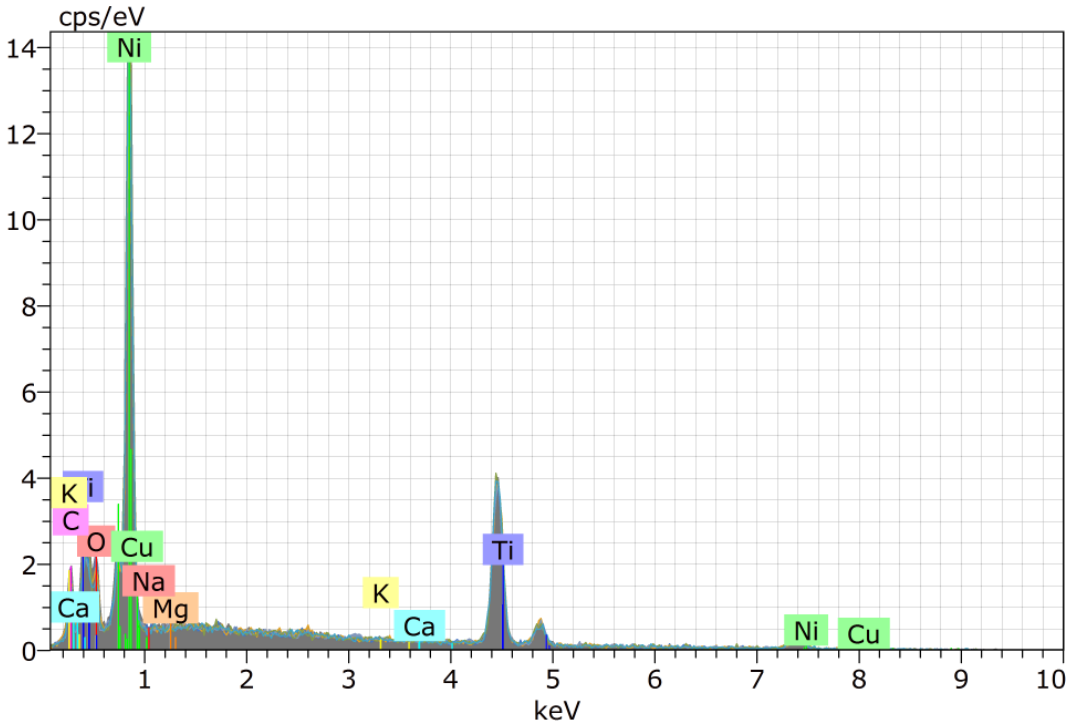


Figure 4.6. EDX response.

Table 4.2. 2kx magnification SEM and EDX images results wt. (%).

| Spectra | O | Cu | C | Na | K | Ni | Mg | Ca | Ti |
|---|---|---|---|---|---|---|---|---|---|
| **1** | 5.77 | 0.00 | 3.22 | 0.27 | 0.15 | 55.81 | 0.13 | 0.06 | 34.59 |
| **2** | 3.66 | 0.00 | 0.77 | 0.49 | 0.00 | 59.52 | 0.33 | 0.15 | 35.08 |
| **3** | 3.27 | 0.00 | 1.68 | 0.35 | 0.21 | 59.54 | 0.31 | 0.05 | 34.60 |
| **4** | 7.33 | 0.00 | 3.48 | 0.35 | 0.00 | 53.21 | 0.11 | 0.00 | 35.52 |
| **5** | 7.67 | 0.00 | 3.35 | 0.55 | 0.26 | 54.07 | 0.14 | 0.00 | 33.97 |
| **6** | 7.22 | 0.00 | 4.00 | 0.54 | 0.00 | 57.57 | 0.42 | 0.00 | 30.25 |
| **Mean value Sigma:** | 5.82 | 0.00 | 2.75 | 0.42 | 0.10 | 56.62 | 0.24 | 0.04 | 34.00 |
| **Sigma:** | 1.94 | 0.00 | 1.24 | 0.12 | 0.12 | 2.71 | 0.13 | 0.06 | 1.91 |
| **Sigma mean:** | 0.79 | 0.00 | 0.51 | 0.05 | 0.05 | 1.11 | 0.05 | 0.02 | 0.78 |

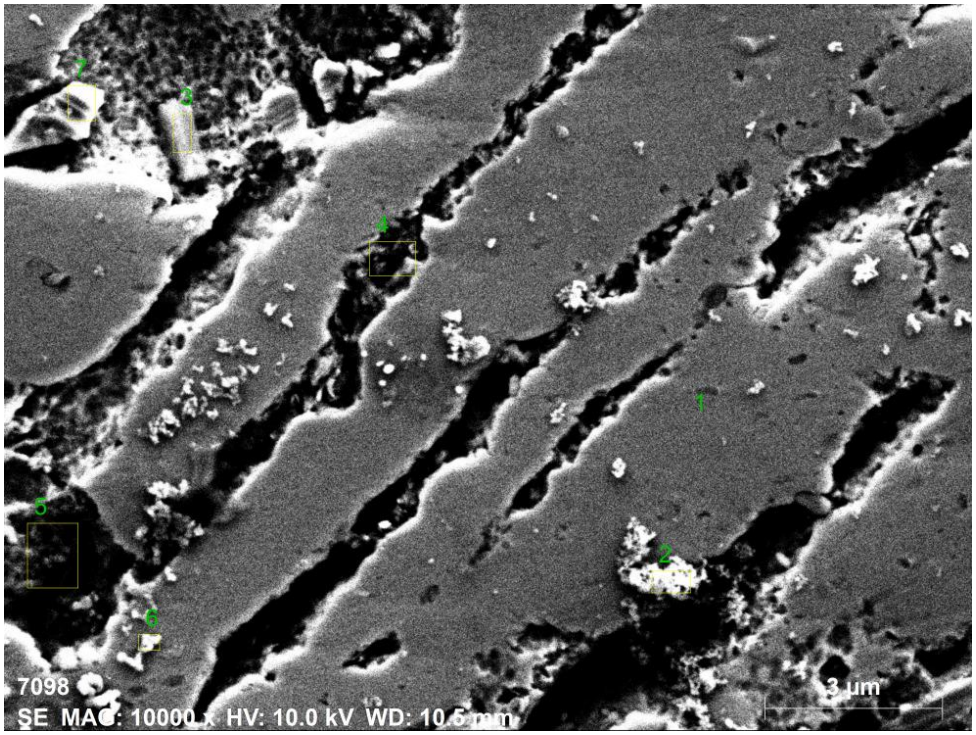


Figure 4.7. EDX sample image with 10kx magnification.

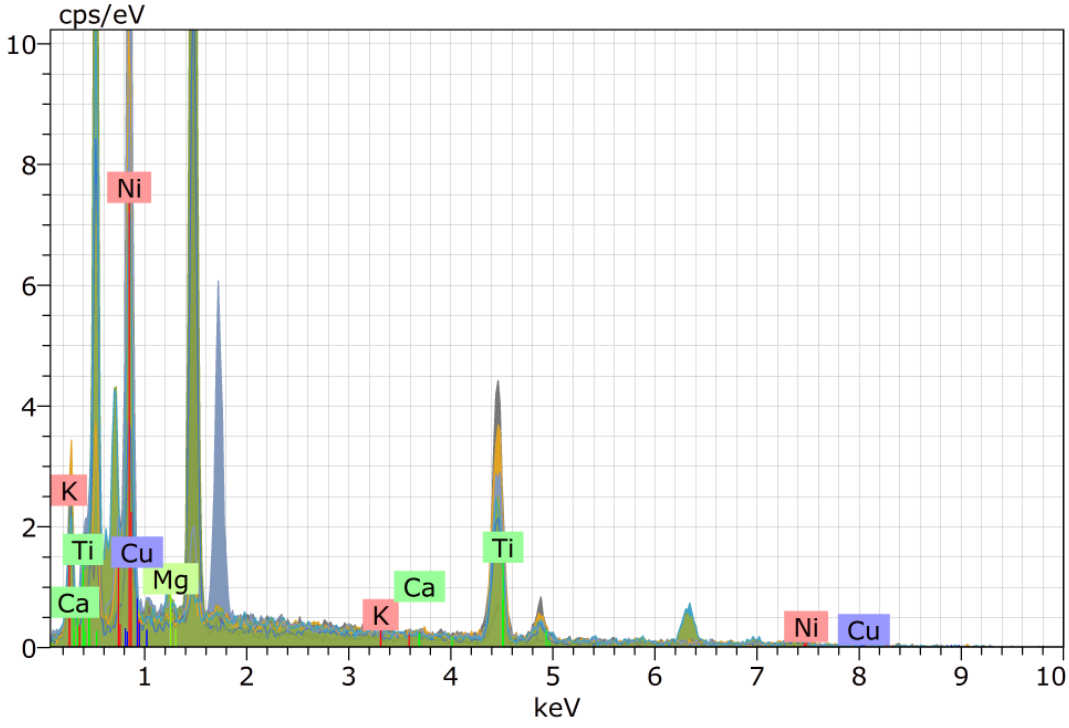


Figure 4.8. EDX response spectrum.

Table 4.3. Response spectra for the selected regions in Fig. 4.7. Wt. (%).

| Spectra | K | Ti | Mg | Cu | Ca | Ni |
|---|---|---|---|---|---|---|
| **1** | 0.00 | 38.58 | 2.64 | 0.00 | 0.34 | 58.44 |
| **2** | 0.00 | 31.06 | 4.53 | 7.62 | 0.22 | 56.56 |
| **3** | 0.05 | 34.01 | 1.20 | 0.00 | 0.48 | 64.25 |
| **4** | 0.07 | 43.46 | 0.21 | 0.00 | 0.57 | 55.69 |
| **5** | 0.07 | 53.01 | 0.58 | 0.74 | 0.46 | 45.14 |
| **6** | 0.00 | 39.34 | 0.33 | 0.00 | 0.00 | 60.33 |
| **7** | 0.12 | 39.32 | 2.33 | 0.00 | 0.19 | 58.04 |
| **Mean value:** | 0.05 | 39.83 | 1.69 | 1.19 | 0.32 | 56.92 |
| **Sigma:** | 0.05 | 7.07 | 1.58 | 2.85 | 0.20 | 5.91 |
| **Sigma mean:** | 0.02 | 2.67 | 0.60 | 1.08 | 0.08 | 2.23 |

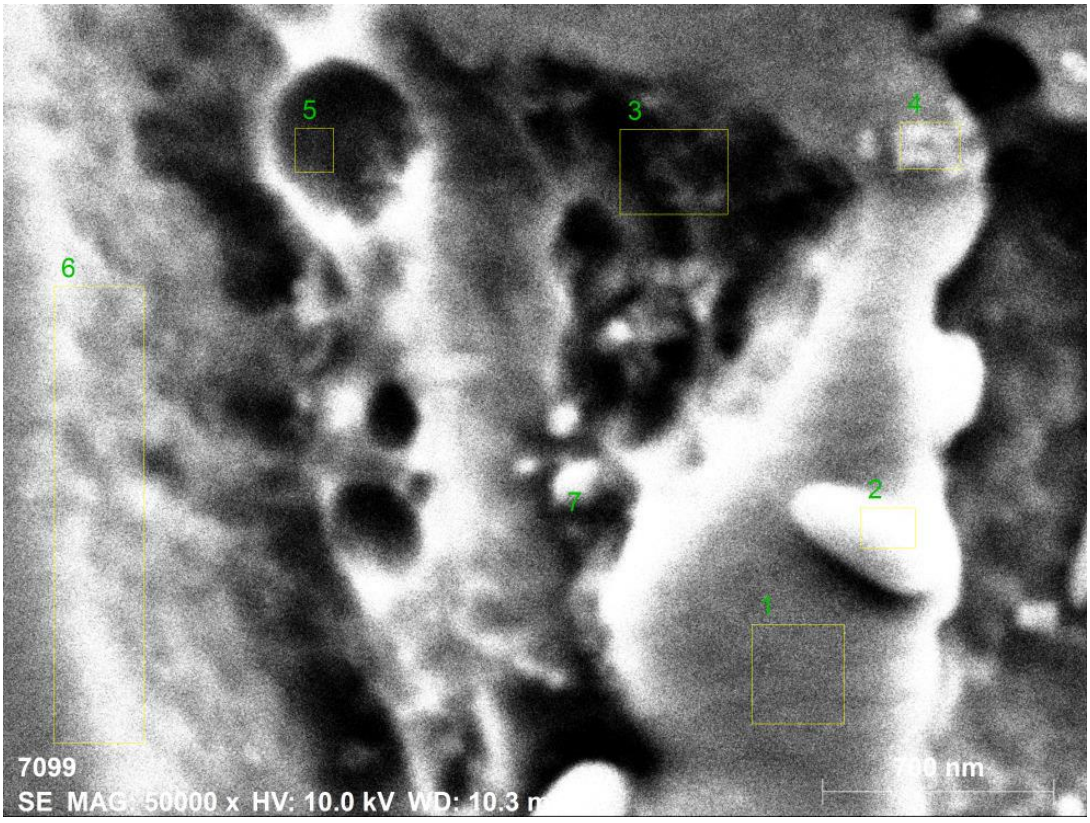


Figure 4.9. 50kx magnification sem image.

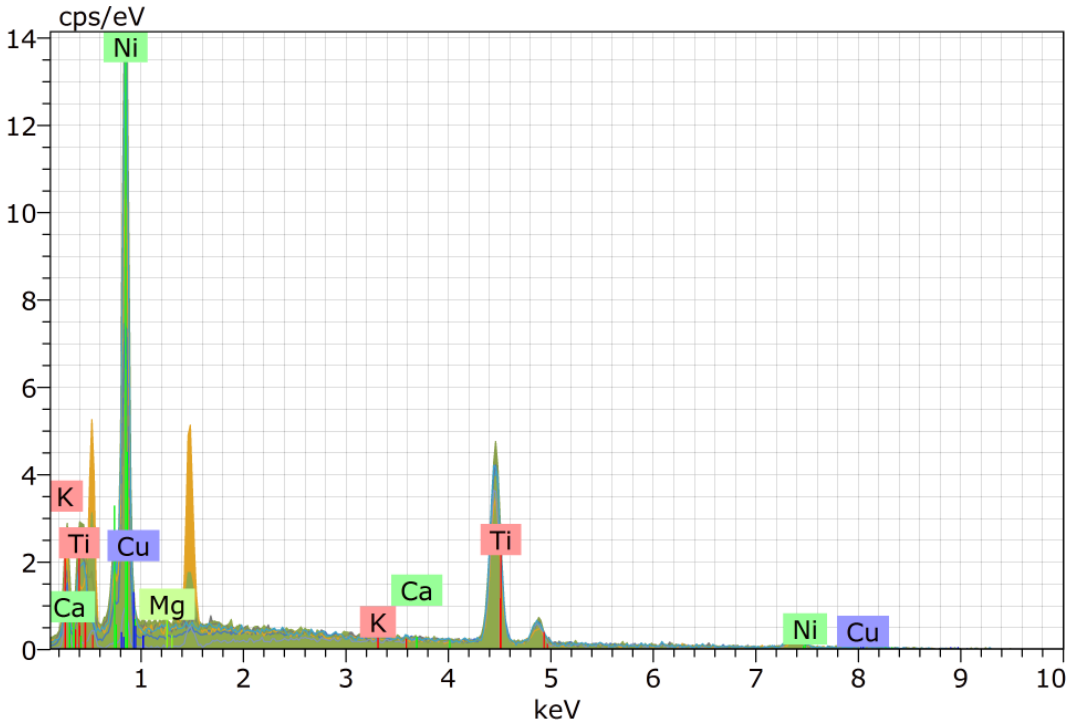


Figure 4.10. Edx response spectrum.

Table 4.4. Elemental response of the selected regions in Fig. 4.9. Mass Percent (%).

| Spectrum | Cu | Ti | Ca | Mg | Ni | K |
|---|---|---|---|---|---|---|
| **1** | 0.00 | 39.99 | 0.00 | 0.25 | 59.76 | 0.00 |
| **2** | 0.00 | 38.41 | 0.19 | 0.53 | 60.87 | 0.00 |
| **3** | 0.00 | 88.17 | 1.93 | 0.00 | 9.36 | 0.54 |
| **4** | 0.00 | 40.22 | 0.00 | 0.35 | 59.43 | 0.00 |
| **5** | 0.00 | 52.72 | 0.44 | 0.00 | 46.46 | 0.38 |
| **6** | 0.00 | 38.67 | 0.04 | 0.19 | 60.84 | 0.26 |
| **7** | 0.00 | 35.20 | 0.18 | 0.50 | 63.99 | 0.12 |
| **Mean value:** | 0.00 | 47.63 | 0.40 | 0.26 | 51.53 | 0.19 |
| **Sigma:** | 0.00 | 18.72 | 0.69 | 0.21 | 19.42 | 0.21 |
| **Sigma mean:** | 0.00 | 0.08 | 0.26 | 0.08 | 7.34 | 0.00 |

## 4.3. IMMERSION CORROSION TESTS RESULTS

Figure 4.11 illustrates the relationship between Weight Lost (mg/dm2) and Time (Day) for the NiTi Alloy under investigation. Figure 6 shows that there was minimal mass loss during the first two days, followed by a linear decrease in mass. On the eighth working day during the immersion test duration, a passive film forms on the surface of the investigated alloy, resulting in a consistent mass loss.

Table 4.5. Immersion Corrosion Test Day- Weight Loss (mg/dm2).

| Time (Day) | Weight Lost (mg/dm$^2$) |
|---|---|
| **0** | 0 |
| **1** | 0.002 |
| **2** | 0.02 |
| **3** | 26.36 |
| **4** | 26.36 |
| **5** | 30.13 |
| **6** | 41.43 |
| **7** | 41.43 |
| **10** | 39.89 |

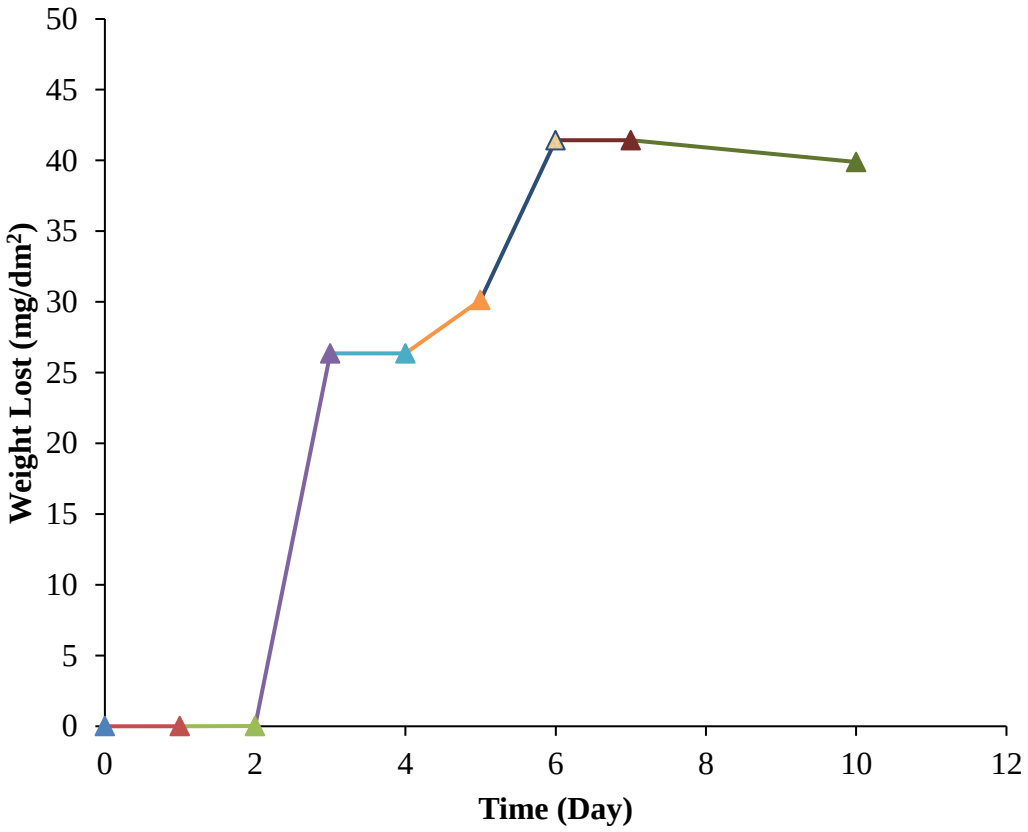


Figure 4.11. The relationship between time (day) and weight loss (mg/dm2) in the examined NiTi alloy.

SEM images and EDS analysis results of the shape memory alloy are given in Figure 4.5. When the SEM image of the examined alloy is examined in Figure 4.5, a clean, tight and dense image is seen. Surface quality is very important for shape memory materials because it directly affects the formation of a passive structure. Matthews et

al. studied the relationship between corrosion resistance and porosity [90]. A porous structure is characterized as a defect in the structure and this is because many porous structures can form on the metal surface when the natural weak bonds are pulled on the metal surface. It is very difficult to form a passive film on the surface of a porous material. On a clean surface, it is possible to form a continuous and smooth passive film, and in this study, such a surface appears, in line with good corrosion behavior. This oxide layer provided very good protection for the alloy under study and improved corrosion resistance. In general, when the EXD results are analyzed, it is seen that oxygen and titanium are high. Therefore, it is thought that TiO2 is formed and that the CO2 layer in the regions numbered 2.7 and the amount of Cu in the regions numbered 3.4 indicate the formation of precipitate.

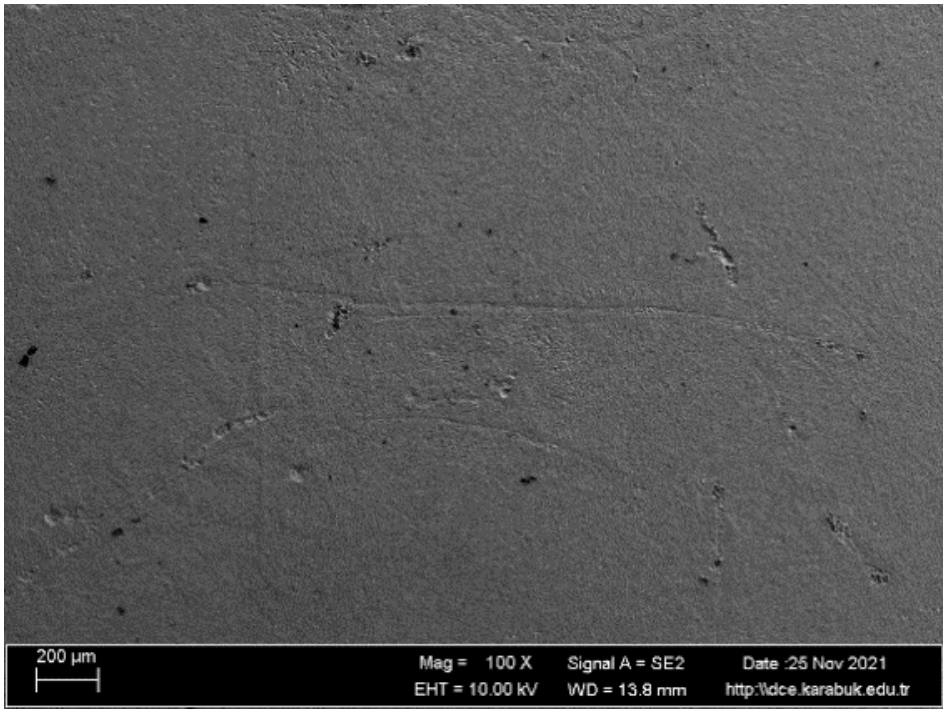


(a)


(b)

Figure 4.12. 500 X SEM images of SMA after corrosion test.

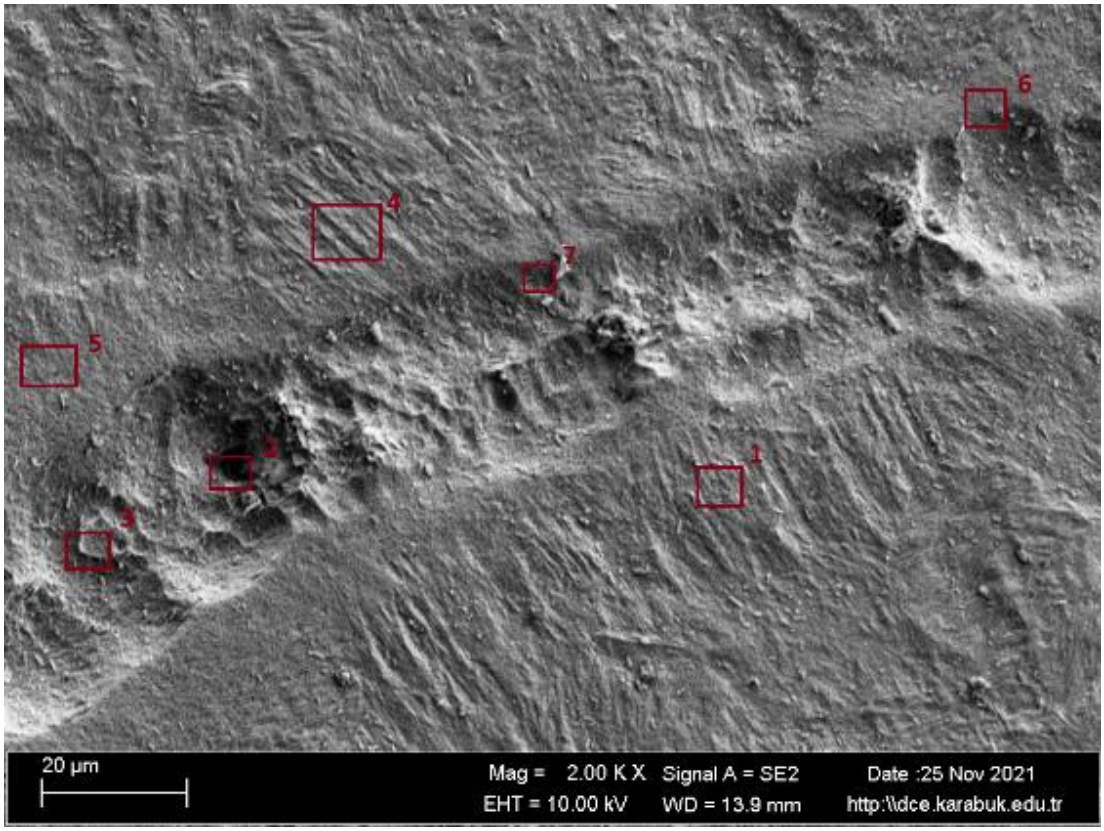


Figure 4.13. SEM images and EDS analysis of the shape memory alloy after corrosion test.

Table 4.6. Elemental response from the selected regions in Fig.4.13.

| **Wt. (%)** | | | | | | | | | |
|---|---|---|---|---|---|---|---|---|---|
| **Spectrum** | O | Cu | C | Mg | Na | Ca | K | Ni | Ti |
| **1** | 25.53 | 0.00 | 5.04 | 1.58 | 2.12 | 0.00 | 0.29 | 13.20 | 52.24 |
| **2** | 11.19 | 0.27 | 63.40 | 0.25 | 0.56 | 0.01 | 0.11 | 4.80 | 19.42 |
| **3** | 28.33 | 1.11 | 5.51 | 1.66 | 2.92 | 0.74 | 0.40 | 12.86 | 46.48 |
| **4** | 30.04 | 1.26 | 4.04 | 1.44 | 2.50 | 0.05 | 0.00 | 10.42 | 50.26 |
| **5** | 27.40 | 0.00 | 2.30 | 2.50 | 2.80 | 0.12 | 0.00 | 13.64 | 51.24 |
| **6** | 25.09 | 0.35 | 5.54 | 0.73 | 1.85 | 0.82 | 0.21 | 13.45 | 51.96 |
| **7** | 26.93 | 0.00 | 11.74 | 0.30 | 1.26 | 1.11 | 0.20 | 10.01 | 48.46 |
| **Mean value:** | 24.93 | 0.43 | 13.94 | 1.21 | 2.00 | 0.41 | 0.17 | 11.20 | 45.72 |
| **Sigma:** | 6.29 | 0.54 | 22.01 | 0.82 | 0.86 | 0.47 | 0.15 | 3.18 | 11.78 |
| **Sigma means:** | 2.38 | 0.20 | 8.62 | 0.31 | 0.32 | 0.18 | 0.06 | 1.20 | 4.45 |

## 4.4. POTENTIODYNAMIC CORROSION TESTS RESULTS

Figure 4.14 displays the potentiodynamic curves acquired in Hank's solution for the examined Ni-Ti shape memory alloy. NiTi exhibits a significant presence of passivation. Furthermore, the observed rise in current density in the alloy of NiTi at

elevated potentials is believed to be caused by the generation of oxygen resulting from the oxidization of water. NiTi exhibits favorable corrosion resistance. The presence of a titanium oxide film is believed to be responsible for the observed protective effect. Authors [75]–[77] have reported these results, indicating an ability for creation of a passive film consistent with previously reported data.

Table 4.7. Potentiodynamic Corrosion Test Results according to the relationship of Time (Day)- Icorr (A/cm2) (10-9).

| **Time (Day)** | **Icorr ($A/cm^2$) ($10^{-9}$)** |
|---|---|
| **0,00001** | 471.7 |
| **1** | 132.33 |
| **2** | 47.03 |
| **6** | 135.67 |
| **9** | 298 |
| **12** | 364.67 |
| **15** | 499.33 |
| **18** | 372 |
| **23** | 273.33 |

Table 4.8. Potentiodynamic Corrosion Test Results according to Time (Day)-Chord (mV) relationship.

| **Time (Day)** | **0.00001** | **1** | **2** | **6** | **9** | **12** | **15** | **18** | **23** |
|---|---|---|---|---|---|---|---|---|---|
| **Ecorr(mV)** | -237 | -51 | -109 | -114 | -78.4 | -76.1 | -106 | 18.6 | -73 |

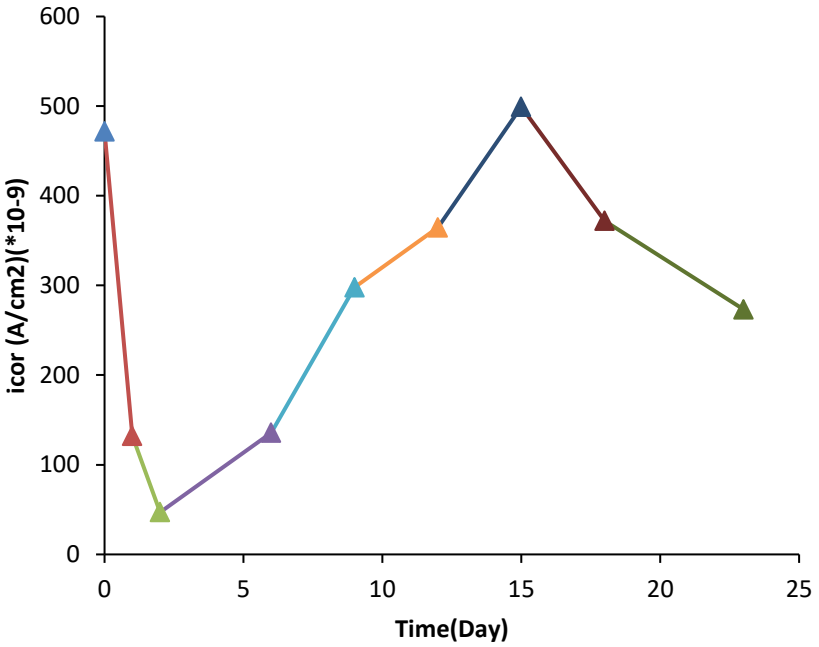


(a)

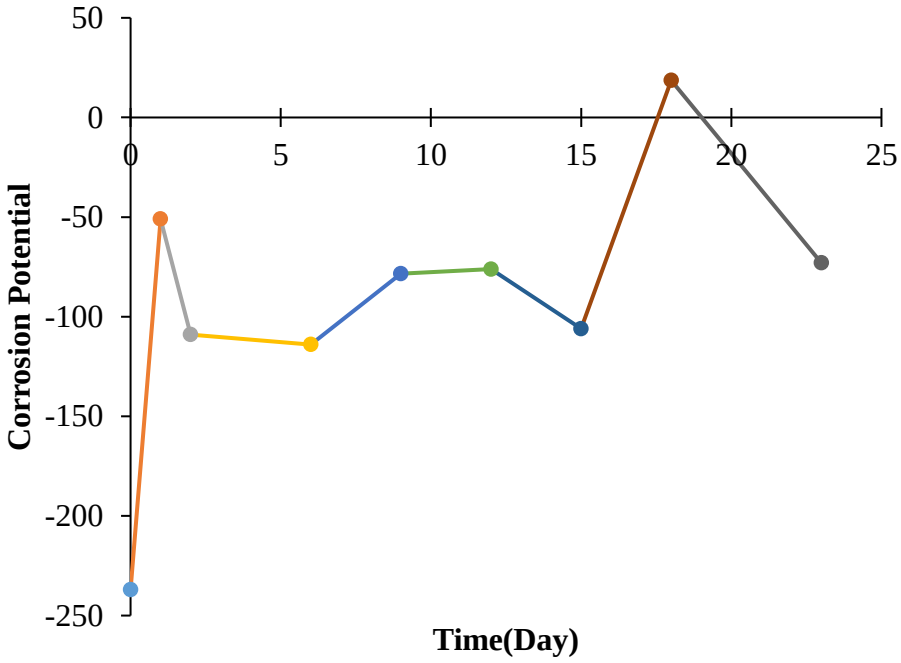


(b)

Figure 4.14. Changes of (a) current density of corrosion (icor); (b) corrosion potential.

Figure 4.15 displays the SMA under examination, presenting the Tafel curves derived from potential dynamic polarization examinations conducted at specific intervals in the synthetic body fluid of the alloy. Both the corrosion electrical current density

(İcorr) and corrosion potential (Ecorr) were calculated by extrapolating the intersection point in anodic and cathodic polarization. The temporal variations of these parameters are presented in Figure 4.15. Figure 4.15 illustrates the periodic variation of the corrosion current density, ranging from 450x10-9 A/cm2 to 50x10-9 A/cm2. The average corrosion current density of the investigated SMA sample is 280x10-9 A/cm2. Additionally, the corrosion potential transitions from an active state to a noble state, indicating a gradual increase in resistance to corrosion in the solution over time.

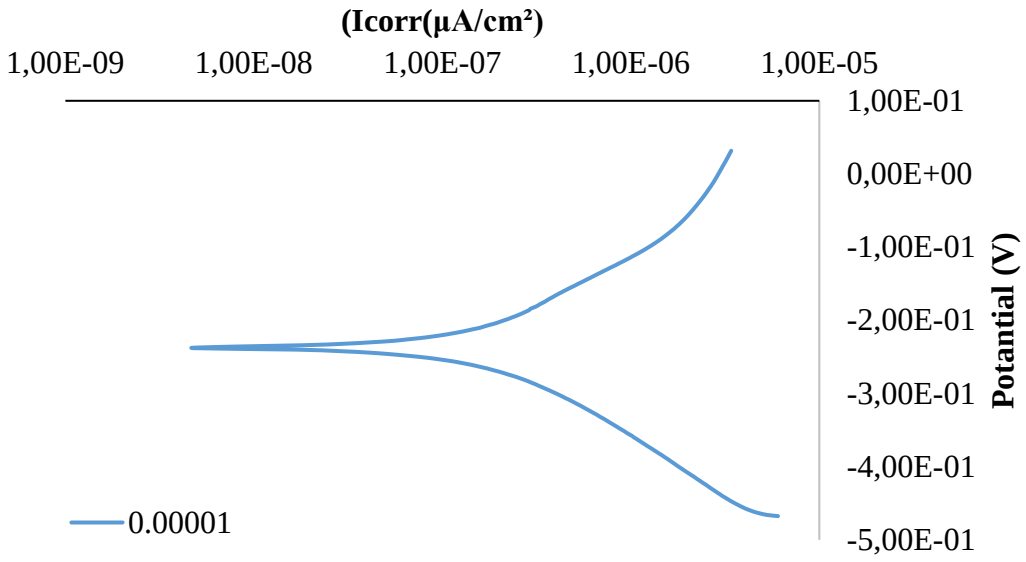


(a)

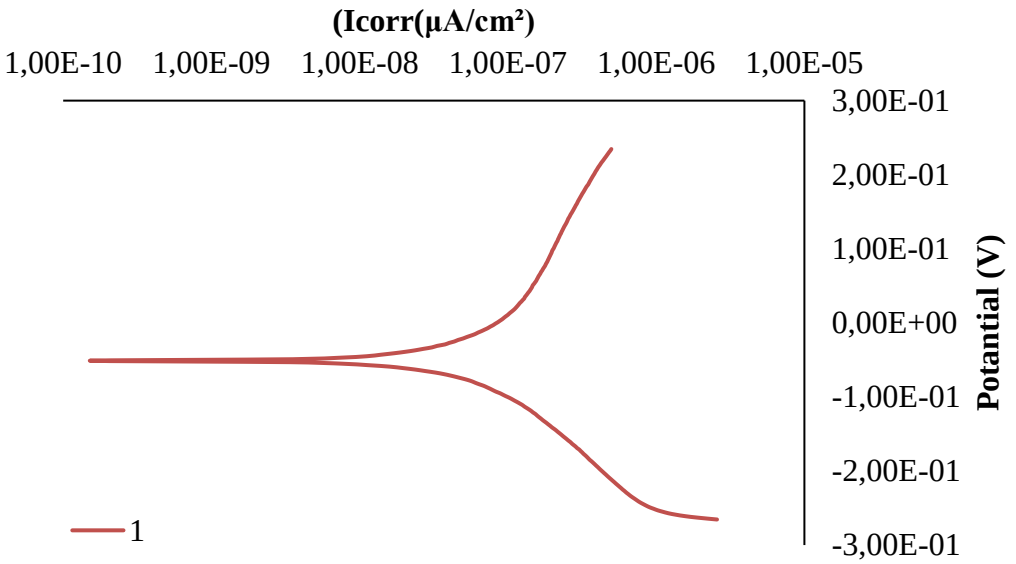


(b)

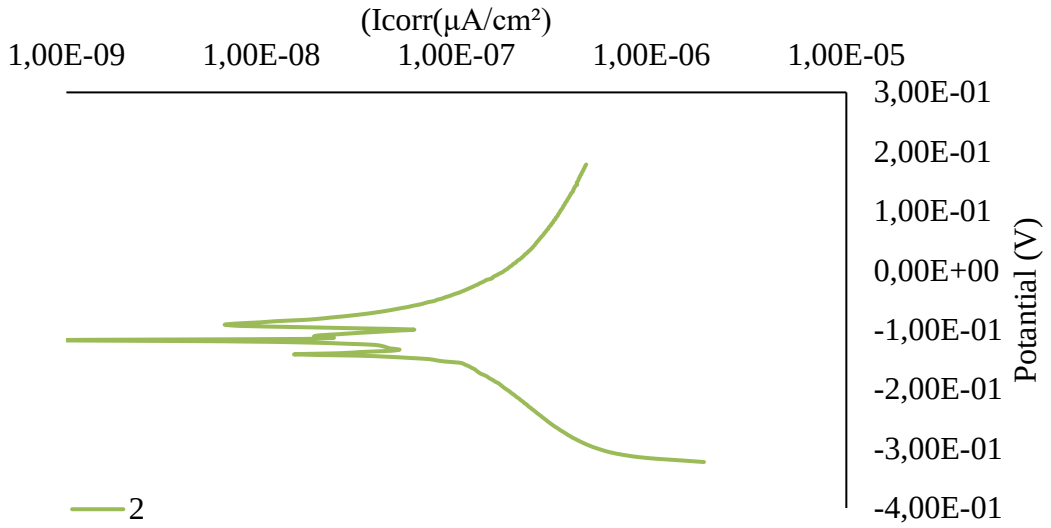
(Icorr(µA/cm²)
1,00E-09
1,00E-08
1,00E-07
1,00E-06
1,00E-05
3,00E-01
2,00E-01
1,00E-01
0,00E+00
-1,00E-01
-2,00E-01
-3,00E-01
-4,00E-01
Potantial (V)
2

(c)

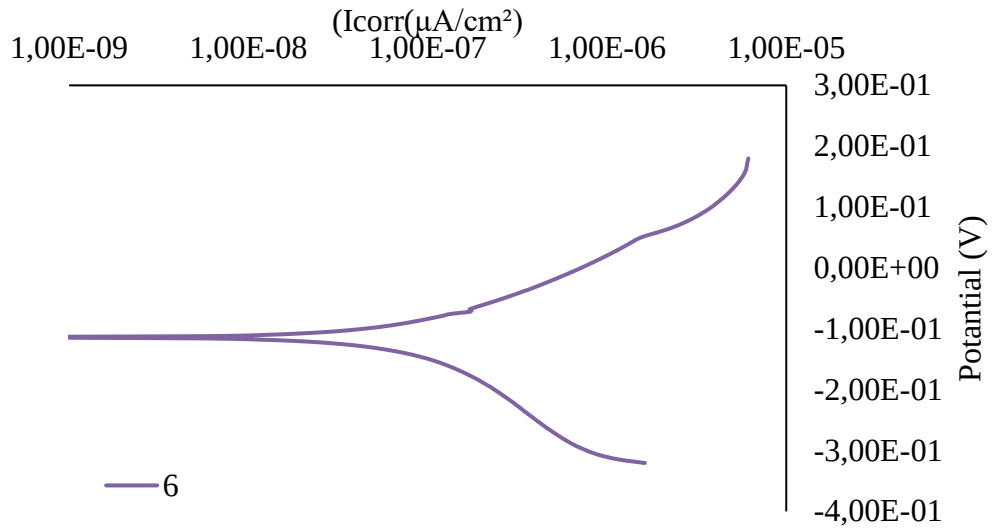
(Icorr(µA/cm²)
1,00E-09
1,00E-08
1,00E-07
1,00E-06
1,00E-05
3,00E-01
2,00E-01
1,00E-01
0,00E+00
-1,00E-01
-2,00E-01
-3,00E-01
-4,00E-01
Potantial (V)
6

(d)

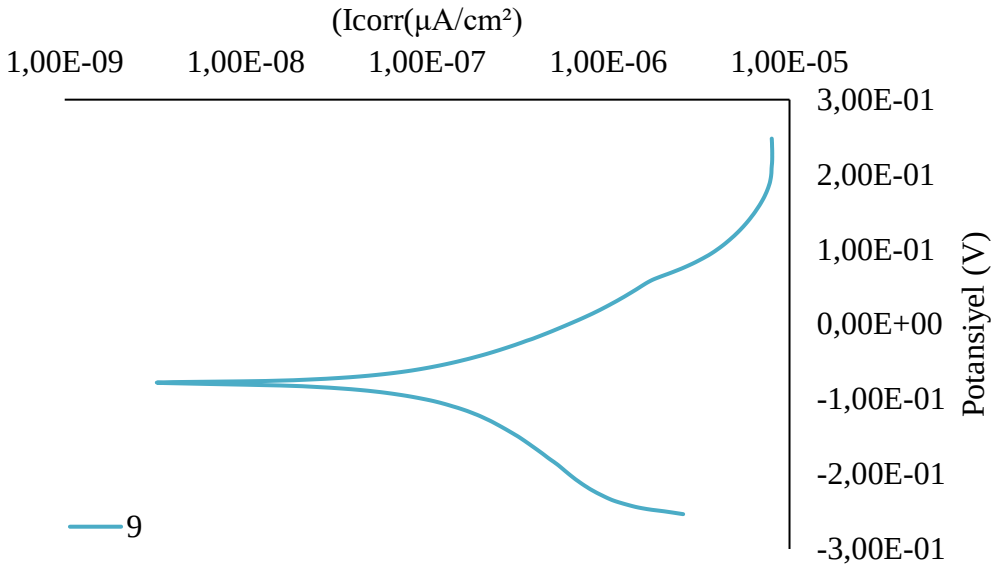
(Icorr(µA/cm²)
1,00E-09
1,00E-08
1,00E-07
1,00E-06
1,00E-05
3,00E-01
2,00E-01
1,00E-01
0,00E+00
-1,00E-01
-2,00E-01
-3,00E-01
Potansiyel (V)
9

(e)

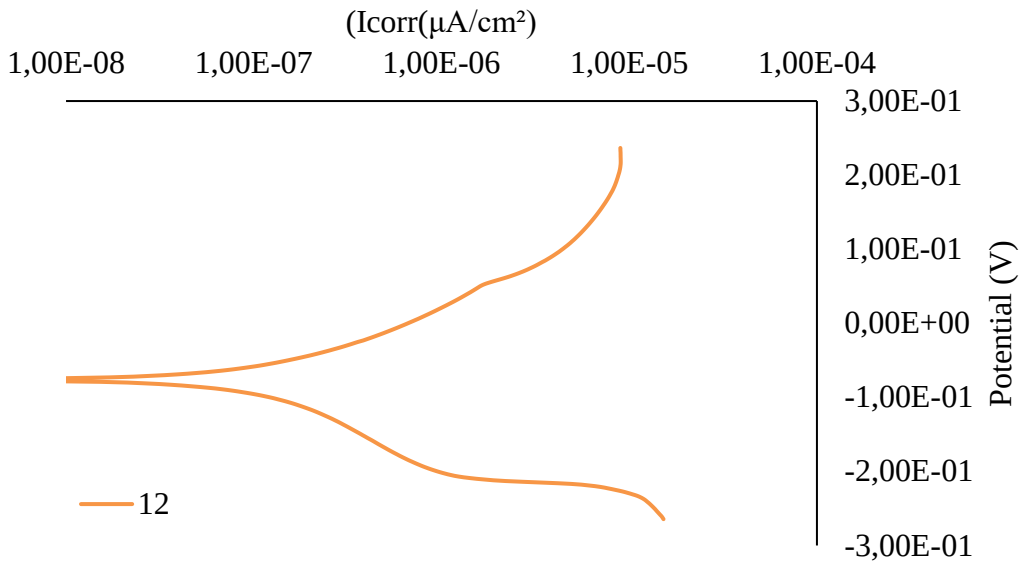
(Icorr(µA/cm²)
1,00E-08
1,00E-07
1,00E-06
1,00E-05
1,00E-04
3,00E-01
2,00E-01
1,00E-01
0,00E+00
-1,00E-01
-2,00E-01
-3,00E-01
Potential (V)
12

(f)

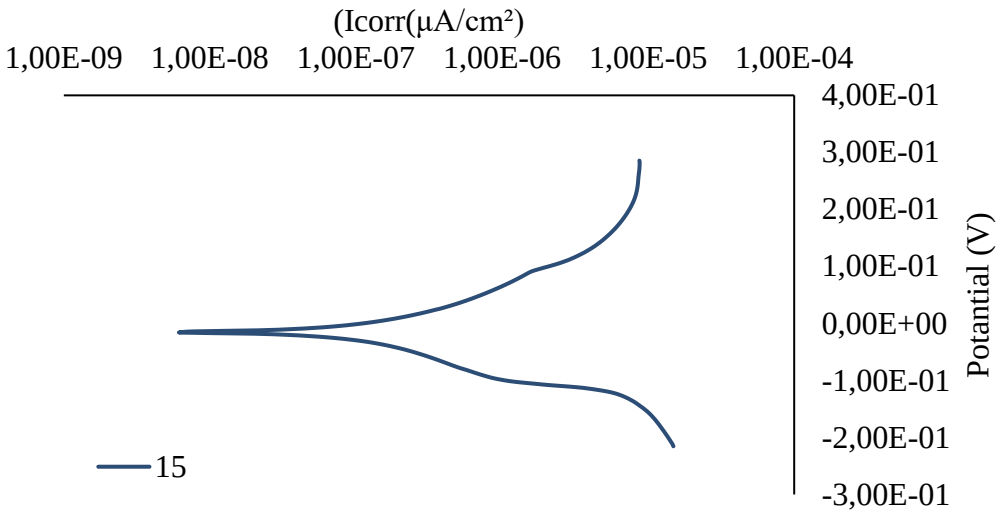
(Icorr(µA/cm²)
1,00E-09
1,00E-08
1,00E-07
1,00E-06
1,00E-05
1,00E-04
4,00E-01
3,00E-01
2,00E-01
1,00E-01
0,00E+00
-1,00E-01
-2,00E-01
-3,00E-01
Potantial (V)
15

(g)

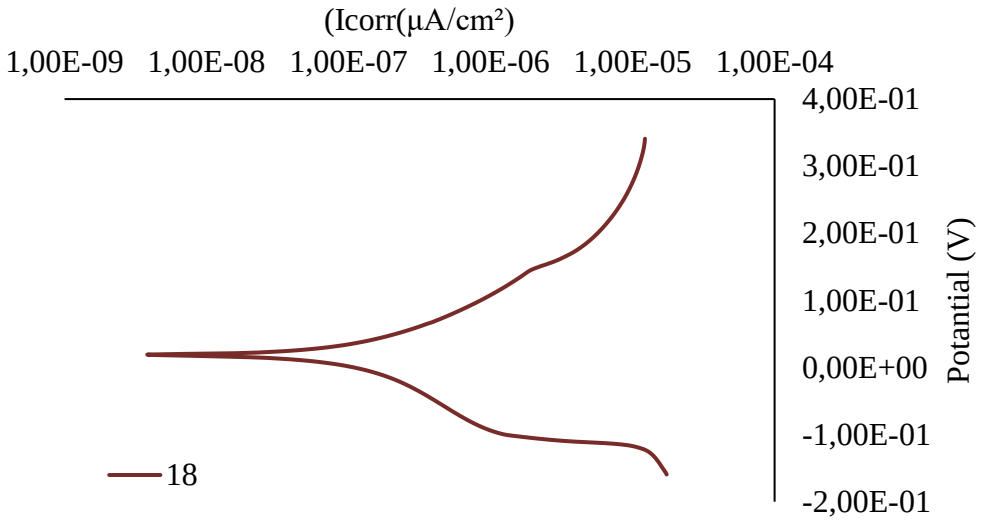
(Icorr(µA/cm²)
1,00E-09
1,00E-08
1,00E-07
1,00E-06
1,00E-05
1,00E-04
4,00E-01
3,00E-01
2,00E-01
1,00E-01
0,00E+00
-1,00E-01
-2,00E-01
Potantial (V)
18

(ğ)

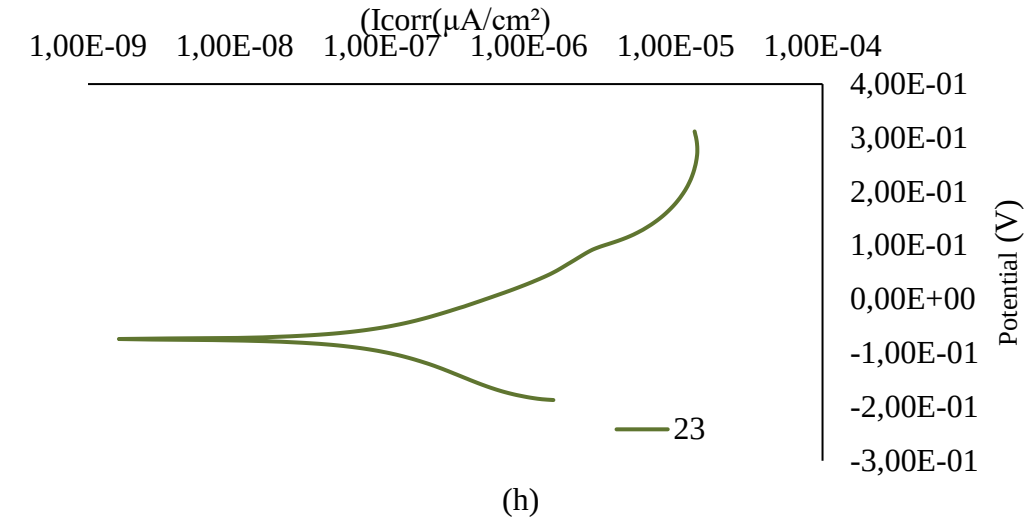


(h)

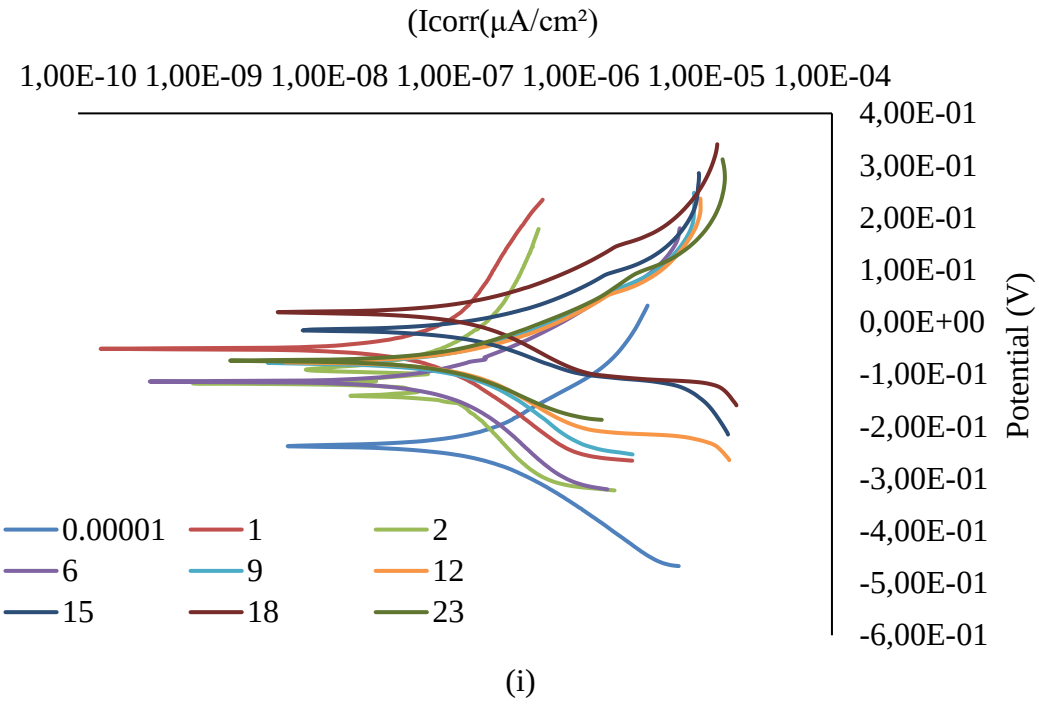


(i)

Figure 4.15. The Taffel curves of the alloy measured in artificial body fluid over a period of 23 days at room temperature.

Corrosion rate values, which indicate the reduction in thickness in millimeters per year, were determined in accordance with Faraday's rules. These values were calculated employing the corrosion current density as well as loss of weight data, as shown in Figure 4.8. Figure 4.8 displays the Icorr-time graph, which exhibits a recurring fluctuation in the thickness reduction over time, as determined through the potentiodynamic polarization information. The range of this variation is between 0.008 and 0.0008. The calculated thickness changes derived using the immersion tests

exhibited a gradual decrease over time. The mean potentiodynamic test thickness-decrease value was 0.005 mm/year, while the smallest immersion test thickness-decrease value was 0.03 mm/year.

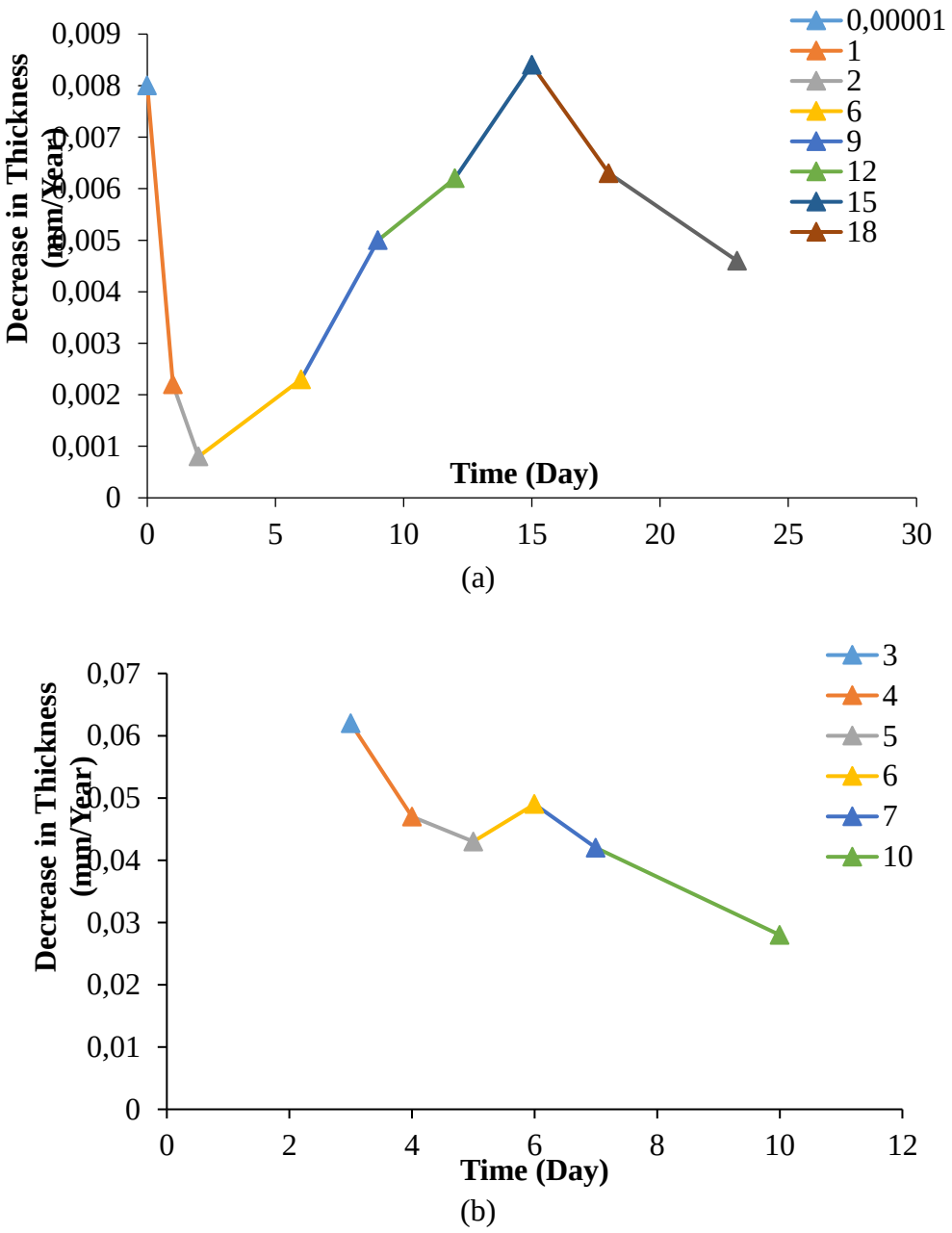


Figure 4.16. The graph (a): illustrates the rate of thickness reduction over time, measured in millimeters per year, following two different tests: b) potentiodynamic and immersion.

Cisse al.[78] applied a chemical passivation coating on NiTi, but the corrosion rate (0.11 × 10−3 mm/year) observed in their study was higher than the corrosion rate

observed in our study for the NiTi sample. In a study conducted by E. Balcı et al., the mean corrosion rate of NiTiNbV the quaternary shape memory alloys (SCAs) was determined to be approximately 1.70 x 10-2 mpy. This corrosion rate was found to be higher than the corrosion rate observed in the present study.

The resistance to corrosion in the potentiodynamic and immersion tests conducted using synthetic body fluid at room temperature was found to be superior compared to previous studies.

Figure 4.17 presents scanning electron microscope (SEM) images and energy-dispersive X-ray spectroscopy (EDS) analysis outcomes of the shape memory alloy (SMA). The investigated alloy in Figure 4.17 exhibits a low number of pits on its corroded surface. Additionally, the size of these pits is too small to be apparent even at high magnifications. Furthermore, the passive films that develop on the corroded surface exhibit compatibility with the edx findings. Edx analysis reveals a general abundance of oxygen and titanium. The formation of TiO2 and CO2 piles is believed to occur as a result of this phenomenon.

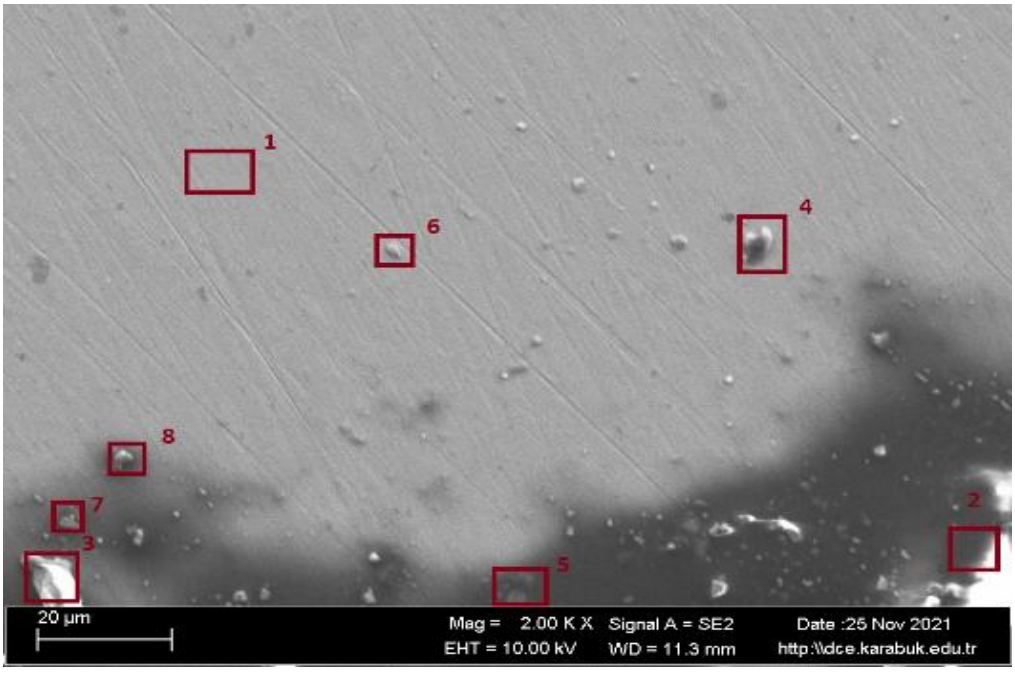


Figure 4.17. 2kX SEM image of corroded surface.

Table 4.9. The response spectrum from the regions in Fig. 4.17.

| **Wt. (%)** | | | | | |
|---|---|---|---|---|---|
| **Spectra** | C | Ti | Ni | Cu | O |
| **1** | 13.78 | 41.61 | 9.71 | 0.00 | 34.90 |
| **2** | 82.10 | 0.86 | 0.00 | 0.00 | 17.06 |
| **3** | 78.67 | 0.66 | 0.00 | 0.16 | 20.51 |
| **4** | 44.29 | 23.97 | 5,44 | 0.00 | 26.30 |
| **5** | 49.01 | 28.28 | 7.04 | 0.00 | 15.68 |
| **6** | 74.36 | 5.43 | 0.34 | 0.02 | 19.85 |
| **7** | 60.28 | 7.99 | 1.08 | 0.03 | 30.62 |
| **Mean value:** | 57.50 | 15.54 | 3.37 | 0.03 | 23.56 |
| **Sigma:** | 24.16 | 15.86 | 3.98 | 0.06 | 7.23 |
| **Sigma mean:** | 9.13 | 6.00 | 1.50 | 0.02 | 2.73 |

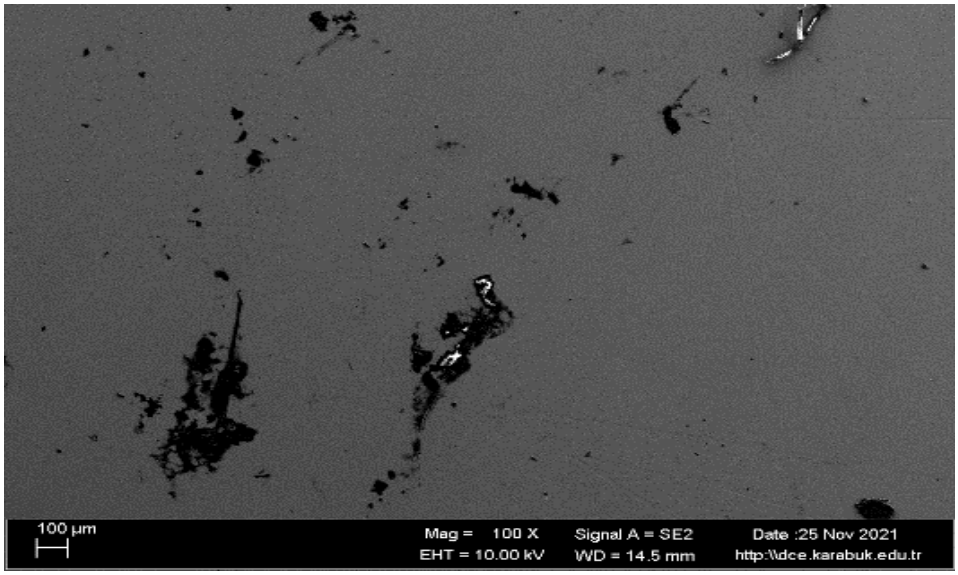


(a)

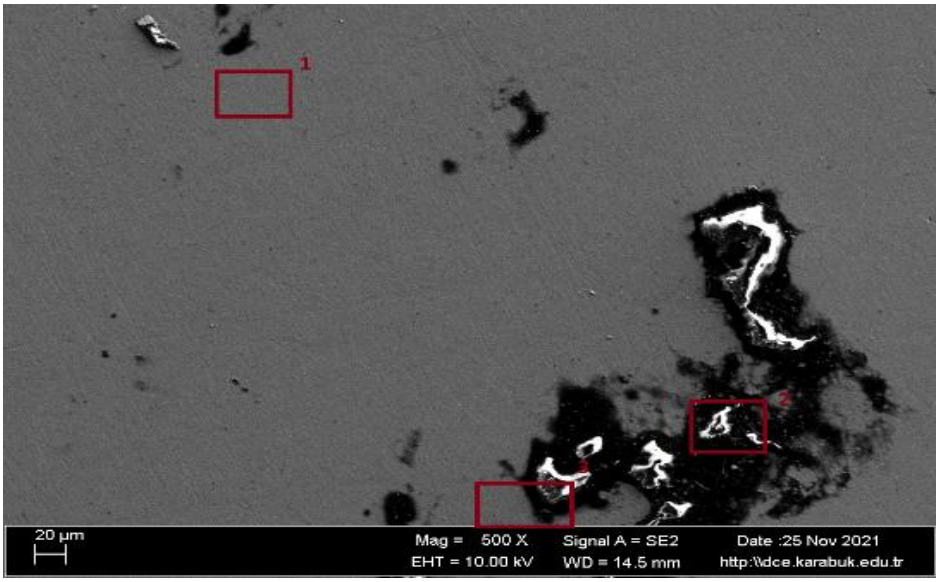


(b)

Figure 4.18. (a) SEM and (b) EDS results of SMA after corrosion.

Table 4.10. Elemental response spectrum from the selected Region in Fig. 4.18.

| **Wt. (%)** | | | | | |
|---|---|---|---|---|---|
| **Spectra** | Cu | C | Ti | O | Ni |
| **1** | 0.05 | 15.15 | 41.95 | 33.98 | 8.85 |
| **2** | 0.14 | 68.23 | 3.96 | 27.63 | 0.04 |
| **3** | 0.00 | 72.71 | 0.01 | 27.28 | 0.00 |
| **Mean value:** | 0.07 | 52.03 | 15.31 | 29.63 | 2.96 |
| **Sigma:** | 0.07 | 32.02 | 23.16 | 3.77 | 5.09 |
| **Sigma mean:** | 0.04 | 18.48 | 13.37 | 2.18 | 2.94 |

## 4.5. WEAR TEST RESULTS

Table 4.11 presents the wear test outcomes of the Ni-Ti SMA, analyzed under varying loads, both in dry conditions and in the presence of body fluid. Table 4.9 presents weight loss results, which allow for the identification and categorization of two separate types of SMAs described in the literature, based on different phases. The wear resistance in β-phase TiNi materials correlates positively with the corresponding hardness values of the respective alloys. The hardness of these alloys increases with the amount of nickel present, and this increase is partially compatible with the B2 matrix of both the β-phase (2) and the β-phase (3). This compatibility is attributed to the existence of Ti3Ni4 precipitates [79]. The wear test results are influenced by both the interaction with the surface and the material's energy absorption capacity. The alloy under investigation exhibits an excellent transformation capacity due to its phase transforming temperature being in close proximity to the test temperature. Consequently, it absorbs a greater amount of energy to restore the structure and effectively inhibits various factors.

Table 4.11. Abrasion test results of Ni-Ti SMA in dry environment and in body fluid.

| **Load (N)** | **Mass Loss (g)** | |
|---|---|---|
| | Body Liquid Wear Test | Dry Wear Test |
| **20** | 0.0075 | 0.0059 |
| **40** | 0.01739 | 0.0211 |

Figure 4.19 presents the wear test findings for Ni-Ti SMA under two different conditions: under dry conditions and in the presence of body fluid, while applying a load.

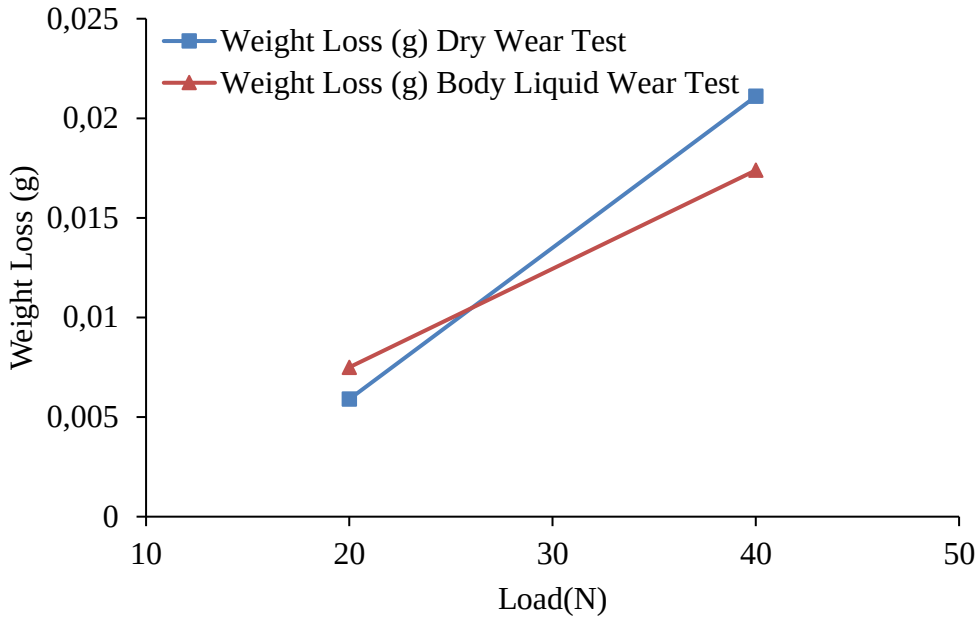


Figure 4.19. Change of wear test results of Ni-Ti SMA with applied load.

Table 4.12. Wear test results.

| **Test Conditions** | **Wear Rate (g/Nm)($10^{-9}$)** |
|---|---|
| **Body Liquid Wear Test** | 1.35 |
| **Dry Wear Test** | 1.7 |

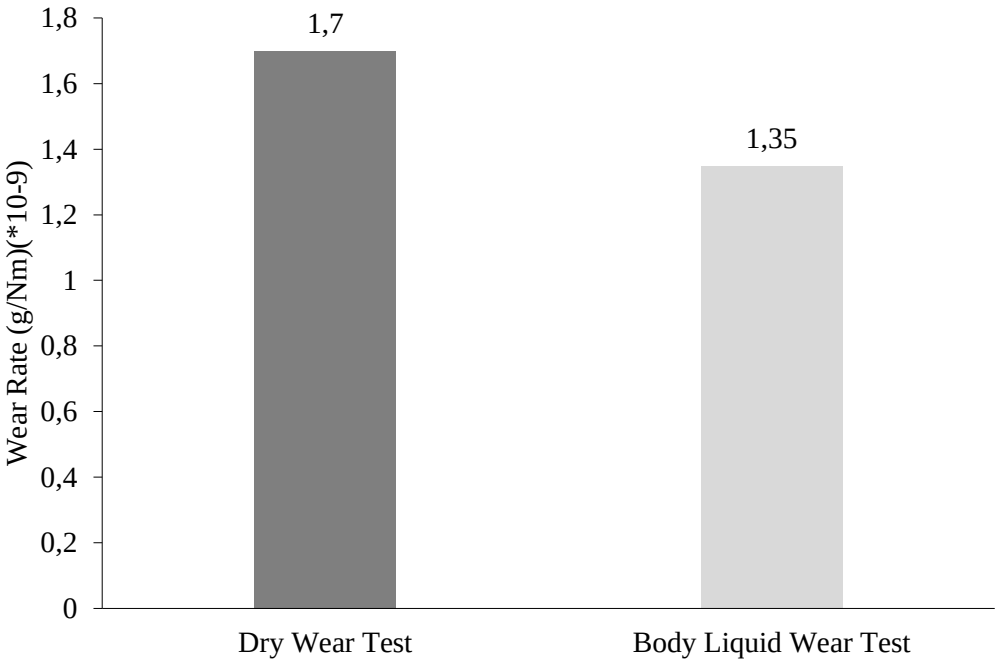


Figure 4.20. Change of wear test results of Ni-Ti SMA.

Figure 4.21 displays SEM and EDX pictures of the investigated alloy following the dry-air wear test. Abrasive slip tracks were observed on the scratched area of the alloy, aligned with the path of slip. The presence of abrasive wear mechanism in the Ni matrix led to a decrease in output. This mechanism caused erosion of the matrix towards the contact boundary, accompanied by deformation due to plasticity, resulting in additional weight loss. The SEM analysis reveals a clean and smooth surface, which is attributed to particle detachment caused by plastic deformation on the contact area surface. TiO2 formation is observed in regions 1.5, 6, and 7 during the analysis of SEM and EDX. Additionally, TiO2 formation is also observed in regions 2, 3, and 4 in which the CO2 layer is present.

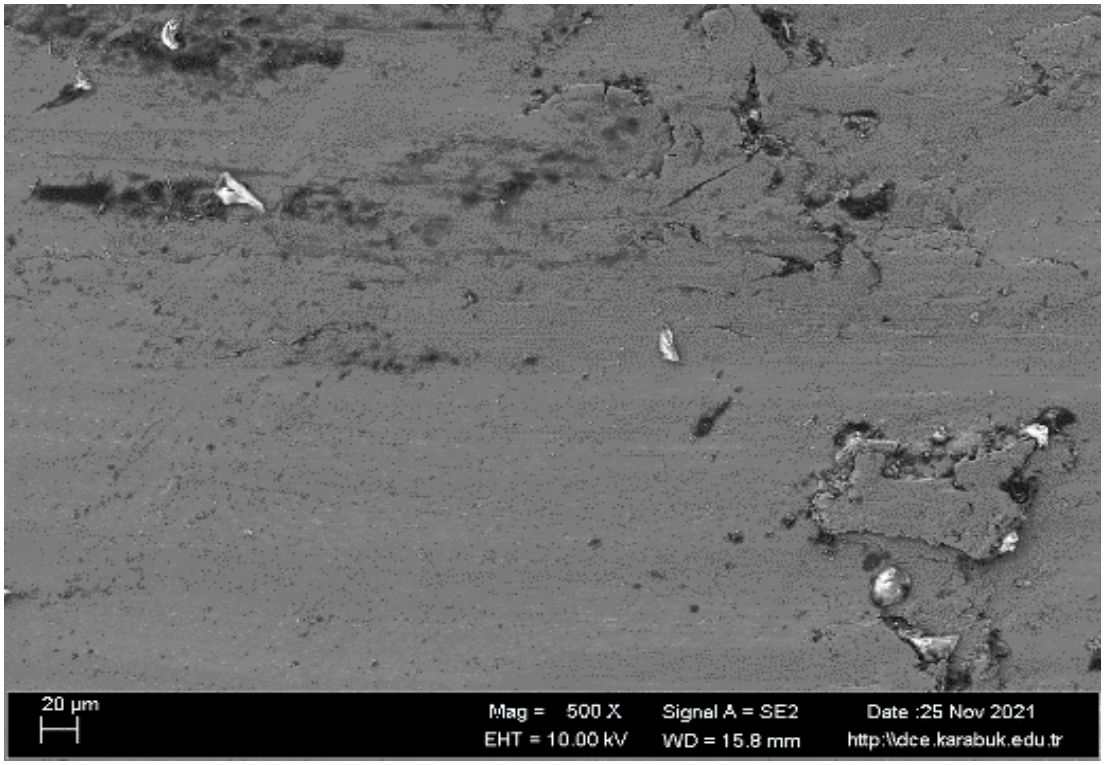


(a)

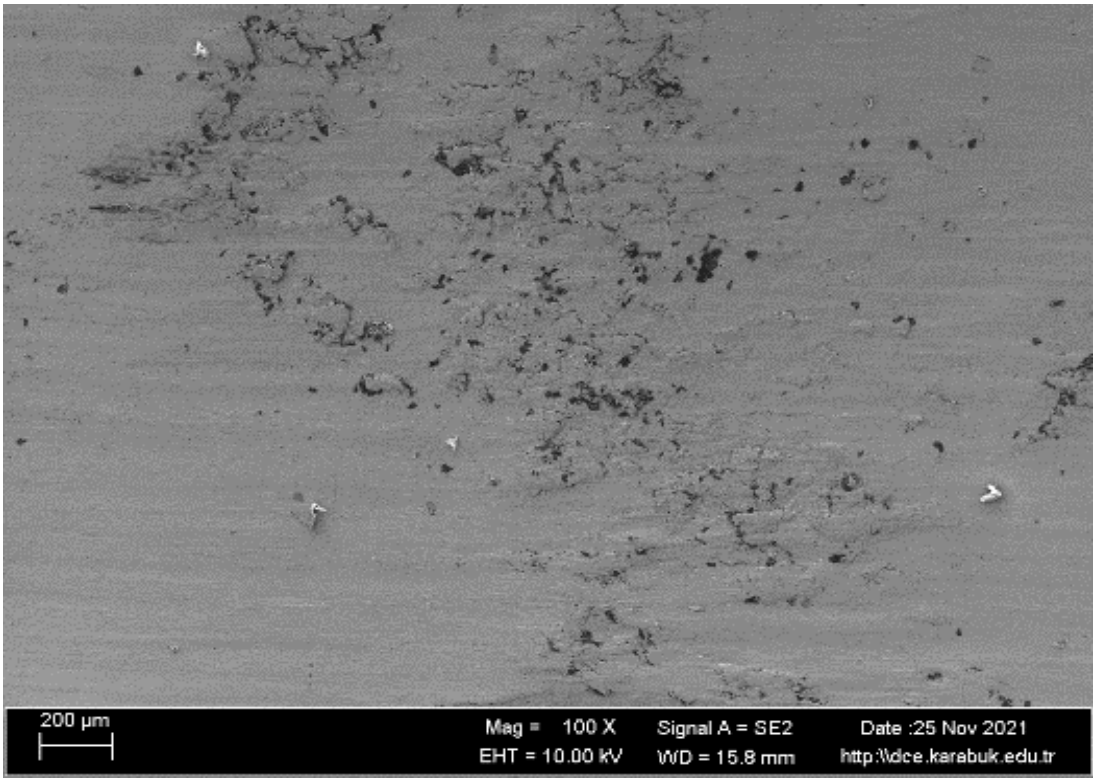
200 µm
Mag = 100 X
Signal A = SE2
Date :25 Nov 2021
EHT = 10.00 kV
WD = 15.8 mm
http:\\dce.karabuk.edu.tr

(b)

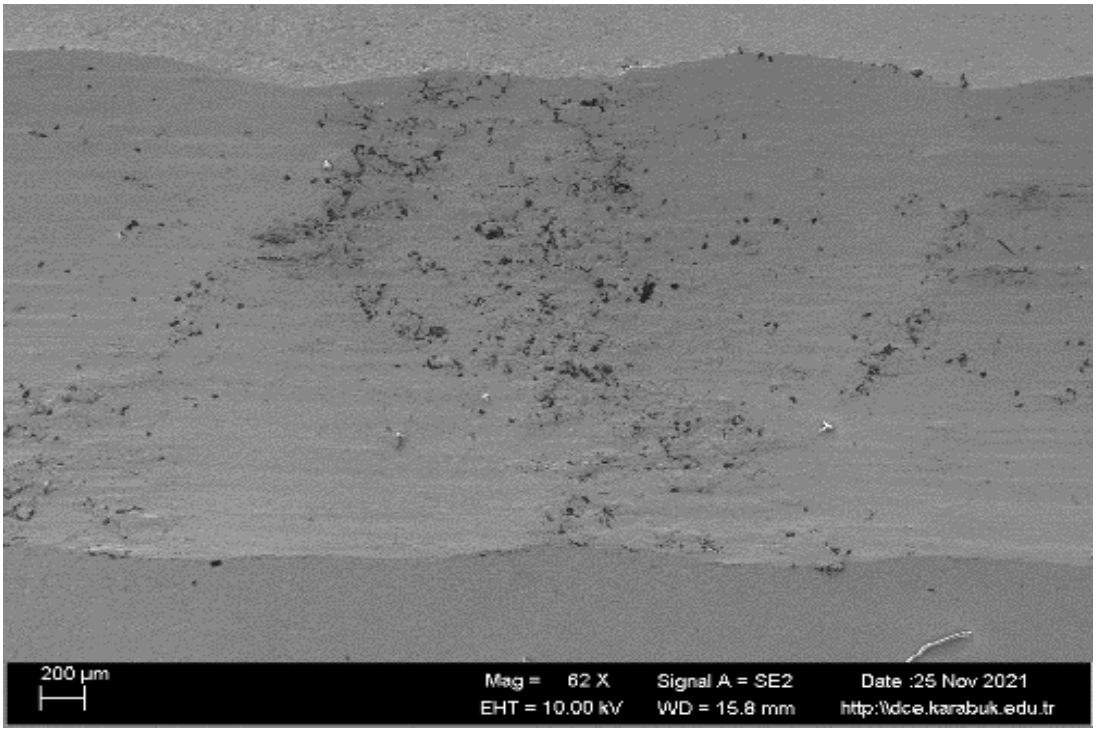
200 µm
Mag = 62 X
Signal A = SE2
Date :25 Nov 2021
EHT = 10.00 kV
WD = 15.8 mm
http:\\dce.karabuk.edu.tr

(c)

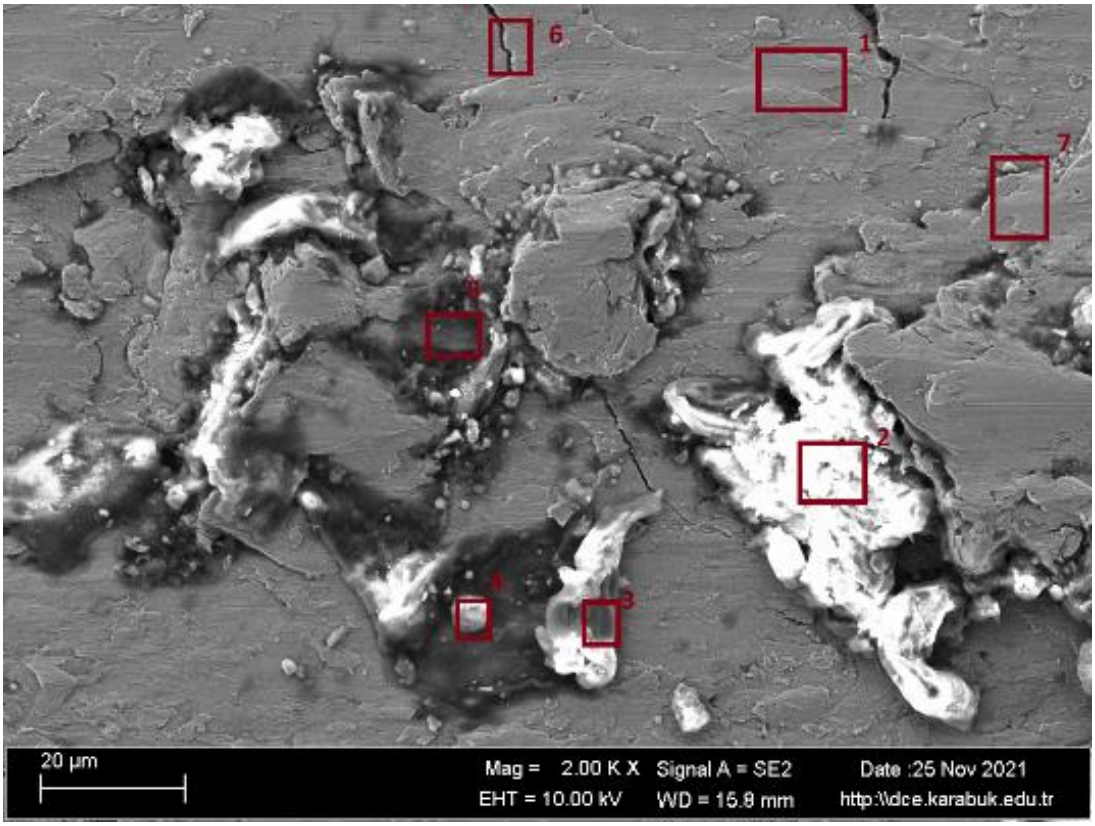


(d)

Figure 4.21. Wear of SMA (a, b) SEM (b) EDS images and analysis.

Table 4.13. Elemental response spectrum from the Fig. 4.21d

| **Wt. (%)** | | | | | | | | | |
|---|---|---|---|---|---|---|---|---|---|
| **Spectrum** | O | C | Mg | Na | Ca | K | Ni | Cu | Ti |
| **1** | 32.38 | 10.54 | 1.88 | 2.57 | 0.49 | 0.56 | 10.45 | 0.00 | 41.13 |
| **2** | 38.93 | 54.64 | 0.47 | 4.58 | 0.65 | 0.42 | 0.20 | 0.00 | 0.11 |
| **3** | 33.75 | 58.67 | 0.85 | 4.46 | 0.58 | 0.91 | 0.07 | 0.20 | 0.51 |
| **4** | 10.95 | 31.03 | 1.42 | 54.85 | 0.34 | 0.67 | 0.00 | 0.29 | 0.45 |
| **5** | 39.46 | 43.14 | 1.15 | 2.80 | 0.70 | 0.68 | 0.08 | 0.14 | 11.85 |
| **6** | 33.73 | 15.93 | 1.02 | 2.67 | 0.57 | 0.67 | 8.77 | 0.14 | 36.51 |
| **7** | 37.82 | 24.56 | 0.85 | 3.76 | 0.06 | 0.26 | 5.82 | 0.00 | 26.87 |
| **Mean value:** | 32.43 | 34.07 | 1.,09 | 10.82 | 0.48 | 0.59 | 3.63 | 0.11 | 16.78 |
| **Sigma:** | 9.88 | 18.68 | 0.46 | 19.44 | 0.22 | 0.21 | 4.62 | 0.11 | 17.88 |
| **Sigma means:** | 3.73 | 7.06 | 0.17 | 7.35 | 0.08 | 0.08 | 1.74 | 0.04 | 6.76 |

Figure 4.22 presents the SEM pictures and the EDS evaluation outcomes of the SMA. The literature reports the X-ray diffraction analysis of the material following wear tests conducted in Hank's solution. It has been observed that formation and reorientation of martensite layers occur in β- and martensite alloys, respectively. In contrast to the findings of the dry wear test conducted on the alloy, it was observed that the plates

exhibited a greater degree of reorientation upon undergoing a change in phase to the martensite phase when subjected to applied stress during examination. The presence of this condition, along with the development of a layer of oxide, enhanced the resistance to corrosive wear compared to dry wear. Upon examination of the SEM images, it is evident that the alloy under investigation demonstrates abrasive wear. Based on the EDX analysis, CO2 is believed to be present in regions 2, 3, 5, and 7, while TiO2 is found in regions 1, 4, and 6.

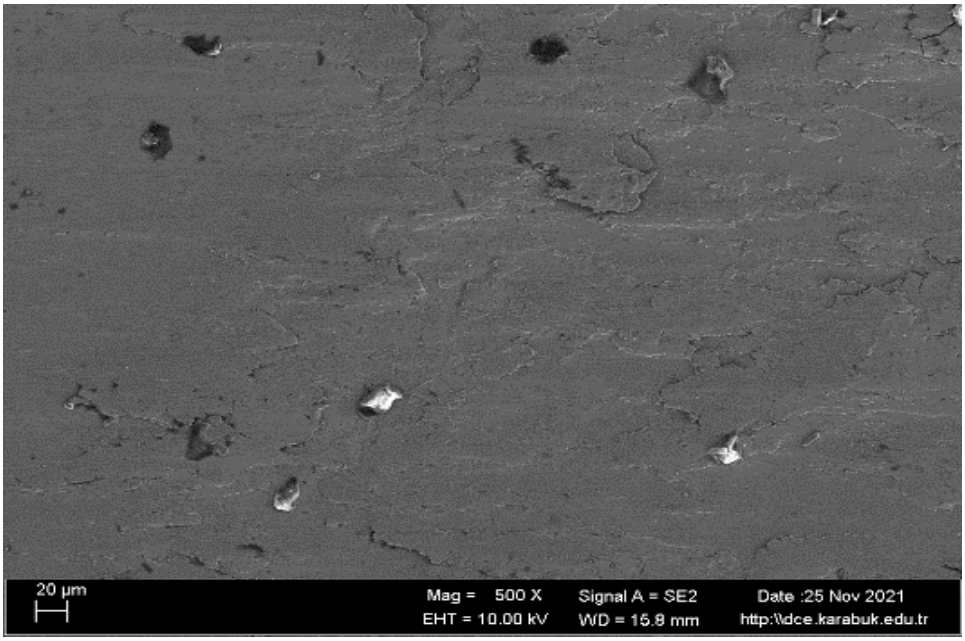


(a)

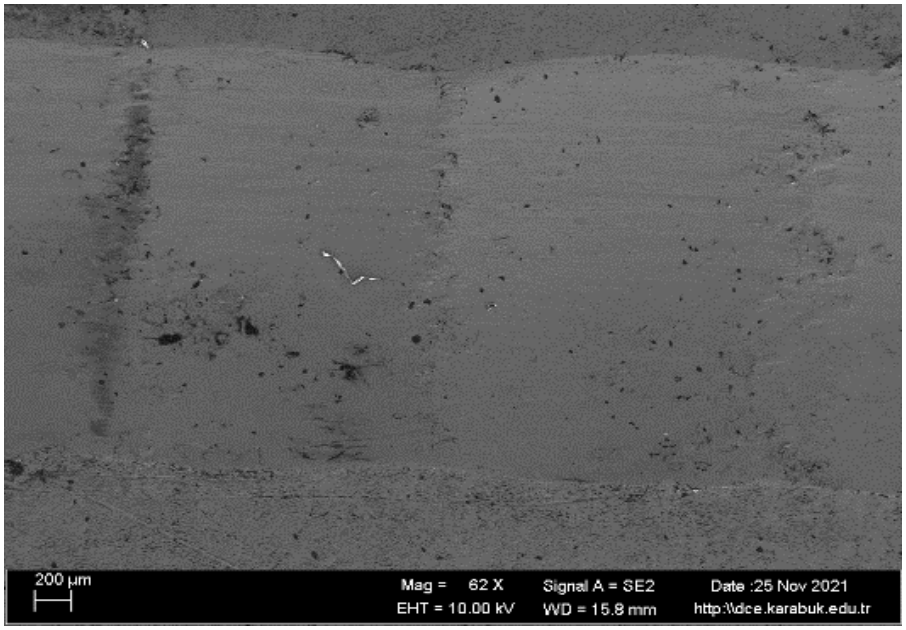


(b)

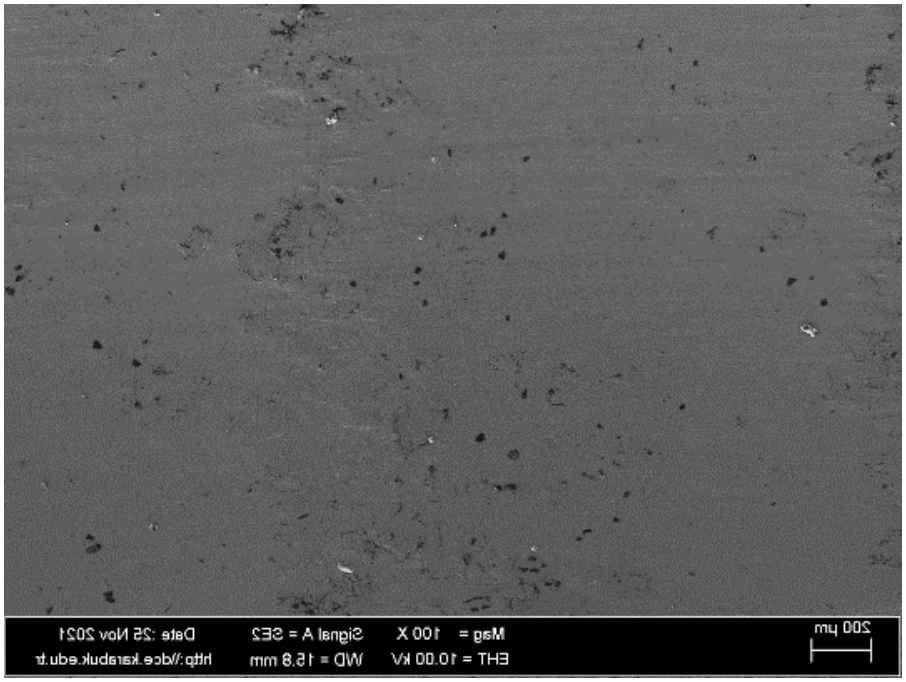


(c)

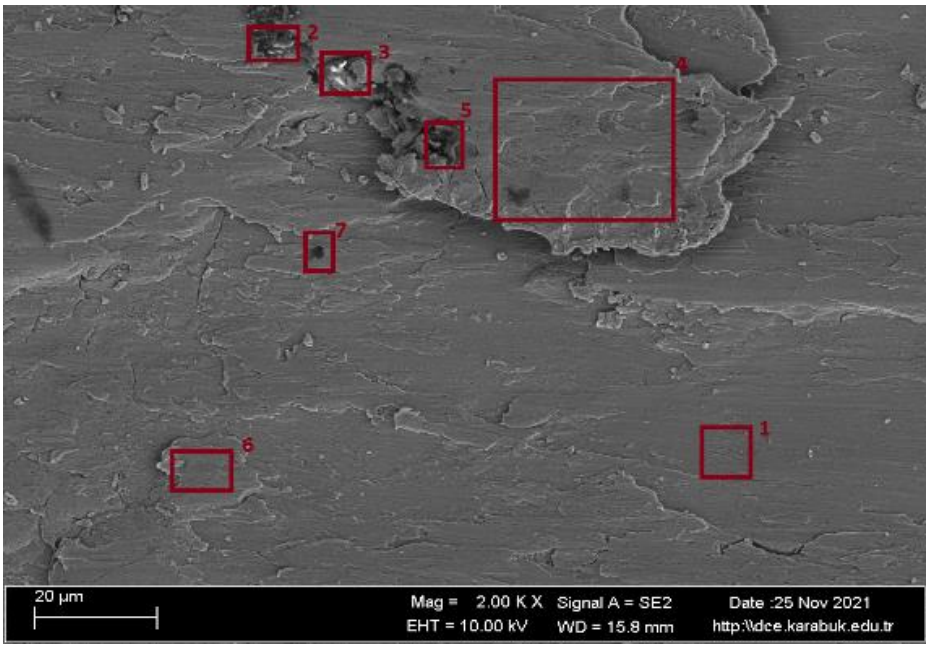


(d)

Figure 4.22. Corrosive Wear SEM pictures and EDS analysis of SMA.

Table 4.14. Elemental response spectrum from the Fig. 4.22d

| Wt. (%) Spectra | C | Cu | Na | O | K | Mg | Ti | Ca | Ni |
|---|---|---|---|---|---|---|---|---|---|
| 1 | 6.97 | 0.00 | 3.44 | 26.22 | 0.00 | 1.75 | 48.33 | 0.65 | 12.63 |
| 2 | 32.51 | 0.00 | 4.29 | 52.42 | 1.40 | 0.90 | 7.11 | 1.14 | 0.24 |
| 3 | 37.36 | 0.06 | 3.74 | 44.98 | 1.16 | 0.67 | 10.54 | 0.69 | 0.79 |
| 4 | 9.19 | 0.96 | 2.44 | 41.51 | 0.13 | 0.95 | 34.57 | 0.17 | 10.09 |
| 5 | 36.21 | 0.00 | 3.85 | 47.42 | 0.92 | 0.63 | 8.77 | 0.76 | 1.44 |
| 6 | 8.92 | 0.87 | 2.77 | 38.48 | 0.00 | 1.83 | 36.02 | 0.56 | 10.55 |
| 7 | 38.65 | 0.00 | 1.12 | 35.63 | 0.00 | 0.70 | 22.50 | 0.61 | 0.79 |
| Mean value: | 24.26 | 0.27 | 3.09 | 40.95 | 0.52 | 1.06 | 23.98 | 0.66 | 5.22 |
| Sigma: | 15.01 | 0.44 | 1.08 | 8.58 | 0.62 | 0.51 | 16.07 | 0.29 | 5.56 |
| Sigma means: | 5.67 | 0.17 | 0.41 | 3.24 | 0.23 | 0.19 | 6.07 | 0.11 | 2.10 |

## 4.6. DSC (DIFFERENTIAL SCANNING CALORIMETRY) TEST RESULTS

The application areas of shape memory alloys (SMAs) include transformation of phase temperatures and hysteresis. In this section, the phase temperatures for transformation have been identified using DSC analysis. Heat-treated nitinol alloys typically undergo a direct single transformation from austenite to martensite upon cooling. The specimen has been examined twice to validate the results obtained from the initial DSC analysis. The analyses yielded similar results. The analysis yielded the determination of the austenite phase start (As) and finish (Af) temperatures, as well as the martensite phase begin (Ms) and complete (Mf) temperatures for the NiTi alloy. Figure 4.7 illustrates that the peak temperature value during the austenite phase transformation, also known as the shape memory temperature, was approximately 32°C. Similarly, the peak temperature during the martensite phase of transformation was approximately 20°C. The observed transformation temperatures indicate the potential suitability of NiTi shape memory alloy (SMA) for applications in the medical domain. Consistent DSC analysis findings were observed in previous investigations regarding the application of NiTi alloys in this particular domain [80].

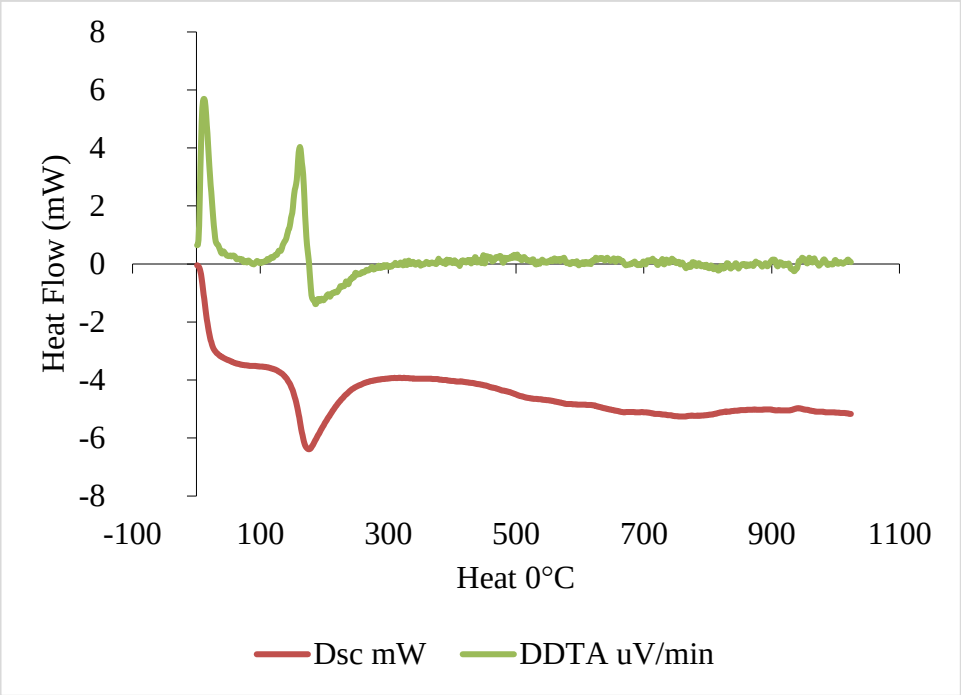


Figure 4.23. DSC plot of nitinol samples.

# PART 5

## CONCLUSIONS

This study investigated the dry wear behavior of Nitinol, wear in Hank fluid, immersion corrosion behavior in body fluid, potentiodynamic polarization test, microstructure characterization, and wear mechanisms. The study observed the following results:

Based on the findings from a 8-day immersion corrosion test, it was observed that the initial two days exhibited a gradual decrease in mass, with a loss of 0.002 mg/dm2 at the conclusion of the first day and 0.02 mg/dm2 at the conclusion of the second day, indicating an accelerating trend. On the fourth day, the acceleration reached 26 and remained constant for the subsequent four days. The value rose to 31.13 on the fifth day, reached 41.43 on both the sixth and seventh days, stayed constant, and then declined to 39.89 mg/dm2 in the eighth day of measurement. The nonlinear behavior observed in this study was attributed to the cyclic formation and disruption of the oxide barrier on the surface.

The mass loss during the 300m dry abrasion test beneath a 20 N load was 0.0059. However, in the abrasion test conducted in Hank fluid under the same load and distance, the mass loss raised to 0.0075 g. The mass loss under a 40 N load was 0.0211 g in dry wear and reduced to 0.01739 g in the wear experiment employing Hank fluid. The wear rates observed in the dry and hank fluid wear tests were 1.7 and 1.35 (g/Nm)x10-9, respectively.

The SEM examination findings indicate that the predominant wear mechanism observed on the wear surfaces is abrasion. TiO2 oxide layers are also observed on the wear surface.

The initial Icorr measurements during the 23-day electro-potential-dynamic corrosion examination were 471.7x10-9 (A/cm2), which decreased to 47.03x10-9 (A/cm2) on the second day. The Icorr value showed an initial increase on the second day and reached its highest point on the 15th day at 499.33 x10-9 (A/cm2). Subsequently, it decreased to 273.33 x10-9 (A/cm2) by the 23rd day. The change is attributed to the formation of a Titanium oxide layer on the surface, which leads to a decrease in electrical resistance and current as the film thickness increases. Over time, the surface coating undergoes a reforming process, resulting in a decrease in the recent corrosion current (Icorr). This study provides evidence of the capabilities of NiTi material. Create a protective surface film even when subjected to high electric potential.

In summary, the immersion and potentiodynamic oxidation examinations performed on Nitinol in Hank's fluid yielded significant findings regarding the corrosion characteristics of this shape memory alloy. The immersion test demonstrated Nitinol's strong resistance to corrosion in Hank's fluid, as no obvious indications of corrosion or deterioration were observed throughout the test duration. Nitinol may be deemed a viable substance for biomedical applications in the presence of Hank's fluid. The potentiodynamic oxidation test confirmed Nitinol's corrosion resistance in Hank's fluid. The obtained polarization curves demonstrated that Nitinol displayed passive characteristics, characterized by a consistent inactive current density and a notably high passive potential. Nitinol demonstrates the formation of a protective oxide layer on its surface, effectively inhibiting corrosion in Hank's fluid. The test results align with prior research on the corrosion-related properties of Nitinol in different environments. Nitinol exhibits self-passivation by developing an oxide barrier when exposed to corrosive substances. The oxide layer functions as a barrier, inhibiting the diffusion of corrosive substances and decreasing the rate of corrosion of the alloy. The resistance to corrosion of Nitinol in Hank's fluid is due to the existence of a stable and bound oxide film on its outer layer. The oxide layer consists mainly of titanium dioxide (TiO2) and nickel oxide (NiO), both of which exhibit strong corrosion resistance. The oxide layer formation is aided by the inclusion of a small quantity of nickel in the Nitinol metal, which improves the material's passivation characteristics. The study's findings have significant implications for the utilization of Nitinol in biomedical contexts. The corrosion resistance of Nitinol in Hank's fluid indicates its suitability for

use in medical devices and implants that are exposed to biological fluids. The oxide layer formed on Nitinol's surface is stable and protective, offering long-term corrosion protection. This ensures the material's integrity and functionality in physiological environments. The resistance to corrosion of Nitinol can be affected by factors including alloy composition, surface finish, and the specific usage environment. Additional research is required to examine the resistance to corrosion of Nitinol in various environments and to enhance its efficacy for specific biomedical uses. The immersion and potentiodynamic corrosion tests carried out on Nitinol in Hank's fluid have yielded important insights into the corrosion behavior of this shape memory alloy (SMA). The findings indicate that Nitinol exhibits exceptional corrosion resistance when exposed to Hank's fluid, suggesting its potential suitability for use in biomedical applications. Additional research in this field will enhance the advancement of Nitinol-based medical instruments and implants.

Discussion: The immersion and potentiodynamic corrosion tests carried out on Nitinol in Hank's fluid have yielded significant insights into the corrosion behavior of this shape memory alloy. The test results demonstrate Nitinol's exceptional corrosion resistance in Hank's fluid, rendering it a viable material for biomedical purposes. The immersion test consisted of submerging Nitinol samples in Hank's fluid for a predetermined duration, followed by the examination of the samples for any indications of corrosion or degradation. The lack of observable corrosion or degradation following the immersion test indicates that Nitinol exhibits significant resistance to corrosion in Hank's fluid. This finding aligns with prior research that has examined the corrosion resistance of Nitinol in different environmental conditions. The potentiodynamic corrosion test was conducted to measure the curves of polarization of Nitinol in Hank's fluid. Polarization curves offer insights into the corrosion characteristics of a material, encompassing its passive potential and passive current density. The potentiodynamic corrosion test results indicated that Nitinol demonstrated passive behavior characterized by a constant passive current density and a high passive potential. Nitinol demonstrates the ability to generate an oxide barrier on its outer layer, thereby effectively inhibiting corrosion in Hank's fluid. The presence of nickel in the Nitinol alloy is responsible for the development of the oxide barrier on its surface. Nickel improves the passivation characteristics of Nitinol, resulting in the

development of a durable and firmly attached oxide film. The oxide layer, consisting mainly of the titanium dioxide and nickel oxide, functions as a barrier that inhibits the diffusion of corrosive substances and decreases the corrosion rate of the alloy. The corrosion resistance of Nitinol in Hank's fluid has significant implications for its utilization in biomedical applications. Nitinol medical devices and implants can safely interact with biological liquids without experiencing corrosion or degradation. The oxide layer on Nitinol's surface offers durable corrosion protection, safeguarding the material's integrity and functionality in physiological environments. The behavior of corrosion of Nitinol can be impacted by multiple factors. The corrosion resistance of Nitinol can be influenced by factors such as alloy composition, finish of the surface, and the specific environmental conditions in which it is utilized. Additional research is required to examine the corrosion characteristics of Nitinol in various environments and to enhance its efficacy for specific biomedical uses. In summary, the immersion and potentiodynamic corrosion examinations have yielded significant findings regarding the corrosion characteristics of Nitinol in Hank's fluid. The results indicate that Nitinol exhibits exceptional corrosion resistance, rendering it a highly promising material for use in biomedical applications. Additional research in this field will enhance the advancement of Nitinol-based medical instruments and implants.

## REFERENCES


[1] S. M. Mirvakili and I. W. Hunter, "Artificial Muscles: Mechanisms, Applications, and Challenges," *Advanced Materials*, 2017.

[2] G. Plotino, A. Costanzo, N. M. Grande, R. Petrovic, L. Testarelli, and G. Gambarini, "Experimental Evaluation on the Influence of Autoclave Sterilization on the Cyclic Fatigue of New Nickel-Titanium Rotary Instruments," *Journal of Endodontics*, 2012.

[3] K. Alvarez and H. Nakajima, "Metallic Scaffolds for Bone Regeneration," *Materials*, 2009.

[4] A. A. Zadpoor, "Additively Manufactured Porous Metallic Biomaterials," *Journal of Materials Chemistry B*, 2019.

[5] M. S. Safavi, A. Bordbar-Khiabani, J. Khalil-Allafi, M. Mozafari, and L. Visai, "Additive Manufacturing: An Opportunity for the Fabrication of Near-Net-Shape NiTi Implants," *Journal of Manufacturing and Materials Processing*, 2022.

[6] saqlain zaman *et al.*, "Implementation of Smart Materials for Actuation of Traditional Valve Technology for Hybrid Energy Systems," 2022.

[7] S. Alipour, F. Taromian, E. R. Ghomi, M. Zare, S. Singh, and S. Ramakrishna, "Nitinol: From Historical Milestones to Functional Properties and Biomedical Applications," *Proceedings of the Institution of Mechanical Engineers Part H Journal of Engineering in Medicine*, 2022.

[8] S. Gao, O. P. Bodunde, M. Qin, W.-H. Liao, and P. Guo, "Microstructure and Phase Transformation of Nickel-Titanium Shape Memory Alloy Fabricated by Directed Energy Deposition With in-Situ Heat Treatment," *Journal of Alloys and Compounds*, 2022.

[9] N. Kovač, Š. Ivošević, G. Vastag, P. Majerič, and R. Rudolf, "Multivariate Regression Analysis of the NiTi Alloys' Surface Corrosion Depending on the Measured Oxygen Value: Tests in Three Different Marine Environments," *Crystals*, 2022.

[10] A. Asserghine, M. Medvidović-Kosanović, A. Stanković, L. Nagy, R. M. Souto, and G. Nagy, "A Scanning Electrochemical Microscopy Characterization of the Localized Corrosion Reactions Occurring on Nitinol in Saline Solution After Anodic Polarization," *Sensors and Actuators B Chemical*, 2020.

[11] S. Kadam, A. K. Jaiswal, and S. Kadam, "Artificial Bone via Bone Tissue Engineering: Current Scenario and Challenges," *Tissue Engineering and Regenerative Medicine*, 2017.

[12] D. D. Kiradzhiyska and R. D. Mantcheva, "Overview of Biocompatible

Materials and Their Use in Medicine," *Folia Medica*, 2019.

[13] N. A. Zarkevich and D. D. Johnson, "Stable Atomic Structure of NiTi Austenite," *Physical Review B*, 2014.

[14] J.-N. Zhu *et al.*, "Controlling Microstructure Evolution and Phase Transformation Behavior in Additive Manufacturing of Nitinol Shape Memory Alloys by Tuning Hatch Distance," *Journal of Materials Science*, 2022.

[15] N. A. Zarkevich and D. D. Johnson, "Shape-Memory Transformations of NiTi: Minimum-Energy Pathways Between Austenite, Martensites, and Kinetically Limited Intermediate States," *Physical Review Letters*, 2014.

[16] M. Guillory and P. Vall, "Past, Present, and Future Trends of Nickel Titanium Rotary Instrumentation," *Journal of Veterinary Dentistry*, 2022.

[17] A. Tuissi, G. Rondelli, and P. Bassani, "Plasma Arc Melting (PAM) and Corrosion Resistance of Pure NiTi Shape Memory Alloys," *Shape Memory and Superelasticity*, 2015.

[18] E. O. Nasakina, M. A. Sudarchikova, K. V Sergienko, S. V Konushkin, and M. A. Sevostyanov, "Ion Release and Surface Characterization of Nanostructured Nitinol During Long-Term Testing," *Nanomaterials*, 2019.

[19] M. El-Tahan and M. Dawood, "Bond Behavior of NiTiNb SMA Wires Embedded in CFRP Composites," *Polymer Composites*, 2017.

[20] B. Arrotin *et al.*, "A Comparative Study of the Electro-Assisted Grafting of Mono- And Bi-Phosphonic Acids on Nitinol," *Surfaces*, 2019.

[21] N. Rawat, M. Benčina, E. Gongadze, I. Junkar, and A. Iglič, "Fabrication of Antibacterial TiO 2 Nanostructured Surfaces Using the Hydrothermal Method," *ACS Omega*, vol. 7, no. 50, pp. 47070–47077, Dec. 2022.

[22] S. Shabalovskaya, J. W. Anderegg, F. Laab, P. A. Thiel, and G. Rondelli, "Surface Conditions of Nitinol Wires, Tubing, and as-Cast Alloys. The Effect of Chemical Etching, Aging in Boiling Water, and Heat Treatment," *Journal of Biomedical Materials Research*, 2003.

[23] M. R. Derakhshandeh, M. Farvizi, and M. Javaheri, "Effects of High-Pressure Torsion Treatment on the Microstructural Aspects and Electrochemical Behaviour of Austenitic NiTi Shape Memory Alloy," *Journal of Solid State Electrochemistry*, 2020.

[24] I. Polozov and A. Popovich, "Microstructure and Mechanical Properties of NiTi-Based Eutectic Shape Memory Alloy Produced via Selective Laser Melting in-Situ Alloying by Nb," *Materials*, 2021.

[25] S. Attarilar, M. Ebrahimi, F. Djavanroodi, Y. Fu, L. Wang, and J. Yang, "3D Printing Technologies in Metallic Implants: A Thematic Review on the Techniques and Procedures," *International Journal of Bioprinting*, 2021.

[26] K. J. Liu, H. T. Liu, and J. Li, “Thermal expansion and bandgap properties of bi-material triangle re-entrant honeycomb with adjustable Poisson’s ratio,” *International Journal of Mechanical Sciences*, vol. 242, no. October 2022, p. 108015, 2023.

[27] A. Jahadakbar *et al.*, “Design, Modeling, Additive Manufacturing, and Polishing of Stiffness-Modulated Porous Nitinol Bone Fixation Plates Followed by Thermomechanical and Composition Analysis,” *Metals*, 2020.

[28] E. Nigito, F. Diemer, S. Husson, S. F. Ou, M. H. Tsai, and F. Rezai-Aria, “Microstructure of NiTi Superelastic Alloy Manufactured by Selective Laser Melting,” *Materials Letters*, 2022.

[29] D. S. T W Duerig, K N Melton, *Engineering Aspects of Shape Memory Alloys*, 1st ed. 1990.

[30] B. D. Clarke, W. M. Carroll, Y. Rochev, M. Hynes, D. Bradley, and D. Plumley, “Influence of Nitinol Wire Surface Treatment on Oxide Thickness and Composition and Its Subsequent Effect on Corrosion Resistance and Nickel Ion Release,” *Journal of Biomedical Materials Research Part A*, 2006.

[31] D. M. Korotin *et al.*, “Arsenic Contamination of Coarse-Grained and Nanostructured Nitinol Surfaces Induced by Chemical Treatment in Hydrofluoric Acid,” *Journal of Biomedical Materials Research Part B Applied Biomaterials*, 2012.

[32] W. M. Carroll and M. J. Kelly, “Corrosion Behavior of Nitinol Wires in Body Fluid Environments,” *Journal of Biomedical Materials Research Part A*, 2003.

[33] A. A. M. Soltan, İ. Esen, S. A. Kara, and H. Ahlatçı, “Examination of the Corrosion Behavior of Shape Memory NiTi Material for Biomedical Applications,” *Materials*, vol. 16, no. 11, p. 3951, May 2023.

[34] K. Yang *et al.*, “Efficacy and Safety of a Parylene-Coated Occluder for Atrial Septal Defect: A Prospective, Multi-Center, Randomized Controlled Clinical Trial,” *Chinese Medical Journal*, 2021.

[35] D. R. N. Correa *et al.*, “Development of Ti-15Zr-Mo Alloys for Applying as Implantable Biomedical Devices,” *Journal of Alloys and Compounds*, 2018.

[36] A. W. Hadi, A. F. Mahde, and M. N. Arbilei, “Introducing Cobalt Nickel Aluminum Ferromagnetic Shape Memory Alloy for Endodontic File Manufacturing,” *International Journal of Health Sciences*, 2022.

[37] P. Dong, R. Yao, Z. Yan, W. Wang, H. Xiuli, and J. Zhou, “Microstructure and Corrosion Resistance of Laser-Welded Crossed Nitinol Wires,” *Materials*, 2018.

[38] N. Dong *et al.*, “Effect of nanodiamond content on the hot deformation behaviors of ND/ZK60 composites,” *Diamond and Related Materials*, vol. 125, no. March, p. 108983, 2022.

[39] A. Jacques, J. Delhalle, and Z. Mekhalif, “Surface-Initiated ATRP of (Hydroxyethyl)Methacrylate on Nitinol Modified by in Situ Generated Diazonium From Its Nitro Precursor,” *Ecs Meeting Abstracts*, 2015.

[40] N. S. Moghaddam *et al.*, “Achieving Superelasticity in Additively Manufactured NiTi in Compression Without Post-Process Heat Treatment,” *Scientific Reports*, 2019.

[41] T. G. Bradley, W. A. Brantley, and B. M. Culbertson, “Differential scanning calorimetry (DSC) analyses of superelastic and nonsuperelastic nickel-titanium orthodontic wires,” *American Journal of Orthodontics and Dentofacial Orthopedics*, vol. 109, no. 6, pp. 589–597, Jun. 1996.

[42] É. S. J. Pereira, A. L. d’Ávila Viana, V. T. L. Buono, O. A. Peters, and M. G. de Azevedo Bahia, “Behavior of Nickel-Titanium Instruments Manufactured With Different Thermal Treatments,” *Journal of Endodontics*, 2015.

[43] C. A. Biffi, P. Bassani, J. Fiocchi, and A. Tuissi, “Microstructural and Mechanical Response of NiTi Lattice 3D Structure Produced by Selective Laser Melting,” *Metals*, 2020.

[44] J. C. Chekotu, D. J. Kinahan, R. Goodall, and D. Brabazon, “Influence of Structural Porosity and Martensite Evolution on Mechanical Characteristics of Nitinol via In-Silico Finite Element Approach,” *Materials*, vol. 15, no. 15, p. 5365, Aug. 2022.

[45] S. O. Omid, Z. Goudarzi, L. M. Kangarshahi, A. Mokhtarzade, and F. Bahrami, “Self-Expanding Stents Based on Shape Memory Alloys and Shape Memory Polymers,” *Journal of Composites and Compounds*, 2020.

[46] P. Keerthana, S. B. Puneeth, and P. Chitra, “In Vivo Comparison of Ultimate Tensile Strength and Surface Topography of Three Different Nickel–Titanium Archwires,” *The Journal of Indian Orthodontic Society*, 2021.

[47] V. Di Cocco, F. Iacoviello, S. Natali, and V. Volpe, “Fatigue Crack Behavior on a Cu-Zn-Al SMA,” *Frattura Ed Integrità Strutturale*, 2014.

[48] V. S. Nair and N. Radhika, “The Role of NiTi Shape Memory Alloys in Quality of Life Improvement Through Medical Advancements: A Comprehensive Review,” *Proceedings of the Institution of Mechanical Engineers Part H Journal of Engineering in Medicine*, 2022.

[49] S. D. Igoshin, “Investigation of the Gradient Properties of Samples Obtained by Direct Laser Deposition From a Mixture of Ni/Ti Elemental Powders,” *Key Engineering Materials*, 2023.

[50] Q. Li, Y. Zeng, and X. Tang, “The Applications and Research Progresses of Nickel–titanium Shape Memory Alloy in Reconstructive Surgery,” *Australasian Physical \& Engineering Sciences in Medicine*, 2010.

[51] A. Bansiddhi, T. Sargeant, S. I. Stupp, and D. C. Dunand, “Porous NiTi for

Bone Implants: A Review," *Acta Biomaterialia*, 2008.

[52] H. Ibrahim, A. Jahadakbar, A. Dehghan, N. S. Moghaddam, A. Amerinatanzi, and M. Elahinia, "In Vitro Corrosion Assessment of Additively Manufactured Porous NiTi Structures for Bone Fixation Applications," *Metals*, 2018.

[53] S. S. Kashyap, S. Upadhyaya, and S. Gur, "Stochastic Seismic Response of Building With Shape Memory Alloy Damper," *E3s Web of Conferences*, 2022.

[54] S. K. Sadrnezhaad, M. H. Parsafar, Y. Rashtiani, and M. Jadidi, "Nitinol Spinal Vertebrae: A Favorable New Substitute," *International Journal of Engineering*, 2019.

[55] R. Davis *et al.*, "A Comprehensive Review on Metallic Implant Biomaterials and Their Subtractive Manufacturing," *The International Journal of Advanced Manufacturing Technology*, 2022.

[56] M. Chapman, M. De Graef, R. James, and X. Chen, "Quantitative Analysis of Compatible Microstructure by Electron Backscatter Diffraction," *Philosophical Transactions of the Royal Society a Mathematical Physical and Engineering Sciences*, 2021.

[57] M. J. Mirzaali, V. Moosabeiki, S. M. Rajaai, J. Zhou, and A. A. Zadpoor, "Additive Manufacturing of Biomaterials—Design Principles and Their Implementation," *Materials*, 2022.

[58] L. Válková, J. Ševčíková, M. P. Goldbergová, A. Weiser, and A. Dlouhý, "Osteoarthritic Process Modifies Expression Response to NiTi Alloy Presence," *Journal of Materials Science Materials in Medicine*, 2018.

[59] A. Bouaissi, N. S. Radhi, K. F. Morad, M. H. Hafiz, and A. A. Atiyah, "Optimization of Nickel Content on Some Properties of (Niti) Shape Memory Alloy," *Knowledge-Based Engineering and Sciences*, 2020.

[60] B. Młocek, Z. Lekston, M. Zubko, R. J, and K. Stróż, "Phase Analysis of NiTi Shape Memory Wires and Computer Simulations of the Superelastic Effect," *Acta Physica Polonica A*, 2016.

[61] G. Zorn *et al.*, "Tailoring the Surface of NiTi Alloy Using PIRAC Nitriding Followed by Anodization and Phosphonate Monolayer Deposition," *Chemistry of Materials*, 2008.

[62] K. McNamara, O. Kolaj-Robin, S. Belochapkine, F. Laffir, A. A. Gandhi, and S. A. M. Tofail, "Surface Chemistry and Cytotoxicity of Reactively Sputtered Tantalum Oxide Films on NiTi Plates," *Thin Solid Films*, 2015.

[63] I. Stachiv, E. Alarcon, and M. Lamac, "Shape Memory Alloys and Polymers for MEMS/NEMS Applications: Review on Recent Findings and Challenges in Design, Preparation, and Characterization," *Metals*, vol. 11, no. 3, p. 415, Mar. 2021.

[64] K. M. F. De Britto, J. E. Spinelli, A. E. Martinelli, and R. M. Do Nascimento, "The effect of residence time on the tensile properties of superelastic and thermal activated Ni-Ti orthodontic wires," *Materials Research*, vol. 14, no. 3, pp. 423–427, 2011.

[65] Z. BAO, S. GUO, F. XIAO, and X. ZHAO, "Development of NiTiNb in-situ composite with high damping capacity and high yield strength," *Progress in Natural Science: Materials International*, vol. 21, no. 4, pp. 293–300, Aug. 2011.

[66] S. Hellberg, J. Hummel, P. Krooß, T. Niendorf, and S. Böhm, "Microstructural and mechanical properties of dissimilar nitinol and stainless steel wire joints produced by micro electron beam welding without filler material," *Welding in the World*, vol. 64, no. 12, pp. 2159–2168, Dec. 2020.

[67] K. Khanlari, Q. Shi, K. Li, P. Xu, P. Cao, and X. Liu, "An investigation into the possibility to eliminate the microstructural defects of parts printed using a Ni-rich Ni-Ti elemental powder mixture," *Materials Research Express*, vol. 7, no. 10, p. 106503, 2020.

[68] S. Dilibal, H. Sahin, E. Dursun, and E. D. Engeberg, "Nickel–titanium shape memory alloy-actuated thermal overload relay system design," *Electrical Engineering*, vol. 99, no. 3, pp. 923–930, Sep. 2017.

[69] S. Pan, R. Yue, H. Hui, and S. Fan, "Lateral cyclic behavior of bridge columns confined with pre-stressed shape memory alloy wires," *Journal of Asian Architecture and Building Engineering*, vol. 21, no. 1, pp. 66–79, Jan. 2022.

[70] H. Holman, M. N. Kavarana, and T. K. Rajab, "Smart Materials in Cardiovascular Implants: Shape Memory Alloys and Shape Memory Polymers," *Artificial Organs*, 2020.

[71] X. Liu *et al.*, "Fabrication of Ni-Rich 58NiTi and 60NiTi From Elementally Blended Ni and Ti Powders by a Laser Powder Bed Fusion Technique: Their Printing, Homogenization and Densification," *International Journal of Molecular Sciences*, 2022.

[72] O. de Sousa Santos, M. M. da Silva, L. Pichon, O. D. Rigo, and J. Otubo, "Characterization of a NiTi SMA wire treated by nitrogen plasma based ion implantation (PBII)," *Procedia Structural Integrity*, vol. 2, pp. 1443–1450, 2016.

[73] I. Kaya *et al.*, "Effects of aging on the shape memory and superelasticity behavior of ultra-high strength Ni 54 Ti 46 alloys under compression," *Materials Science and Engineering: A*, vol. 678, pp. 93–100, Dec. 2016.

[74] C.-H. Kuang, C. Chien, and S.-K. Wu, "Multistage martensitic transformation in high temperature aged Ti48Ni52 shape memory alloy," *Intermetallics*, vol. 67, pp. 12–18, Dec. 2015.

[75] D. J. Wever, A. G. Veldhuizen, J. de Vries, H. J. Busscher, D. R. A. Uges, and

J. R. van Horn, “Electrochemical and surface characterization of a nickel–titanium alloy,” *Biomaterials*, vol. 19, no. 7–9, pp. 761–769, Apr. 1998.

[76] Q. Y. Wang and Y. F. Zheng, “The electrochemical behavior and surface analysis of Ti50Ni47.2Co2.8 alloy for orthodontic use,” *Dental Materials*, vol. 24, no. 9, pp. 1207–1211, Sep. 2008.

[77] M. H. Wong, F. T. Cheng, and H. C. Man, “Comparison of corrosion resistance and apatite-forming ability of NiTi treated by different low-temperature methods,” *Journal of Alloys and Compounds*, vol. 466, no. 1–2, pp. L5–L10, Oct. 2008.

[78] O. Cissé, O. Savadogo, M. Wu, and L. Yahia, “Effect of surface treatment of NiTi alloy on its corrosion behavior in Hanks’ solution,” *Journal of Biomedical Materials Research*, vol. 61, no. 3, pp. 339–345, Sep. 2002.

[79] M. Arciniegas, J. Casals, J. M. Manero, J. Peña, and F. J. Gil, “Study of hardness and wear behaviour of NiTi shape memory alloys,” *Journal of Alloys and Compounds*, vol. 460, no. 1–2, pp. 213–219, Jul. 2008.

[80] A. Nespoli, E. Villa, L. Bergo, A. Rizzacasa, and F. Passaretti, “DSC and three-point bending test for the study of the thermo-mechanical history of NiTi and NiTi-based orthodontic archwires,” *Journal of Thermal Analysis and Calorimetry*, vol. 120, no. 2, pp. 1129–1138, May 2015.

## RESUME

Abuojaila Abdallah Mouammer SOLTAN, 50 years old, born in June 1972, Al-Khoums, Libya, between 1994 and 1995. He graduated from the Intermediate Institute. Between 2004 and 2008, he graduated from the Higher Institute for Comprehensive Professions, with a cumulative average of 51.59. Between 2014 and 2016, he graduated from the Republic of Turkey in the state of Karabuk at Karabuk University with a master's degree in mechanical engineering.